RECEIVED
LAWRENCE
RADIATION LABORATORY

AUG 27 1968

LIBRARY AND
DOCUMENTS SECTION

UCRL-17707
c.2 Eq. 2

University of California

Ernest O. Lawrence Radiation Laboratory

ZERO STRANGENESS RESONANCE PRODUCTION IN 6 GeV/c
PROTON-PROTON COLLISIONS

Robert Ronald Kinsey

(Ph. D. Thesis)

June 1968

TWO-WEEK LOAN COPY

This is a Library Circulating Copy which may be borrowed for two weeks. For a personal retention copy, call Tech. Info. Division, Ext. 5545

UCRL-17707 c.2

E. LRL

DISCLAIMER

This document was prepared as an account of work sponsored by the United States Government. While this document is believed to contain correct information, neither the United States Government nor any agency thereof, nor the Regents of the University of California, nor any of their employees, makes any warranty, express or implied, or assumes any legal responsibility for the accuracy, completeness, or usefulness of any information, apparatus, product, or process disclosed, or represents that its use would not infringe privately owned rights. Reference herein to any specific commercial product, process, or service by its trade name, trademark, manufacturer, or otherwise, does not necessarily constitute or imply its endorsement, recommendation, or favoring by the United States Government or any agency thereof, or the Regents of the University of California. The views and opinions of authors expressed herein do not necessarily state or reflect those of the United States Government or any agency thereof or the Regents of the University of California.

UCRL-17707

UNIVERSITY OF CALIFORNIA

Lawrence Radiation Laboratory
Berkeley, California

AEC Contract No. W-7405-eng-48

ZERO STRANGENESS RESONANCE PRODUCTION IN 6 GeV/c PROTON-PROTON COLLISIONS

Robert Ronald Kinsey
(Ph.D. Thesis)

June 1968

ZERO STRANGENESS RESONANCE PRODUCTION IN 6 GeV/c PROTON-PROTON COLLISIONS

Contents

ABSTRACT v

I. INTRODUCTION 1

II. EXPERIMENTAL PROCEDURE 5

A. The Beam 5

B. Scanning and Roadmaking. 7

C. Measurement and Reconstruction 8

D. Bubble Density Measurements. 11

E. Fitting and Data Reduction 17

III. PRODUCTION CROSS SECTIONS. 19

IV. FINAL STATE $pp\pi^+\pi^-$ 21

A. General Features 21

B. Partial Cross Sections 34

C. One-Pion-Exchange Model. 39

V. FINAL STATE $np\pi^+\pi^+\pi^-$ 42

A. General Features 42

B. Resonant Search. 46

1. The ρ Meson. 46

2. The NN* Final States 49

3. Other Pseudo-Two-Body Final States 55

VI. FINAL STATE $pp\pi^+\pi^-\pi^0$ 59

A. General Features 59

B. Resonant Search. 60

1. The ρ Meson. 60

2. The Pseudo-Two-Body Final States 62

VII. CONCLUSIONS 65

ACKNOWLEDGMENTS 67

APPENDICES 68

A. Shape and Position of N*(1236) Peak 68

B. Form of Baryon Resonances Used in Fitting and Calculations 71

REFERENCES 73

FIGURE CAPTIONS 76

ZERO STRANGENESS RESONANCE PRODUCTION IN 6 GeV/c PROTON-PROTON COLLISIONS

Robert Ronald Kinsey

Lawrence Radiation Laboratory
University of California
Berkeley, California

ABSTRACT

Approximately 33,000 four-pronged proton-proton interactions at 6 GeV/c have been examined for the production of nonstrange meson and baryon resonances. These events were found by scanning approximately 112,000 pictures taken in the LRL 72 -in. hydrogen bubble chamber. The reactions studied in detail and their cross sections are

(1)	$pp \rightarrow pp\pi^+\pi^-$	3.2 ± 0.3 mb
(2)	$pp \rightarrow pn\pi^+\pi^+\pi^-$	2.9 ± 0.4 mb
(3)	$pp \rightarrow pp\pi^+\pi^-\pi^0$	2.4 ± 0.2 mb

Proton-proton interactions have been studied by others in this energy region and this experiment agrees with these studies in the general features of reaction (1). Reaction (1) is dominated by the psuedo-two-body final states NN^* and N^*N^* produced in a peripheral manner. Fits to the various possible final states have been made and are reported. Data from this reaction have also been compared to the peripheral one-pion exchange (OPE) model and the results are given.

In reactions (2) and (3), an interesting feature is the production of an I=3/2 baryon resonance which is observed to decay into a nucleon

and three pions and which produces a peak in the appropriate mass spectrum at 2080 MeV/c^2. In addition, the ρ meson has been detected for the first time in a bubble chamber proton-proton production experiment in addition to the η and ω mesons already reported. Due to the complicated nature of the final states in reactions (2) and (3) fits to the numerous possible final states are not attempted. However an attempt has been made to determine the production cross sections for various new or interesting resonances.

I. INTRODUCTION

In recent years the study of high energy particle interactions has resulted in the discovery of a great number of meson and baryon resonances. They have in general been discovered in two distinct types of experiments. One of these in the case of baryon resonances is the bombardment of a proton target by an appropriate meson beam at a total center of mass energy corresponding to the mass of the resonance. This is called a formation experiment. The second type of experiment is generally called a production experiment and it is this type that is of interest in the work presented here. A production experiment consists of studying the effective mass spectra of multibody final states at high center of mass energies where resonances are produced in association with other particles or resonances. It is of interest to continue the search for as yet undetected resonant states in this type of experiment and to attempt to determine their quantum numbers as they are found. It is also interesting to examine the production mechanisms of those resonances whose existence and quantum numbers are already established.

The importance of multibody final states increases with the increasing energy of the incident particle in production experiments involving the bombardment on nucleons with pions, kaons, nucleons, and anti-nucleons. An important and striking feature of these final states is that they appear to be produced as psuedo-two-body reactions involving one or more resonances.[1] This psuedo-two-body production is also characterized by the tendency of the secondary particles to go in the forward-backward direc-

tions in the total center of mass system. This tendency is suggestive of a peripheral process and one meson exchange models (OME) are often used in an attempt to explain the experimental aspects of these final states, sometimes with striking success.[2]

The percentage of inelastic reactions which can be explained as psuedo-two-body is another point of interest. It has been pointed out[1] that some reaction channels of pion, kaon, nucleon and anti-nucleon interactions with nucleons have a large percentage of resolved psuedo-two-body reactions. For example, in the reaction

$$\pi^+ p \rightarrow p\pi^+\pi^+\pi^- \qquad (1.1)$$

at 8 GeV/c incident pion momentum it is reported[3] that 45% of the reaction is resolved into the psuedo-two-body final states $N^*\rho^o$, N^*f^o, pA_1, and pA_2. In K^+p interactions at 2.7 GeV/c,[4] the reaction channel

$$K^+p \rightarrow K^+p\pi^+\pi^- \qquad (1.2)$$

is found to be 53% $K^{*o}N^{*++}$. In the reaction $pp \rightarrow pp\pi^+\pi^-$, at 5.5 GeV/c, it is reported[5] that 70% of this reaction channel can be explained as N^*N^* and pN^* final states.

That a few reaction channels have a large percentage of psuedo-two-body final states and others only a small percentage may be an experimental bias due to resonances not being recognized. Isobars with isotopic spin I=1/2 are often not resolved and hence they are not counted. The fraction of psuedo-two-body reactions also tends to increase with the discovery of new resonances and will probably continue to do so.

The present experiment involves the study of nonstrange resonance

production in a proton-proton production experiment at 6 GeV/c incident proton momentum. The reaction channels studied involve four or more charged particles in the final state with the emphasis on the following three reactions

$$pp \rightarrow pp\pi^+\pi^- \tag{1.3}$$

$$pp \rightarrow pn\pi^+\pi^+\pi^- \tag{1.4}$$

$$pp \rightarrow pp\pi^+\pi^-\pi^0 \tag{1.5}$$

The psuedo-two-body final states of these three reaction channels have been studied intensively. Reaction (1.3) has been compared to the one-pion-exchange model (OPE) and in addition fits have been made to the partial cross sections of the possible final states. Reactions (1.4) and (1.5) have been examined for resonance production and cross sections for the production of new or interesting resonances have been estimated whenever possible.

Cross sections for the deutron production reactions

$$pp \rightarrow d\pi^+\pi^+\pi^- \tag{1.6}$$

$$pp \rightarrow d\pi^+\pi^+\pi^-\pi^0 \tag{1.7}$$

and channels other than those listed above with more than four charged particles in the final state have also been obtained. However, reactions other than (1.3), (1.4) and (1.5) have not been studied in detail due to small cross sections involved and the difficulty in obtaining a correct identification in the case of the more complicated final states.

Section II discusses the experimental procedure used in this work and Section III gives the production cross sections of the reactions

observed. In Section IV the detailed results of reaction channel (1.3) are reported and compared to a simple one-pion-exchange model. Section V discusses our resonance search in the reaction channel (1.4). Reaction (1.5) is discussed in Section VI. In Section VII we give a summary of the results and conclusions of this work.

II. EXPERIMENTAL PROCEDURE

A. The Beam

Protons produced in a polyethelene target 3/8-in. high, 1/4-in. transverse to and 1/2-in. along the direction of the external proton beam of the Bevatron were transported to the LRL 72-in. liquid hydrogen bubble chamber by the arrangement shown in Fig. 1. Targeting techniques were required to minimize interference with the external beam optics since the external beam was being used for multiple experiments. The optical elements which determined the focal properties of the beam at the uranium collimator were the first quadrupole pair, which gave a vertical magnification of 0.5 and a horizontal magnification of 1.0, and the two bending magnets, which produced a dispersion of one inch per 1% $\Delta P/P$. A momentum definition of ±0.15% was provided by the slit in a 12-in. thick uranium collimator of 1/2-in. vertical and 1/4-in. horizontal dimensions. With an intensity of $\sim 10^{11}$ protons per pulse in the external proton beam, a beam of approximately 30 protons per pulse could be maintained in the channel. Efficient operation was achieved by dynamic intensity control provided by a pulsed parallel plate electromagnetic separator operated with a 4-in. gap and 150 kilovolts between the plates. At an appropriate signal from a preset scalar which read the output of counters placed immediately in front of the bubble chamber, a spark gap across the spectrometer plates was triggered. The plates were thus discharged in 2μsec but the magnetic field remained and caused the beam to be deflected 3/4-in. vertically, off the slit into the uranium collimator. The usual variations

in beam intensity at the bubble chamber due to statistical fluctuations and accelerator instability were greatly reduced by this system of control and the beam was maintained constant to within two tracks per picture.

Contamination from pion production in the target was small since the incident protons of the external proton beam and the secondary protons from the target differed little in momentum while the secondary pions had much smaller momentum. A measurement of the pion contamination for a similar beam using a Cerenkov counter to distinguish pions from protons indicated a contamination by pions of less than 0.1%. This has been neglected as a source of background events in the analysis of the data.

The observed widths of the beam momentum distributions as obtained from both the measurement of non-interacting tracks and from identified examples of fits to elastic scatters were consistent with each other and with that expected from the measurement error of approximately 1%. The momentum of the beam was found to be 6.10 ± .02 GeV/c. An uncertainty of 0.5% was used by the fitting program which is somewhat larger than that deduced from the beam optics to allow for effects such as scattering on slits and other apparatus.

B. Scanning and Roadmaking

Approximately 112,000 pictures of proton-proton interactions in the LRL 72-in. hydrogen bubble chamber were scanned for events with four, six, and eight pronged topologies, that is, events with four, six or eight charged particles in the final state. This scan was done on scan tables equipped for rough measurement of the events that were found. The least count for points measured on these scan tables is 12.5μ. Three points were measured on each track in each of the three views. These points were used later during the automatic measurement of the events to define roads for use by the filtering program in separating digitizations of the bubbles associated with the tracks from background bubble digitizations. In this scan 33,000 four-pronged, 2000 six-pronged, and 50 eight-pronged events were found and had roads made for them.

A rescan was done using every tenth roll of film. Events found and their location were recorded and compared with the first scan in order to compute a scan efficiency for each of the two scans using the fact that in the film scanned twice

$$N_1 = \epsilon_1 N \tag{2.1}$$

$$N_2 = \epsilon_2 N \tag{2.2}$$

$$N_{overlap} = \epsilon_1 \epsilon_2 N \tag{2.3}$$

where N is the number in the film, N_1 and ϵ_1 are the number of events found and the scan efficiency of scan 1, N_2 and ϵ_2 are likewise the number of events found and the scan efficiency of scan 2, and $N_{overlap}$ the number of events common to both scan 1 and scan 2.

Solving equations (2.1), (2.2), and (2.3) for N we get

$$N = \frac{N_1 \times N_2}{N_{overlap}} \tag{2.4}$$

and then for ϵ_1 and ϵ_2

$$\epsilon_1 = \frac{N_1}{N} \tag{2.5}$$

$$\epsilon_2 = \frac{N_2}{N} \tag{2.6}$$

In this way the average scan efficiency of scan 1 was determined to be 68 ± 5% and that of scan 2, 90 ± 2%.

C. Measurement and Reconstruction

The automatic measurement of the events was accomplished by the Berkeley flying spot digitizer system[6] (FSD) which is an integrated system of hardware and programs which utilizes a Hough-Powell device (HPD) controlled on line by an IBM-7094A to digitize the film. Since the number of digitizations transmitted from the HPD to the computer for any given frame greatly exceeds the storage capacity of the computer, the roads defined from the scan table measurements are used by a filtering program to select the digitizations appropriate to the tracks. Further filtering produces a number of averaged points along each track to be used in the spatial reconstruction of the tracks.

Reconstuction of the tracks was accomplished by the three-view reconstruction program FOG[7]. After only one pass through the system an average of 75% of the events were successfully reconstructed, but this

varies from 50% during the first part of the measurement period to about 90% during the final period of measurement.

An investigation has been made of those events which could not be reconstructed by the program FOG. A sample of 592 events which had failed reconstruction had new roads made and were remeasured by the FSD. The original measurement had a 26% failure rate. The failed events after a careful remeasurement had an 18% failure rate. A check was made also to determine if the events which failed had any common characteristics. While all but, at most, forty-four of the failures were determined to be due to random causes such as incorrect scanner recording procedures, failure of the roads to overlay the tracks, poor picture quality, or beam tracks obscured in one or more views by adjacent beam tracks, we know that events with an outgoing track less than about 0.5 cm long in space certainly tend to fail more often than other topologies. This is due to the difficulties encountered in attempting to digitize these tracks on the HPD. This could be an important bias since events with a short dark track correspond to final states in which the momentum transfer squared from the target proton to a final state proton in the backward hemisphere of the total center-of-mass system is small (less than approximately 0.015 $(\mathrm{GeV}/c)^2$). In principle, due to the symmetry of the initial state, we should be able to correct for this bias by examining those events in which the momentum transfer from the beam proton to a final state proton in the forward hemisphere of the total center-of-mass system is small. Unfortunately, in the laboratory system the proton of interest produces a track with a curvature similar to the

beam track and at small angles to the beam direction. If a beam track happens to lie nearby in space to this secondary track, the track may be incorrectly measured due to the partial overlapping of the tracks' images in the photographs. Note that, in the first case involving short tracks, the failures are a function of the topology of the event while in the second case the failure is due in some sense to the quality of the pictures (i.e. the background of beam tracks around the vertex of the event). Thus, while we cannot accurately determine the magnitude of the bias in either case and thus the bias against very low momentum transfer events in general, it seems reasonable to assume that the errors because of bias due to outgoing tracks being overlapped are small in relation to the errors and systematic uncertainties encountered in analyzing a given channel. Due to the similarity of the data from the forward and backward hemispheres, we conclude that the bias due to short tracks is also small. Further, on the basis of the number of events with short stopping tracks recorded by the scanners in a sample of the film, we estimate that less than 1% of the events could have been lost for this reason. In the analysis of the data, we find that the possible bias against low momentum transfers is negligible, but we will refer to it again where appropriate.

D. Bubble Density Measurements

In a bubble chamber experiment the curvature of a charged particle's track due to the magnetic field of the bubble chamber is measured and used to calculate the momentum of the particle. The fitting program, using the conservation of momentum and energy, then calculates the probability that a given combination of final state particles could have produced the observed topology. Ambiguities in the choice of the correct combination of final state particles can occur, especially in those fits with an unobserved neutral particle. Often these ambiguities can be resolved if the velocity of one or two of the tracks can be estimated. This has often been done in other bubble chamber experiments by estimating on the scan table the bubble density of a track and then using the observed fact[8] that the bubble density is proportional to $1/\beta^2$ where $\beta = V/c$. A feature of the FSD measurements that has enabled us to keep scan table checks to a minimum and thus process a large number of events in a reasonable length of time is the measurement of the bubble density which is automatically made when the tracks are digitized on the HPD. Applying the maximum likelihood method, Strand[9] has shown that for a straight track normal to the direction of scan by the flying spot, the most likely value of the bubble density is given by

$$ka = \ln \frac{T}{M} \qquad (2.7)$$

where k is the bubble density of the track as measured on the film, a is the spot size of the flying spot on film, T is the total number of

scan lines intersecting the track, and M is the number of times that no bubble is encountered or recorded when the spot crosses the track (i.e. $M = T - H$ where H is the number of digitizations recorded in T scans across the track). No attempt is made to accurately measure a but, since it does not vary significantly, we can use ka as compared to the value of ka for a minimum ionizing track such as the beam track to get a measure of the relative bubble density of the track.

Formula (2.7) must be generalized, of course, since it assumes a straight track perpendicular to the scan direction. This is done by modifying (2.7) to

$$ka = \overline{\cos\alpha} \ln \frac{T}{M} \tag{2.8}$$

where $\overline{\cos\alpha}$ is the cosine of the angle between the chord of the track and the perpendicular to the scan direction. A correction was also made for the variation in track bubble density due to the temperature gradient of the liquid hydrogen. It was found that tracks which approached the top glass of the chamber became denser and that tracks going into the bottom of the chamber became less dense. By taking a sample of fits with good four constraint chi squares, the measured bubble density and the predicted relative bubble density were used to calculate what the bubble density of the reference track would be at the average location of the track in Z, the vertical height. Figure 2 shows the results of such a study, where ka of the reference track is plotted versus the average Z of the track in the bubble chamber. We note that tracks which have the higher average values of Z also require a higher reference ka to get the correct value of the relative

bubble density or, as interpreted here, these tracks have a higher bubble density due to the higher temperature of the liquid hydrogen in this region. A polynomical fit in Z was made to these points to determine a weighting function which has the effect of decreasing the measured ka of a track in the top of the chamber and increasing it for a track in the bottom. Thus, all tracks have their measured ka adjusted to an arbitrary point in Z by use of this weighting function which tends to cancel the temperature effect.

Using the weighted value of ka, we find that the bubble densities of the outgoing tracks relative to the beam tracks for a sample of events with four constraint fits agrees quite well with the relative bubble densities predicted by a $1/\beta^2$ dependence. In Figs. 3(a) and (b) the value of $(I_{meas}-I_{calc})/I_{calc}$ has been plotted where

$$I_{meas} = \frac{\langle ka \rangle \text{ outgoing track}}{\langle ka \rangle \text{ beam track}} \tag{2.9}$$

and

$$I_{calc} = \frac{\beta^2 \text{ beam track}}{\beta^2 \text{ outgoing track}} \quad . \tag{2.10}$$

We define $\langle ka \rangle$ as the average value of the bubble density times the spot size. The average is made over the three views and is weighted by the assigned errors.

We include in Figs. 3(a) and (b) the values of $(I_{meas}-I_{calc})/I_{calc}$ for those tracks which had their relative bubble density measured and have a calculated relative bubble density less than 3.0. The requirement placed on the calculated bubble density is necessary since at a relative bubble density of about 3.0 the track becomes a solid line on

the film without any apparent gaps and the bubble density cannot be measured accurately. Figure 3(a) is for tracks measured in the normal mode. Figure 3(b) is similar except that the tracks were measured in the orthogonal mode. The normal and orthogonal modes are defined by the direction the flying spot is moved in relation to the film during the digitizing of a given track. In the normal mode the flying spot is moving across the width of the film. In the orthogonal mode the flying spot is moved perpendicular to the normal scan direction, that is, along the length of the film. The choice of which mode will be used for the measurement is made by calculating the projected length of the track parallel and perpendicular to the scan direction in the film plane. That measurement mode in which the perpendicular length is greater than the parallel length is the one used.

To bring I_{meas} into agreement with I_{calc} for those tracks measured in the orthogonal mode it was found necessary to assume that 5% of the digitizations of these tracks were lost or not recorded. This is apparently due to the fact that the optics of the FSD are optimized for the normal mode of operation. The orthogonal mode represents somewhat of a compromise. The effect of this is that the intensity of the spot of light used to scan the film in the orthogonal mode is less than that used in the normal mode.

In terms of the measured parameters the average of ka is written as

$$\langle ka \rangle = \frac{\sum_{i=1}^{3} \frac{(ka)_i}{\sigma_i^2}}{\sum_{i=1}^{3} \frac{1}{\sigma_i^2}} \qquad (2.11)$$

where σ_i is the error of the measurement of $(ka)_i$ in view i.

From equation (2.8) the error in (ka) can be found to be

$$\sigma_i = \overline{\cos\alpha}\sqrt{\frac{H}{MT}} \tag{2.12}$$

and the averaged error

$$\sigma = \sqrt{1/\sum_{i=1}^{3}(1/\sigma_i^2)} \tag{2.13}$$

Equation (2.12) was found to give an error which was apparently too small as was expected since systematic errors are not included in the calculation. Also, Eq. (2.13) is based on the assumption that the measurements are uncorrelated and, thus, gives an average error which is smaller than the real error. To take possible systematic errors into account and to offset the correlation between the measurements we have chosen to rewrite Eq. (2.12) as

$$\sigma_i = \overline{\cos\alpha}\sqrt{\frac{H}{MT} + (eH)^2} \tag{2.14}$$

where e is a parameter which was adjusted so that the pull quantity $(I_{meas}-I_{calc})/\sigma$ for the tracks measured had a half width at half maximum of 1.0. The value of e used for measurements made in the normal mode was 4.0×10^{-4} and for measurements made in the orthogonal mode it was 4.0×10^{-3}. The pull quantity for the tracks studied are shown in Figs. 4(a) and (b) for the normal and orthogonal modes respectively.

To facilitate the selection processing of the events a χ^2_{ION} was calculated. The unfitted χ^2_{ION} was calculated as

$$\chi^2_{ION} = \sum_{i=1}^{n}\left(\frac{I_{meas}-I_{calc}}{\sigma}\right)_i^2 \tag{2.15}$$

The second reason for excluding a track from the bubble density χ^2 of a fit is due to the poor discrimination of the relative bubble densities above about 3.0. As the relative bubble density approaches 3.0, the tracks begin to appear as solid dark lines since the bubbles are close together and can appear to merge. As the track image approaches that of a solid line, the number of misses, M, approaches zero and ka as given by Eq. (2.8) tends to become undefined although the value calculated from a $1/\beta^2$ dependence remains defined for all nonzero momentum tracks. Also, as the number of misses due to gaps in the track becomes small, the number of accidental misses becomes very important. Thus, a track was not used in the calculation of the χ^2_{ION} if I_{calc} given by Eq. (2.10) was greater than 2.5. The fit was rejected however, if the I_{calc} for a track was greater than 2.5 but the I_{meas} was less than 1.5. A minimum I_{meas} of 1.5 was used to take into account the large errors associated with the I_{meas} of dark tracks and the possibility of having a low value of I_{meas} because the ka of the beam track was measured too high due to overlapping by another beam track.

E. Fitting and Data Reduction

Kinematic fits by the program CLOUDY[10] were attempted for each event using every known combination of strongly interacting particles which was consistent with the observed topology, conserved energy, strangeness, and baryon number and had at most one unobserved neutral particle. A hypothesis was accepted if both the χ^2_{KINE} and χ^2_{ION} corresponded to probability levels greater than 1%. Ambiguities between four constraint and one constraint kinematic fits were always resolved in favor of the four

where the sum is taken over the n outgoing tracks to be used in the fit. A difficulty encountered when attempting to use this unfitted χ^2_{ION} can be seen by referring to Eq. (2.9). The <ka> of the beam track is used as a reference but some beam tracks are overlapped in one or more views by another beam track and can have a measured <ka> up to twice as large as it should be due to the extra digitizations from the other beam track. In order to obtain a reasonable χ^2 for all events we have chosen to use a fitted χ^2_{ION} defined as

$$\chi^2_{ION,Fitted} = \sum_{i=1}^{n} \left(\frac{aI_{meas} - I_{calc}}{a\sigma} \right)_i^2 \qquad (2.16)$$

with n outgoing tracks as before. The value of a is allowed to vary for each proposed fit until the minimum value of χ^2_{ION} has been reached.

In Figs. 5(a) and (b) we show the unfitted and fitted χ^2, respectively, calculated for the bubble density measurements of those events with a four constraint kinematic χ^2 of greater than 5% probability and for which all four of the outgoing tracks could be used in the bubble density χ^2. Both the unfitted and fitted χ^2 are in good agreement with the peak values and shape expected for four and three constraint χ^2 distributions respectively.

A track could be excluded from the χ^2 and the constraint class of the bubble density fit reduced for one of two reasons. In the first case the filtering program rejected the measurement because of possible confusion with a crossing track or because the total number of hits exceeded the computed number of scan lines. The former could be light or dark tracks while the latter were always black. In this case a scan table check of the event had to be made if there was any possible confusion.

constraint fit. Other ambiguities were first checked to see if both the kinematic and bubble density χ^2's noticeably favored one fit more than the other. After this check only 5% of the events were classified as ambiguous. These ambiguous events were checked on the scan table and an independent estimate of the bubble densities of each track was made. Using the bubble densities which had been checked on the scan table, a final selection was made by a physicist of these ambiguous events with the result that only 1% of the events in the final sample remain ambiguous. These hard core ambiguities are assigned to both of their most likely fits with a weight of 0.5.

III. PRODUCTION CROSS SECTIONS

To determine the absolute cross sections of the reaction channels of interest it is necessary to determine:

1) the number of events of a given type in a specified fiducial volume over a known number of pictures;
2) the total length of beam track present in the same volume and the same pictures;
3) the density of the liquid hydrogen in the bubble chamber.

Table I lists the results of the selection and assignment of events to various reaction channels over a sample of approximately 68000 frames of the total 112000 frames scanned. The failure rate in reconstruction of the events, as previously mentioned, varied during the measurement period, being lowest during the last half of the measurement period. Since these events have only been measured once it was thought desirable to use that sample of data with the smallest proportion of measurement failures to determine the production cross sections.

The total length of beam track scanned in these frames was determined by counting the number of beam tracks at the end of the fiducial volume which had passed through the fiducial volume without interacting and then calculating with the known total cross section at this energy what the total beam track length must be. The count was done for every fiftieth frame of every tenth roll. The average number of beam tracks at the exit end was found to be 8.2 ± 0.3 tracks/frame. The fiducial volume used was 108.1 cm long in the

beam direction. Using a total cross section for pp interactions at 6 GeV/c of 40.7 $\pm$ 0.6 mb[11] we find the average number of track lengths per frame to be 8.9 $\pm$ 0.4. The total track length is then

$$L = N_F \, N_T \, l = 65.1 \times 10^6 \text{cm} \pm 5\% \qquad (3.1)$$

where N_F = number of frames scanned (67640), N_T = average number of track lengths per frame, and l = length of the fiducial volume.

The density of the hydrogen was derived from measurements of the chamber vapor pressure during the exposure. The density has been determined to be .0600 $\pm$ .0006 g/cm^3.

The absolute cross section for all the four pronged events is then determined by:

$$\sigma = \frac{N}{L} \frac{A}{N_o \rho} = 10.8 \pm 0.9 \text{ mb} \qquad (3.2)$$

where N is the number of four pronged events corrected by the scan efficiency, A is the atomic weight of hydrogen (1.01), N_o is Avogadro's Number (6.023×10^{23} mole^{-1}), ρ is the density of the hydrogen, and L is the track length scanned. Table II lists the cross sections of interest with their calculated errors. The errors take into account the errors associated with the determination of the hydrogen density, the scan efficiency, the total beam track length, and the statistical error in the number of events in each channel. Also listed in Table II for comparison purposes are the production cross sections of other pp experiments.

IV. FINAL STATE $pp\pi^+\pi^-$

A. General Features

The most striking feature of this reaction channel is the production of zero strangeness baryon resonances. The zero strangeness baryon resonances or N*'s that we observe in this final state have all been previously observed in pion-nucleon scattering and their quantum numbers have been established by a number of experiments using a variety of techniques generally based on the direct formation of the resonance being studied by bombardment of a nucleon target with a pion beam of the appropriate energy. In this experiment we do not attempt to accurately determine the masses, widths, or quantum numbers of these resonances, but rather use this information as established in other experiments to investigate the production mechanism and cross sections of these resonances.

In Figs. 6 and 7, the $p\pi^+$ and $p\pi^-$ mass spectra are shown for the final state $pp\pi^+\pi^-$. Two combinations each with a weight of 0.5 are shown for each event due to the indistinguishability of the two final state protons.

In the $p\pi^+$ mass plot of Fig. 6 we note a large enhancement in the low mass region which peaks at about 1220 MeV/c^2 and has a width at half maximum of approximately 100 MeV/c^2. This peak we attribute to production of the $N^{*++}(1236)$. Taking into account the fact that half of the combinations plotted are background this peak is consistent with assuming that approximately 80% of the events involve production of this resonance. A more accurate statement requires a knowledge of the shape of background distribution of the $p\pi^+$ combinations in which the proton and the π^+ are produced at different vertices. This in turn requires a knowledge of the

final states taking part in the reaction channel and their relative abundance since the reflections are different in each of the final states. The curve in this figure is the result of a fit which attempts to take into account all of the final states observed. We will discuss the results of this fit in the next section.

In Fig. 7 two resonance peaks are observed at 1500 and 1675 MeV/c^2 which we attribute to the zero strangeness baryon resonances $N^{*o}(1525)$ and $N^{*o}(1680)$. Assuming a smooth background continued from about 1325 MeV/c^2 into the high mass region above 1800 MeV/c^2 we find that the $N^{*o}(1525)$ and the $N^{*o}(1680)$ are produced in approximately 5.3% and 4.0% respectively of the events. The analysis of the $N^{*o}(1680)$ is obscured by the fact that three resonances with different spins and parities are known to occur at approximately this mass. One of these is an I=3/2 resonance at 1670 MeV/c^2 which we expect from isotopic spin considerations to be only weakly produced in this charge state. The two I=1/2 resonances occur at 1670 and 1688 MeV/c^2 with spin-parity, J^P, of $5/2^-$ and $5/2^+$ respectively. A comparison of the $N^{*++}(1236)$ peak with the theoretical distribution (see Appendix A) indicates that our mass resolution is approximately 20 MeV/c^2 and while this is good for a bubble chamber experiment it is not sufficient to separate these two resonances. In the subsequent analysis of this peak we will refer to the $N^*(1680)$ since we cannot distinguish between the two mass values 1670 and 1688 MeV/c^2.

Also in Fig. 7, a peaking in the mass plot can be seen in the 1220 MeV/c^2 region which we will later find is consistent with production of the $N^{*o}(1236)$, but since the background can also peak in this region it is very difficult to estimate the percentage of its production.

The curve again shows the results of the fit to be discussed in the next section.

In Fig. 8 the $p\pi^+\pi^-$ mass spectrum has been plotted. Again two combinations, each given a weight of 0.5, have been plotted for each event due to the indistinguishability of the final state protons. Two peaks can be observed in this plot. One is at 1525 MeV/c^2 and the other at about 1675 MeV/c^2 which we attribute to the $N^{*+}(1525)$ and $N^{*+}(1680)$. As with the $N^*(1236)$ in the low mass regions of Figs. 6 and 7, the relative amounts of the resonances observed here depend quite strongly on the shape of the background distribution. The solid curve shows the results of the fit to be discussed in the next section.

In Fig. 9 we show the $\pi^+\pi^-$ effective mass spectrum. While there is no evidence in this mass plot for the production of any meson resonances, we do not exclude the possible production of a ppM^o final state where M^o is a neutral meson resonance decaying into $\pi^+\pi^-$ if the production cross section is smaller than we can detect with this experiment. For example, the final state $pp\rho^o$ would have to have a cross section greater than at least 20 μb to be detected in this experiment. The curve shown on this mass plot is a result of the fit described in the next section which attributes 98% of the pion production in this final state to the decay of the observed baryon resonances. As we can see, the curve agrees quite well with the experimental distribution.

Figure 10 shows the production angular distribution in the total center-of-mass system of the final state protons in the variable $\cos\theta(p)$, where $\theta(p)$ is the angle between the final state proton and the beam direction. The final state protons are symmetrically produced and

strongly peaked forward-backward with respect to the beam direction, suggesting that peripheral processes are a dominate feature of the production mechanism for this final state.

Referring to Figs. 6,7, and 8 we can see that two types of peripherally produced psuedo-two-body final states may be important in understanding the production mechanism. They are $pp \rightarrow N^{*++}N^{*0}$ and $pp \rightarrow pN^{*+}$. Figures 11(a) and (b) show the simplest one-particle-exchange diagrams for the production of these two final states. To produce to final state $N^{*++}N^{*0}$ as shown in Fig. 11(a) obviously requires I=1 exchange such as one-pion-exchange. However, the production of the pN^{*+} final state as shown in Fig. 11(b) can involve either I=1 or I=0 exchange. Of course, many other processes and diagrams are possible but we will not consider them here.

If peripheral production and the Feynmann diagrams shown in Figs. 11(a) and (b) correctly describe the major features of the production mechanism for this final state then it is useful to attempt to select for detailed study, based on the requirements of the model, events most

likely to have been produced by a given process and, in addition, suppress events due to competing processes. Also, this selection of events should tend to remove the confusion inherent in the indistinguishability of the final state protons. For example, to study the contribution to the total matrix element of the diagram shown in Fig. 11(a), it would be convenient to be able to make the "right" choice when assigning the final state protons to the two vertices such that p_1 is the proton produced in association with the π^+ at one vertex and p_2 is the proton produced with the π^- at the other vertex. In Fig. 6, it is difficult to study resonance production at the $p_1\pi^+$ vertex of Fig. 11(a) since both the $p_1\pi^+$ and the $p_2\pi^+$ effective masses were included. The effect of including $p_2\pi^+$, the "wrong" choice, is to add a background to the $p\pi^+$ distribution which is impossible to calculate exactly without a detailed knowledge of the resonance production at the $p_2\pi^-$ vertex. In addition, we need to suppress the contribution of competing diagrams (e.g. as shown in Fig. 11(b)) which can also add to the background and obscure the resonance production we wish to investigate. Similar remarks are also appropriate to the study of the $p_2\pi^-$ vertex of Fig. 11(a) and the $p_2\pi^+\pi^-$ vertex of Fig. 11(b). Note that by using Monte Carlo techniques to generate events according to a theoretical model, we can take into account any cuts we may find necessary to improve the representation of our data when we compare theory and experiment. Two methods appear to be useful in selecting the events and resolving ambiguities.

The first method is based on the observed peripheralism of the production mechanism. For example, we can consider the final state

shown in Fig. 11(b) with a proton (p_1) produced at one vertex and a baryon resonance at the other vertex which decays into $p_2\pi^+\pi^-$. The question then is which of the two final state protons is to be assigned to the resonance at vertex b and which is to be the isolated proton at vertex a. In calculating the momentum transfer to a final state proton the question arises as to which of the initial protons to use, the beam or the target proton. In the spirit of the peripheral model we always choose that initial proton which gives the smallest absolute value of the momentum transfer. We can estimate as an upper limit that not more than 10% of the events will have the incident proton incorrectly chosen with this technique, if single pion exchange is indeed the proper mechanism. If the distribution of cos $\theta(p)$ shown in Fig. 10 is folded at cos $\theta(p) \doteq 0.0$ which is equivalent to always choosing the minimum momentum transfer, the question of the percentage of incorrect choices becomes one of estimating the number of events in which a proton is scattered through more than 90°. At $\theta(p) = 0^\circ$ we have a large peak which falls rapidly to a minimum value at $\theta(p) = 90^\circ$. In the peripheral model the worst that can happen is for the distribution to flatten out and maintain this minimum value between 90° and 180°. This means that approximately 1200 protons will have the wrong incident proton chosen. Now, to determine which of the final state protons is to be assigned to the single particle vertex, again the proton with the minimum absolute momentum transfer is chosen. This double selection on minimum momentum transfer is the double del squared method. This method of assigning the two final state protons must be used with care since it has the important restriction that it tends to enhance the low mass region of the mass distribution of the particles at

vertex b (i.e. $p_2\pi^+\pi^-$ mass distribution in the specific case where p_1 and p_2 are the two protons in the $p_1p_2\pi^+\pi^-$ final state and p_1 is chosen by the double del squared method to be at the vertex a of Fig. 11(b)). Further, a serious objection to this method can be raised if we attempt to choose the $p\pi^+$ combination appropriate to the $N^{*++}(1236)$ resonance on this basis. If this resonance were produced predominantly at one vertex as shown in Fig. 11(a) and the other particles at the other vertex, then this method might still be appropriate, but the data indicates that a significant proportion of the $N^*(1236)$ present is produced as a decay product of higher resonances as shown in Fig. 11(c). The double del squared procedure has no meaning when applied to the decay product of a resonance so let us consider the second method of selecting between two indistinguishable particles.

We may choose to consider only those events with the $p\pi^+$ effective mass in a band $1.220 \pm B$ GeV/c^2 in order to select protons from an $N^{*++}(1236)$ decay. With B chosen narrow enough very few events will have more than one combination in the band. If both possible $p\pi^+$ combinations do have effective mass values in the band, we can process the event in two ways. First, we may use both combinations, count the event twice, and accept the fact that at least half of these events will be background. Second, we can neglect these events entirely and not make any wrong choices or any right ones either for these ambiguous events. Both of these methods have advantages and disadvantages. For example, if there are few events and the background from the wrong combinations is smoothly varying, the first method might be appropriate. If the background events can produce sharp peaks as sometimes occurs in angular distributions and if there are

sufficient data, the second method might be appropriate.

Now that we have discussed the types of selections that can be made on the data, let us proceed with the analysis of the $pp\pi^+\pi^-$ final state. First, we will examine events appropriate to the peripheral pseudo-two-body final state pN^{*+} to see which of the possible N^*'s are present. Second, we will examine the $N^{*++}N^{*0}$ pseudo-two-body final states. In the next section we will attempt to use the observed resonances and final states to make an overall fit.

We use the double del squared method to pick p_1, the nonresonant proton as shown in Fig. 11(b). The $p_1\pi^+$ mass spectrum still shows considerable $N^{*++}(1236)$ production even after this selection so we also select only those events with the $p_1\pi^+$ effective mass less than 1120 MeV/c^2 or greater than 1320 MeV/c^2 . Figure 12 shows the resulting $p_2\pi^+\pi^-$ mass spectrum. Out of 5681 events, 3527 survive this mass cut. We estimate that approximately 720 of the events eliminated are background under the N^* peak. The mass spectrum of Fig. 12 has two peaks corresponding to the mass and widths of the established zero strangeness baryon resonances $N^*(1525)$ and $N^*(1680)$ which appear in our mass plot at 1525 and 1675 MeV/c^2 respectively. In addition, an enhancement at 1425 MeV/c^2 in this mass spectrum can be interpreted as an indication of $N^*(1400)$ production. It is necessary to note that the low mass region of this plot where resonance production is observed can be affected by two different biases. As is well known, the double del squared method of selection tends to bias the selected data in favor of the low effective masses. Conversely, a bias in the measured events against events with low momentum transfer protons in the final state will result in a bias against events with low effective

masses. The first bias can be taken into account when we calculate the background and the second is certainly smaller than the uncertainty in the shape and normalization of the assumed background.

Using the curve shown as an estimate of the background we find that in this sample of events 7% are attributable to N*(1400), 10% to N*(1525), and 14% to N*(1680). We must note that the percentage of events attributed to each of these resonances depends quite critically on the shape and normalization of the assumed background. The curve shown is a "peripheral phase space" which was calculated using Monte Carlo techniques to generate events distributed according to:

$$d\sigma^2 = \text{const.x} \frac{e^{-A\Delta^2} \Delta^2}{(\Delta^2 + m_\pi^2)^2} R(m) \qquad (4.1)$$

where

Δ^2 is the four-momentum transfer squared between p_1 and p_A as shown in Fig. 11(b);

R(m) is the three-body phase space factor for $p_2\pi^+\pi^-$; and

m is the effective mass of $p_2\pi^+\pi^-$.

The same selections made on the experimental data were made on the Monte Carlo events (i.e., $\Delta^2(p_1) \leq \Delta^2(p_2)$, and $M(p_1\pi^+) \leq 1120$ MeV/c^2 or $M(p_1\pi^+) \geq 1320$ MeV/c^2). The observed slope of the momentum transfer distribution was reasonably approximated by A=4.0. The curve was normalized to the observed mass distribution above 2000 MeV/c^2.

The effects of assumptions other than those used above on the shape of the background can be quite significant. Using the momentum transfer dependence given by Eq. (4.1) with A=4.0 rather than the simple non-peri-

pheral phase space has caused the peak of the background distribution to be shifted from about 2400 MeV/c^2 to 2050 MeV/c^2. If we assume that the background is due to $p_1 N^*_{1236}(p_2\pi^+)\pi^-$ and calculate a "peripheral phase space" as before, taking into account the shape of the N*(1236), we can generate a background which peaks in the 1600 to 1700 MeV/c^2 region. This type of background would tend to reduce the number of events assigned to production of the N*'s 1400, 1525, and 1680. Other backgrounds for this mass plot due to final state configurations other than those above further complicate the analysis. We must note, however, that any background we choose which contains resonance production must also reproduce the observed mass spectra in those plots in which these resonances are observed. This is the purpose of the overall fit attempted in the next section.

Another aspect of the pseudo-two-body final state pN^{*+} is the decay mechanism of the N*. It is possible that the resonance simply breaks up into the three particles observed in the final state as represented in the following equation

$$N^{*+} \rightarrow p_2\pi^+\pi^- \tag{4.2}$$

or the resonance can cascade by decaying into another resonance, such as the N*(1236), plus a pion and then that resonance can decay as represented by the following

$$N^{*+} \rightarrow N^{*++}_{o}(1236)\pi^{\mp}, \quad N^{*++}_{o}(1236) \rightarrow p_2\pi^{\pm} \tag{4.3}$$

It would seem appropriate to examine the $p_2\pi^+$ mass spectrum to determine what the ratio of N*(1236) production is compared to the background.

Unfortunately, because of the kinematics, the N*'s under consideration here all produce peaks in the 1200-1240 MeV/c^2 range even if the decay does not involve the production of an intermediate N*(1236). For example, if the $p_2\pi^+\pi^-$ effective mass were 1500 then the maximum $p_2\pi^+$ effective mass can only be 1360 MeV/c^2; the minimum must be 1078, and the peak value in between. Furthermore, if we attempt to examine a given mass interval in the $p_2\pi^+\pi^-$ mass spectrum in order to test the shape of the $p_2\pi^+$ mass spectrum with respect to the predicted N*(1236) distribution, the statistics become very poor in a given bin due to the limited number of events and the unknown background becomes very important (e.g. is the background resonant or non-resonant). This source of N*(1236) production or non-resonant background under the N*(1236) peak cannot be neglected, however, when we make our fits or when we select for N*(1236) production at a vertex such as vertex a in Fig. 11(a).

With the above remark in mind, let us look once more at the $p\pi^-$ mass spectrum. Since, as we have seen in Fig. 6, the production of $N^{*++}(1236)$ dominates the reaction channel, it should not be surprising if the N^{*o}'s seen in the $p\pi^-$ mass spectrum of Fig. 7 were produced in the pseudo-two-body final state $N^{*++}_{(1236)}N^{*o}$ where the N^{*o} can be one of the following three resonances: $N^{*o}(1236)$, $N^{*o}(1525)$, and $N^{*o}(1680)$. In Fig. 13 we have plotted the $p_2\pi^-$ mass spectrum when the $p_1\pi^+$ effective mass is in the range 1160 to 1280 MeV/c^2. A total of 3223 events out of 5681 survive this mass cut and 459 have both possible $p\pi^+$ effective masses in this range and have thus been plotted twice. The shaded region shows the two combinations of the $p\pi^-$ effective mass when both possible $p\pi^+$ effective masses are in the N*(1236) range. As we can see,

these events are smoothly distributed over the allowed mass region and do not contribute to the resonant peaks in any significant amounts. Using as a background a curve which is a smooth continuation of the observed distribution above 1800 MeV/c^2 into the 1400 MeV/c^2 region and then is allowed to fall off to zero at threshold, we get a rough estimate for $N^{*o}(1525)$ and $N^{*o}(1680)$ production which corresponds to 5% and 4% respectively of the events surviving the $N^{*++}(1236)$ mass cut. The exact amount of $N^{*o}(1236)$ production, as mentioned before, is critically influenced by the assumed background distribution, but it is on the order of 10% of the selected events.

In order to be certain that the $N^{*++}(1236)$ we have selected is produced at a vertex as shown in Fig. 11(a) and is not a decay product of a higher mass resonance or a reflection in the low mass $p\pi^+$ mass spectrum due to these higher massed resonances, we require the $p_1\pi^+\pi^-$ effective mass to be greater than 1800 MeV/c^2 where $p_1\pi^+$ is the effective mass combination chosen to lie in the $N^*(1236)$ band from 1160 to 1280 MeV/c^2. The resulting $p_2\pi^-$ mass spectrum is shown in Fig. 14. As we can see, the background has been reduced but the magnitude of the resonant peaks above the background has not been significantly changed.

At this point in the discussion of the $pp\pi^+\pi^-$ final state we have shown several known baryon resonances to be present in our data. We shall use these observed resonances when we make an overall fit in the next section in an attempt to find the partial cross sections for the production of these resonances in various psuedo-two-body final states. For the moment let us turn our attention briefly to the question of the production mechanism of the observed final states. In particular, since

the production of the $N^{*++}(1236)$ resonance is so dominant, let us see if a one-pion-exchange mechanism could be responsible for the production of this resonance in the psuedo-two-body final states $N^{*++}(1236)N^{*o}$.

As shown in Fig. 11(a), if the exchanged particle is a virtual pion, it has been shown[19] that the distribution of the angle, θ^*, of the final state proton resulting from the decay of the $N^*(1236)$ with respect to the incoming initial state proton in the $N^*(1236)$ center of mass is given by

$$I(\theta^*) = \text{const.}\ (1 + 3\cos^2\theta^*) \quad . \qquad (4.4)$$

In Fig. 15 we show the cos θ^* for those events with the $p_1\pi^+$ effective mass in the range 1160 to 1280 MeV/c^2 in order to select for $N^{*++}(1236)$ decaying into $p_1\pi^+$ and which in addition have a $p_1\pi^+\pi^-$ effective mass above 1800 MeV/c^2 in an attempt to exclude any $N^{*++}(1236)$ which is produced as the decay product of a higher mass resonance. The distribution is not symmetric forward-backward and does not seem to agree well with the distribution predicted by Eq. (4.4). We must note, however, that of the 1777 data points shown, 499 correspond to events with both $p\pi^+$ combinations in the $N^*(1236)$ band. In the shaded area of Fig. 15, the events with ambiguous $N^*(1236)$ selections have been eliminated leaving 1278 selected events. The distribution for these events is quite symmetric. The curve shown was calculated assuming that 50% of the events are distributed according to Eq. (4.4) and the other 50% are distributed isotropically. The ageement between the curve and the distribution of events in the shaded region is reasonable. We will investigate the one-pion-exchange production mechanism more thoroughly in the section following the discussion of the partial cross sections.

B. Partial Cross Sections

In the previous section we have shown that zero-strangeness baryon resonances are abundantly produced in the reaction channel

$$pp \rightarrow pp\pi^+\pi^- \quad .$$

In addition, these resonances appear to be produced peripherally in a variety of psuedo-two-body final states. The cuts that were made to enhance the resonances in the mass plots and uncertainties in background caused by the reflections of the various final states present make it very difficult to estimate the cross sections for the production of a given resonance or psuedo-two-body final state. In order to abstract this information on the partial cross sections for production of psuedo-two-body final states, a maximum likelihood fit was made using all of the available data without any cuts. This information is important if we wish to compare the results for this reaction channel with other experiments or reaction channels in order to examine the production of an individual psuedo-two-body final state such as $N^{*++}(1236)N^{*o}(1236)$ as a function of the total center-of-mass energy or if we wish to find the ratio of $\sigma(N^*(1688) \rightarrow p\pi^+\pi^-)/\sigma(N^*(1688) \rightarrow n\pi^+)$ produced in the final state $pN^{*++}(1688)$ for example.

The program MURTLEBERT[20] was used to make the maximum likelihood fit since it was found to be the best program available although it is not entirely satisfactory. The program calculates a frequency function for each event which has the following form:

$$\mathcal{L}(\vec{\alpha},\vec{\beta},\vec{x}) = \sum_{i=1}^{N} \alpha_i P_i(\vec{\beta}_i,\vec{x}) \qquad (4.5)$$

where

$\mathcal{L}$ = frequency of the event

α_i = fraction of the ith final state

$\vec{\beta}_i$ = parameters of the ith final state (i.e. masses, and widths of the resonance, etc.)

$\vec{x}$ = measureables of the event (i.e. effective masses)

N = the number of final states included in the model

P_i = normalized probability that an event corresponds to the ith final state (i.e. $\int P_i(\vec{\beta}_i,\vec{x})d\vec{x} = 1$) .

The normalized probability is calculated using Briet-Wigner formulas for the resonance production in a given final state times the appropriate phase space factors. A likelihood function is formed by taking the product of the frequency functions and then the values of the parameters α_i are found which maximize the likelihood function. The values of the parameters $\vec{\beta}_i$ for the resonance production in the ith final state such as the masses, widths, spin, parity, and inelasticity are treated as known and we have used the values available from phase shift analyses of π-N scattering. Further remarks concerning the momentum and energy dependence of the partial and total widths used in the Breit-Wigner formula for fitting the shapes and positions of the resonance peaks are discussed in Appendix B. This procedure assumes that the matrix elements for the production of different final states do not interfere but this does not appear to cause any difficulties. A much more serious problem is the fact that the program, unfortunately, does not take into account the effects of the peripheralism observed in this final state. This is especially important in the low mass region of the $p\pi^+\pi^-$

(i.e. below about 1600 MeV/c^2) where peripheralism and N*(1236) production can conspire to produce significant enhancements. The total amount of pN*(1400) and pN*(1525) assigned by the fit is in effect an upper limit due to the unknown nature of the peripheral background. The mass and width of the N*(1400) are not well established and with a width of 200 MeV/c^2 as assumed in the fitting program this procedure chooses to assign a larger fraction to this resonance than we believe likely from our examination of Fig. 12.

We have attempted to keep the number of variable parameters small by using only those final states which were observed in the preceding section and excluding those final states which are possible but not directly observed in the mass plots. For our model we have assumed nine final states, eight resonant final states, (see table III), and the non-resonant final state $pp\pi^+\pi^-$. This model requires the use of sixteen sensitive parameters in the fitting procedure since the indistinquishability of the final state protons requires us to calculate two normalized probabilities for each resonant final state which differ only in the interchange of the final state protons. The fraction of the non-resonant final state $pp\pi^+\pi^-$ is fixed by the requirement that the sum of all the α_i's must equal one. In general, we found that the inclusion of other possible but unobserved final states did not improve the agreement in the mass plots between the experimental data and the predictions of our model. However, the final state pN*(1920) was included in the fits to account for an excess of events in the 1800 to 2100 MeV/c^2 region of the $p\pi^+\pi^-$ mass spectrum. It is possible that some or even all of the enhancement in this region can be explained by a peripheral background

such as that in Fig. 12, so again this cross section should be considered as an upper limit.

Only the cascade decays of the $N^*(1525)$ and $N^*(1688)$, as shown in Fig. 11(c), into an intermediate $N^*(1236)\ \pi$ state prior to the production of the observed particle combination $p\pi^+\pi^-$ were finally used in the fits since it was found that the program was insensitive to the shape of the $p\pi$ mass spectrum for $p\pi^+\pi^-$ combinations in this mass region and always chose the cascade decay as most probable. We expect this from a consideration of the kinematics when we limit ourselves to $p\pi^+\pi^-$ effective masses around 1500 MeV/c^2, as previously remarked. The fit is sensitive to the branching ratio of $\Gamma(N^*(1400) \rightarrow p\pi^+\pi^-)/\Gamma(N^*(1400) \rightarrow N^{*\pm+}(1236)\pi^{\mp})$ since the kinematic peak in the $p\pi$ mass spectrum no longer occurs at the $N^*(1236)$ peak but at a somewhat lower value. However, since the shape and position of the kinematic peak are so strongly dependent on the mass and width used in the fitting program for the $N^*(1400)$ we must note that the branching ratio of $.45 \pm .10$ found in this fit can be much different if the real mass and width of the $N^*(1400)$ are significantly different from the values 1400 MeV/c^2 and 200 MeV/c^2 assumed in our fit. The ratio of $N^{*++}(1236)\pi^-/N^{*o}(1236)\pi^+$ used in the fitting procedure for the cascade type decays was fixed at 9:1 in accordance with the isotopic spin predictions.

The result of the fit is tabulated in Table III and the best fitted curves are shown in Figs. 6, 7, 8, and 9. Since the program fits for resonance production in the $p\pi^+$, $p\pi^-$ and $p\pi^+\pi^-$ effective masses simultaneously and then calculates the mass distributions to be expected using the fitted amounts of each final state, the predicted mass distribution

in a given effective mass such as the $p\pi^-$ includes not only the resonance production and phase space for that effective mass combination but also the reflections in that effective mass distribution of resonance production in the other effective mass combinations. This procedure is certainly superior to considering only resonance production plus phase space in isolated mass plots. As we can see in Figs. 6, 7, 8, and 9, the agreement between the data and the curves calculated when the fitted parameters are used in our model are quite good in spite of the fact that the observed peripheralism of this final state has not been taken into account.

At this point let us note that the errors quoted in Table III are evaluated from the fit only. The error on the total cross section and systematic errors due to biases against low momentum transfer events have not been included to avoid any confusion. The total cross section error adds to the errors quoted in Table III in a known and easily calculatable way. The biases against low momentum transfer events are more difficult to take into account since they are not well known and would affect the different final states unequally. However, we do point out that these biases are probably most important for the final state $pN^*(1400)$ and when compared to the uncertainty in the mass and width of the $N^*(1400)$ resonance are probably negligible.

C. One-Pion-Exchange Model

A one-pion-exchange calculation has been made for the final state $N^{*++}(1236)p\pi^-$ using a Monte Carlo technique to generate events distributed according to:[21]

$$\frac{d^4\sigma}{dM^2 d\Delta^2\, d\Omega} = \text{const.} \times q^2 \frac{\Delta^2+(m_p+m')^2}{(\Delta^2+\mu^2)^2}\, k\, M \frac{d\sigma(M)}{d\Omega} \tag{4.6}$$

where $$q^2 = \frac{1}{4m'^2}\left(\left(\Delta^2 + (m_p-m')^2\right)\left(\Delta^2 + (m_p+m')^2\right)\right) \tag{4.7}$$

$$k = \frac{1}{M}\left(\frac{M^4}{4} - \frac{1}{2}M^2(m_p^2+\mu^2) + \frac{1}{4}(m_p^2-\mu^2)^2\right)^{1/2} \tag{4.8}$$

Δ^2 = four-momentum transfer squared to the recoil baryon m'; a N*(1236) in this case;

μ = mass of the pion; m_p = mass of proton;

M = invariant mass of the particles emerging at vertex b of Fig. 11(d); e.g., the $p\pi^-$;

$\frac{d\sigma(M)}{d\Omega}$ is the differential cross section for the two-body production at vertex b, $\pi^- p \to \pi^- p$;[22]

q is the three-momentum of the initial proton, p_A, in the rest frame of m', the N*(1236);

k is a kinematic factor, the three-momentum of the exchanged meson in the $\pi^- p$ center-of-mass frame consistent with the actual two-body scattering at energy M.

A Monte Carlo technique is used because it is very flexible and easily used to compare the theory with the experiment. In the generation of the events we choose the mass of the $N^*(1236)$ within the limits used to select the data and weight the events with the appropriate factor to take into account the mass and width of this resonance. Any other procedure applied to the actual data can also be applied to the Monte Carlo events. Thus the procedure of selecting the smaller value of the momentum transfer and rejecting events with both $p\pi^+$ combinations in the $N^*(1236)$ band can both be reflected in the theoretical distributions we calculate. In addition, we can include a form factor to bring the theoretical Δ^2 distribution into agreement with the experimental distribution. This is necessary since the momentum transfer distribution imposes kinematic restrictions on the values the other variables may assume. We have chosen to use the simple multiplicative form factor

$$e^{-\alpha\Delta^2} . \qquad (4.9)$$

Figures 16 and 17 show the Δ^2 distribution of the selected $N^{*++}(1236)$ and the effective mass spectrum of the $p_2\pi^-$ combination respectively when we select events from the $pp\pi^+\pi^-$ final states such that the $p_1\pi^+$ effective mass is in the region 1160 to 1280 MeV/c^2 and the $p_2\pi^+$ effective mass is outside this band. In addition the $p_1\pi^+\pi^-$ effective mass is restricted to values greater than 1800 MeV/c^2. Note that these are the same criterion used to select the events in the shaded area of Fig. 15 which was discussed in Section A. At that time, we pointed out that it appears that a significant proportion of the $N^{*++}(1236)$ selected by these cuts is not produced alone at a vertex as shown in Fig. 11(d). In fact, we were unable to obtain a reasonable fit to Δ^2 and $p_2\pi^-$ mass distribution

using only the simple one-pion-exchange model described so far. We have found that it is necessary to include in our calculations a background in which the $N^{*++}(1236)$ is produced at the same vertex as the π^-. We use a constant vertex factor at the $N^*(1236)\pi^-$ vertex times the appropriate phase space and resonance factors. We have assumed that this background also has a momentum transfer dependence given by

$$\frac{\Delta_2^2 \, e^{-\alpha\Delta_2^2}}{(\Delta_2^2+\mu^2)^2} \tag{4.10}$$

which includes the factors due to the virtual pion propagator, the $\pi^0 pp$ vertex, and a form factor. The variable, Δ_2^2, is the four-momentum transfer squared from the initial proton to the final state proton, p_2.

By varying the value of α and the fraction of the events, β, attributed to our assumed background, we have fit simultaneously the Δ^2 distribution of the $p_1\pi^+$ particle combination shown in Fig. 16 and the $p_2\pi^-$ effective mass distribution of Fig. 17. The best fit was obtained with $\alpha = 6.75 \pm .55$ and $\beta = .46 \pm .04$. The curves shown in Figs. 16 and 17 were calculated by Monte Carlo techniques using the above values of α and β. The χ^2 for 40 degrees of freedom in the Δ^2 distribution of Fig. 16 is 50, and for the 35 degrees of freedom in the $p_2\pi^-$ mass distribution of Fig. 17 it is 65. The overall agreement between the data and our simple one-pion-exchange model is quite reasonable and certainly suggest that one-pion-exchange is indeed a contributing production mechanism.

V. FINAL STATE $np\pi^+\pi^+\pi^-$

A. General Features

The addition of another pion to the final state increases to a large degree the complications encountered in analyzing this final state. The baryon-meson mass spectra are presented in Fig. 18. The two distributions which involve only one of the π^+ mesons have two effective masses plotted per event due to the indistinguishability of the two final state π^+'s. Only the N*(1236) is produced in amounts sufficient to be readily detected in the total sample of events and then only in the $I_Z = 3/2$ $p\pi^+$ and $I_Z = -3/2$ $n\pi^-$ states. The baryon-meson-meson mass spectra are presented in Fig. 19. The plots with only one π^+ have two effective masses per event as before. The baryon-meson-meson-meson mass spectra are shown in Fig. 20. Strong resonance production is not oberved in any of the mass plots of Fig. 19 and 20.

These remarks do not exclude the possibility that a large percentage of the events are still pseudo-two-body but, as we shall see, only indicate that individual pseudo-two-body final states have small cross sections. Many pseudo-two-body final states are possible in addition to the pN^{*+} and nN^{*++} such as $N^{*++}N^{*o}$ and $N^{*+}N^{*+}$. Reflections from this multitude of resonances would tend to obscure resonances in the effective mass plots. A further complication arises when, as we have seen in the four-body final states, a resonance cascades and produces another resonance as a decay product. We do not wish to confuse the decay product with the primary resonance production of the pp interaction if we can avoid it. For example, the $N^{*-}(1236)$ resonance seen in the effective mass spectrum of Fig. 18(d) is a likely candidate for production as a

decay product since it cannot be formed as an isolated resonance at a vertex by simple particle exchange.

Another general feature found in the analysis of the four-body final state $pp\pi^+\pi^-$ discussed in Section IV is the peripheral nature of the production mechanism. The production angular distributions of the proton and neutron of the five-body final state $np\pi^+\pi^+\pi^-$ are shown in Figs. 21(a) and (b) respectively. By comparing the forward peaks of these distributions with the forward and backward peaks of the protons in the $pp\pi^+\pi^-$ final state shown in Fig. 10, we can see that, while the proton and neutron distributions in the five-body final state are not as sharply peaked at small angles to the beam as the protons of the four-body final state, there is still an ample indication that a peripheral production mechanism is important.

We note that the backward peaks of the proton and neutron angular distributions both contain an excess of events in violation of the required symmetry of these distributions. This asymmetry is too large to be explained by a statistical fluctuation or the fact that we have chosen to display only unambiguous events in our distributions. We attribute these excess events to spurious fits to the $np\pi^+\pi^+\pi^-$ final state in which the proton and neutron are both found to lie in the backward hemisphere.

The final state $pp\pi^+\pi^-\pi^0\pi^0$ appears to be the most likely source of the fake fits. The misidentification can arise when a proton with a momentum of about 3.0 GeV/c in the laboratory system is fit as a π^+. At this momentum the bubble density information for such a track is no longer useful in distinguishing between these two mass hypothesis.

In the center-of-mass system, when the proton is produced along the beam direction it will have a center-of-mass momentum of about 0.6 GeV/c. This happens to be the most probable value in the center-of-mass system for the momentum of a proton in the above six-body final state. Further, if the $\pi^o\pi^o$ combination also has its most probable effective mass value, about 0.45 GeV/c^2, and a small resultant momentum,

then the energy and momentum equations can easily be balanced by calling the neutral particle combination a neutron. The 3.0 GeV/c track when fit as a π^+ yields a π^+ in the center-of-mass system of 0.8 GeV/c. The excess momentum in the forward direction must be balanced by a momentum component in the backward direction which is assigned to the neutron. Thus, the neutron will be found most often to lie in the backward hemisphere in the center of mass along with the second proton as we have observed. In addition, there should be an excess of π^+ mesons with a center-of-mass momentum in the region of 0.8 GeV/c and, indeed, this is what we observe when we compare the events with both the neutron and proton backward in the center of mass with those events in which both the neutron and proton are forward.

We have corrected the number of events and the total cross section for this final state listed in Tables I and II to take into account the presence of these fake events. This was done by estimating the number of excess events in the 0.8 GeV/c region of the π^+ momentum spectrum in the total center-of-mass system when both the proton and neutron were backward. Also, another estimate was made by subtracting the number of forward neutrons from the number of backward protons. Both estimates were in agreement with each other and for the sample of film used to

find the total cross sections gave 196 ± 14 fake events. In the total sample of 5244 events plotted for this final state, approximately 386 are considered as fakes. We have not eliminated these fake events from our plots since any cuts on the data would also remove some real events and might introduce biases. Also, a study of these fake fits has shown that they are distributed in a smooth phase space manner in the mass plots of interest and will not produce any fake resonance type peaks in these plots.

B. Resonant Search

1. The ρ Meson

An unresolved question in pp interactions has been that, while the ω and η mesons[16,17] are produced in pp interactions, the ρ meson has not been reported. As we can see in Fig. 22, the $\pi^+\pi^-$ mass spectrum does not show any conclusive evidence for the existence of a ρ^o but we have been forced to include two effective masses per event due to the indistinguishability of the two π^+ mesons. We can effectively select for the appropriate π^+ by requiring that the other π^+ be a decay product of an $N^{*++}(1236)$. In the same manner as in the four-body final state we take as the N^{*++} the $p\pi_1^+$ combination in the band 1160 to 1280 MeV/c^2 and we also require that the $p\pi_2^+$ effective mass be outside the mass region from 1120 to 1320 MeV/c^2. In addition, since we are looking for a $\pi^+\pi^-$ resonance, we require that the $n\pi^-$ combination be outside the 1236 resonance region from 1120 to 1320 MeV/c^2. In Fig. 23 the resulting $\pi_2^+\pi^-$ effective mass is plotted and, as we can see, there is now a well defined resonant peak in the effective mass region corresponding to ρ^o production. Taking as our background distribution a curve smoothly continued from the region below the resonant peak to the region above the resonant peak, we find 85 events above background in the resonance region. Since several mass cuts have been made on the data to obtain the selected events shown in Fig. 23, we must consider what the detection efficiency is for observing the ρ^o in this sample of events. The detection efficiency has been calculated assuming that the ρ^o has a mass of 760 MeV/c^2, a width of 120 MeV/c^2, does not interfere with the background, and is produced only in the final state $nN^{*++}(1236)\rho^o$. A peripheral production model

was used for this calculation in which the neutron is produced at one vertex with a constant vertex factor, a pion is exchanged, and the N*(1236) and ρ are produced at the other vertex, again with a constant vertex factor. Using this model, we write the differential cross section for the final state nN*(1236)ρ as

$$\frac{d^2\sigma}{dm^2 d\Delta^2} = \text{const.} \times \frac{\Delta^2}{(\Delta^2+m_\pi^2)^2} \frac{P}{m} e^{-\alpha\Delta^2} \qquad (5.1)$$

where Δ^2 is the four-momentum transfer squared to the neutron and P/m is the two-body phase space factor for the N*ρ vertex when P is the three momentum of the ρ or N* in the ρN* center of mass and m is the ρN* effective mass. The factor $\Delta^2/(\Delta^2+m_\pi^2)^2$ is included because of the pion propagator in our peripheral model. The exponential dependence on the momentum transfer, $e^{-\alpha\Delta^2}$, is a form factor used to bring the predicted Δ^2 distribution into agreement with the experimental Δ^2 distribution. We obtain good agreement between the experimental and predicted Δ^2 distributions for $\alpha = 1.0 \pm 0.5(\text{GeV}/c)^{-2}$. The calculation was done using Monte Carlo techniques to generate events distributed according to Eq. (5.1). The resonance shape of the $p\pi_1^+$ mass distribution for N*(1236) production (Eq. A.6) and the resonance shape of the $\pi_2^+\pi^-$ mass distribution for ρ^0 production were included by choosing the N* and ρ masses over their allowed mass regions and weighting the Monte Carlo events appropriately. No attempt was made to include any possible effects of the decay angular distributions of the N*(1236) or the ρ. Applying the same mass cuts used on the experimental data to the Monte Carlo events and counting only those events which have a $\pi_2^+\pi^-$ effective mass between 640 and 840

MeV/c^2 we find that the detection efficiency is 0.22 ± 0.02. The cross section for ρ^o production in this reaction channel is thus found to be 228 ± 46 μb. We note that our calculated detection efficiency is model dependent and this cross section is only our best estimate.

2. The NN* Final States

At this point we wish to investigate the final state nN^{*++} where the N^{*++} subsequently decays into $p\pi^+\pi^+\pi^-$. In Fig. 20(a) it is difficult to see any indications for such a final state but, since no selections have been made, backgrounds due to resonance production in other possible final states can tend to obscure any resonant peaks. This final state is interesting since, due to isotopic spin considerations, any resonance produced in this final state must be an I=3/2 resonance. We first select events with $n\pi^-$ effective masses less than 1120 MeV/c^2 or greater than 1320 MeV/c^2 since the formation of $N^{*-}(1236)$ is inconsistent with the final state we wish to examine and, as we can see in Fig. 18(d), events involving production of the $N^{*-}(1236)$ are an important source of background. The first histogram of Fig. 24 shows the $p\pi^+\pi^+\pi^-$ effective mass spectrum after removal of events with the $n\pi^-$ effective mass in the $N^*(1236)$ band. The curve shown is intended to be typical of the nonresonant backgrounds occurring in this mass plot. In particular the curve is a sum of the two backgrounds which would result from the final states $np\pi^+\pi^+\pi^-$ and $nN^{*++}(1236)\pi^+\pi^-$ when we require that the $n\pi^-$ effective mass is outside the $N^*(1236)$ band as we have done for the experimental data. We assume also that these two final states occur in the ratio of 2 to 1 in order to correspond to the observed $N^{*++}(1236)$ production in the events selected as above.

We believe that the peak observed in this mass plot at about

2100 MeV/c^2 is due to the production of an I=3/2 zero-strangeness baryon resonance which subsequently decays into $p\pi^+\pi^+\pi^-$. Using as an estimate of the background a curve smoothly continued from the region below the resonance peak to the region above 2200 MeV/c^2 we find 125 events above background in the resonance region from 1950 to 2200 MeV/c^2. The calculated detection efficiency for this resonance is found to be 0.49 ± 0.13 by taking into account the events lost due to the $n\pi^-$ mass cut and assuming that 70% of the resonance events are in the range counted. The production cross section for this resonance is thus found to be 151 ± 47 μb.

Further evidence for resonance production as opposed to statistical fluctuations is obtained when we require that at least one of the $p\pi^+$ effective masses be in the band 1220 ± 60 MeV/c^2 in addition to the $n\pi^-$ mass cut. The resulting effective mass distribution is shown as the first shaded histogram of Fig. 24. As we can see the number of events in the resonant peak has remained relatively unchanged but the background has been significantly reduced. The fact that the size of the peak is not noticeably changed by the requirement that the $p\pi^+$ effective mass be in the N*(1236) band is consistent with assuming that the observed N* cascades with an N*(1236) as an intermediate decay product as opposed to immediately breaking up into the four observed final state particles, $p\pi^+\pi^+\pi^-$. An additional selection on the production angle of the neutron can be made to take advantage of the peripheral nature of the psuedo-two-body reactions. The second shaded histogram of Fig. 24 shows the $p\pi^+\pi^+\pi^-$ mass spectrum where in addition to the $n\pi^-$ and $p\pi^+$ mass cuts we have required that the absolute value of the cosine of the production angle of the neutron with respect to the incident beam direction in the total

center-of-mass system must be greater than or equal to 0.9 (i.e., $|\cos\theta_n| \geq 0.9$ where θ_n is the production angle of the neutron). The resonance to background ratio is now about one to one as compared to a resonance to background ratio of approximately one to four when only the $n\pi^-$ mass cut is made.

The selection criteria used here are similar to those used to isolate events associated with ρ production in the previous section. Thus, let us consider the following decay scheme

$$N^* \rightarrow \underset{\hookrightarrow p\pi^+}{N^{*++}(1236)}\underset{\hookrightarrow \pi^+\pi^-}{\rho^0} \qquad (5.2)$$

Figure 25 shows the $p\pi^+\pi^+\pi^-$ effective mass spectrum of events for which the $n\pi^-$ effective mass is less than 1120 MeV/c^2 or greater than 1320 MeV/c^2, $|\cos\theta_n| \geq 0.9$, the π_1^+p effective mass is in the band 1220 ± 60 MeV/c^2, and the $\pi_2^+\pi^-$ effective mass is in the band 740 ± 100 MeV/c^2 (i.e., the experimental ρ band). Resonance production is still observed at about 2100 MeV/c^2. An attempt to explain the observed peak as a kinematic effect due to the peripheral production of the $N^*\rho$ mass combination was made[23] since it is well known that the kinematics of such a reaction would enhance the low mass values of the $N^*\rho$ mass spectrum. As in the previous section, events were generated using Monte Carlo techniques which were distributed according to Eq. (5.1) for $pp \rightarrow nN^{*++}\rho$. In addition, events were generated for $pp \rightarrow nN^{*++}\pi^+\pi^-$ with a three-body phase space factor replacing P/m in Eq. (5.1). Again, we used $\alpha = 1.0\ (\mathrm{GeV}/c)^{-2}$. The same mass cuts and angle cuts made on the experimental data were also made on the Monte Carlo events. Since the background under the ρ^0 peak in the sample of events investigated here is roughly equal to the reso-

nance production, the two types of Monte Carlo events were combined in the same proportion. The resulting "peripheral phase space" is shown as the smooth curve of Fig. 25. The fit to the experimental histogram is poor; χ^2=27 for nine constraints. We conclude that a kinematic effect is not responsible for the observed enhancement.

Further evidence of resonance production is seen in the decay distribution of the N*(1236) in the N*(1236)ρ center of mass with respect to the initial state proton which results in the minimum momentum transfer to the N*ρ system. Figures 26(a) and (b) show this decay distribution for events in the resonance region defined as 2080 ± 100 MeV/c^2 and outside this region respectively. Both of these distributions suffer from small statistics but the indication is that in the resonance region shown in Fig. 26(a) there is a forward-backward peaking suggestive of resonance production and decay while the non-resonant events of Fig. 26(b) have only a small forward peak.

The parameters and quantum numbers such as the mass, width, spin and parity are difficult to establish due to the limited statistics available and the complications arising from the fact that four final-state particles are produced. If we attempt to fit the mass and width assuming that four ($p\pi^+\pi^+\pi^-$) or even three ($N^{*++}(1236)\pi^+\pi^-$) particles are produced and using a simple Breit-Wigner distribution, the fit indicates that we are seeing a resonance with a mass of about 2080 MeV/c^2 and a width of approximately 200 MeV/c^2 not previously detected. If we consider only those events in which the resonance decays into an N*(1236) and a ρ meson we are in a somewhat better position since we can now use a more sophisticated Breit-Wigner which includes a momentum-dependent partial wdith (Appendix B).

Still unknown, of course, are the spin and parity of this resonance which determines the angular momentum, ℓ, of the decay into $N^*(1236)\rho$ and thus the degree of the momentum dependence of the partial width. In addition, the energy dependence of the total width is also unknown. However, using a constant total width, the trend is that the higher the ℓ value the smaller the value of the resonance mass required to reproduce the peaking in the 2100 MeV/c^2 region.

We have assumed that the resonance is due to the $N^*(1950)$ which has spin-parity $7/2^+$ and calculated the resulting $N^{*++}(1236)\rho^0$ effective mass distribution using Monte Carlo techniques to generate events with the apppropriate cuts on the $n\pi^-$, $p\pi_1^+$, $\pi_2^+\pi^-$ effective masses and the cut on the production angle of the neutron. The mass and width of the $N^*(1950)$ were taken as 1940 MeV/c^2 and 190 MeV/c^2 respectively. The momentum dependence of the partial width was calculated using Eq. (B.1) with X = 0.20 GeV/c and $\ell = 3$. As we can see, the resulting distribution shown by the dashed curve in Fig. 25 is in reasonable agreement with the data. The best fit to the experimental effective mass histogram is obtained with a sum of "peripheral phase space" and resonance production. This fit indicates that 55 ± 15% of the events shown in Fig. 25 are due to production of the $N^{*++}(1950)$.

The determination of the spin and parity of the resonance seen here must await the accumulation of more events in this channel or another experiment designed to observe the $N^*(1236)\rho$ system in this energy region. A $7/2^+$ assignment would certainly confirm the $N^*(1950)$ interpretation and its decay into $N^*(1236)\rho$ in addition to increasing our knowledge of resonance cascade processes and the effect of such processes on the shape

and positions of resonances.

The $n\pi^+\pi^+\pi^-$ effective mass distribution can also be examined for resonance production in the same manner as the $p\pi^+\pi^+\pi^-$ effective mass. In this case we require that $|\cos\theta(p)| \geq 0.9$ where $\theta(p)$ is the production angle of the proton and in addition restrict both $p\pi^+$ effective mass combinations to be outside the N*(1236) band defined as 1220 ± 100 MeV/c^2. The resulting distribution is shown in Fig. 27. No significant resonance production is observed in this mass plot.

3. Other Pseudo-Two-Body Final States

In those selections made previously on the $np\pi^+\pi^+\pi^-$ reaction channel we have been interested in those final states in which events with the production and decay into $n\pi^-$ of an $N^{*-}(1236)$ were considered as background. It is now interesting to examine those events in which production of the $N^{*-}(1236)$ is observed. The $N^{*-}(1236)$ could be produced through pion or other one particle exchange mechanisms at a vertex in association with one or more pions but its production alone at a vertex would not be possible without the exchange of an I = 2 particle.

In Fig. 28 we show a scatter plot for those events with $M(n\pi^-)$ in the range 1160 to 1280 MeV/c^2 of the $p\pi_1^+$ effective mass versus the $(n\pi^-)\pi_2^+$ effective mass where we have chosen as the $p\pi_1^+$ combination that $p\pi^+$ combination with the smallest momentum transfer. As we can see there is a band corresponding to an $N^{*++}(1236)$ in the $p\pi^+$ effective masses and a clustering of points in the region corresponding to formation of $N^{*o}(1520)$ and $N^{*o}(1688)$ in the $(n\pi^-)\pi^+$ effective mass. This suggests the formation of the pseudo-two-body final states $N^{*++}(1236)$ $N^{*o}(1520)$ and $N^{*++}(1236)$ $N^{*o}(1688)$ and the cascade sequence

$$N^{*o} \rightarrow N^{o-}(1236)\ \pi^+ \qquad (5.3)$$
$$\quad\ \ \hookrightarrow n\pi^-$$

The $n\pi^-\ \pi_2^+$ mass distribution is shown in Fig. 29 for those events which meet the following criteria: $M(n\pi^-)$ in the band 1160 to 1280 MeV/c^2, $M(p\pi_1^+)$ in the band 1160 to 1280 MeV/c^2, and, as before, the momentum transfer to the $p\pi_1^+$ system is less than the momentum transfer to the $p\pi_2^+$ system. Again, as shown in the shaded area of this figure,

an enhancement of the resonances observed and a reduction in background is achieved by exploitation of the peripheral nature of these pseudo-two-body final states by requiring that the absolute value of the cosine of the production angle of the $p\pi_1^+$ combination be greater than or equal to 0.9. The estimation of a background distribution for this mass plot is somewhat difficult. Simple kinematic phase space does not agree well with the observed distribution of events even in the region above 1900 MeV/c^2 which is most likely to be due to nonresonant background and is thus certainly unsatisfactory in describing the expected background under the resonance peaks. Using Monte Carlo techniques, we have calculated various "peripheral phase space" distributions, including those with single and double N*(1236) production, taking into account the mass cuts made on the data. In addition, we have compared other $N\pi\pi$ mass spectrum, in which we expect the resonance production to be small and on which we can make similar mass cuts, to this mass plot and the calculated distributions. We have concluded that the background distribution is best characterized by a smoothly increasing curve which peaks in the region from 1800 to 1900 MeV/c^2 and then falls to zero. Further, we find that from 55 to 60 percent of the events shown in the unshaded histogram of Fig. 29 should be considered as background. The N*(1520) peak is found to contain from 120-136 events and the N*(1680) peak is found to contain from 143-173 events. Correcting for the detection efficiency, we find that the production cross section for the $N^{*++}(1236)$ $N^{*0}(1520)$ final state in this reaction channel is from 169 ± 38 to 191 ± 42 μb. For the $N^{*++}(1236)$ $N^{*0}(1680)$ final state we find a production cross section of 201 ± 45 to 243 ± 53 μb. It is interesting to note that based on the observed cross section for the

production of the $N^{*++}(1236)$ $N^{*o}(1520)$ final state in the reaction $pp \rightarrow pp\pi^+\pi^-$ and an inelasticity of 45 percent for the $N^*(1520)$ we could expect as much as 270 ± 41 μb for $N^{*++}(1236)N^{*o}(1520)$ in this channel if the inelastic decays were 100 percent $N^*(1236)\pi$. Similar calculations for the 1680 peaks predict a production cross section for $N^{*++}(1236)$ $N^{*o}(1680)$ in this channel which could lie between 101 and 281 μb depending on the mixture of D_{15} and F_{15} resonances in the 1680 peak.

Selections for other pseudo-two-body final states in this reaction channel such as $N^{*o}(p\pi^-)$ $N^{*++}(n\pi^+\pi^+)$ and $N^{*+}(n\pi^+)N^{*+}(p\pi^+\pi^-)$ are, in general, less satisfying. The lack of significant production of the $I_Z = \pm 1/2$ $N^*(1236)$ resonances as compared to background in the $p\pi^-$ and $n\pi^+$ mass plots of Figs. 18(b) and (c) makes the selection for these resonances by mass cuts very questionable. In addition, to select against production of the $I_Z = \pm 3/2$ $N^*(1236)$ resonances in an attempt to reduce the background cuts the number of events available for investigating these pseudo-two-body final states to the point where the statistical significance of any enhancements in the mass spectra is quite small. Finally, as more mass cuts and other criteria are imposed on the data the kinematic restrictions implied become more important and at the same time more difficult to properly take into account.

With these remarks in mind let us examine the $n\pi_1^+$ and $p\pi_2^+\pi^-$ mass spectrum shown in Fig. 30(a) and (b) respectively. The selection criterion are as follows: $n\pi_1^+$ is that $n\pi^+$ combination with the smallest absolute momentum transfer in the spirit of the double del squared model (DDSQ) and the $p\pi_1^+$ and $n\pi^-$ effective masses are both outside the $N^*(1236)$ resonance region, 1120 to 1320 MeV/c^2. The shaded areas of these two

plots correspond to the additional requirement that the $|\cos\theta(n\pi_1^+)| \geq 0.9$ in order to take advantage of the assumed peripheral nature of the reaction. As we can see, resonance production of $N^{*+}(1236)$ is suggested by an enhancement at 1220 MeV/c^2 in Fig. 30(a) and enhancements appropriate to the production of the I = 1/2 N*'s 1520 and 1680 are present in both Figs. 30(a) and (b). Further studies of these events intended to isolate a given pseudo-two-body final state such as $N^{*+}(1236)\ N^{*+}(1520)$ are unproductive due to the limited nature of the available statistics.

The search for a possible $N^{*o}(p\pi^-)\ N^{*++}(n\pi^+\pi^+)$ final state is the most difficult and unproductive. For the sake of completeness we present the $p\pi^-$ and $n\pi^+\pi^+$ mass spectra in Figs. 31(a) and (b) respectively for those events in which both $p\pi^+$ effective masses are outside the region 1120 to 1320 MeV/c^2. Again, the shaded area is for those events which also have $|\cos\theta(p\pi^-)| \geq 0.9$.

VI. FINAL STATE $pp\pi^+\pi^-\pi^o$

A. General Features

The remarks made concerning the $np\pi^+\pi^+\pi^-$ final state are, in general, still true of the $pp\pi^+\pi^-\pi^o$ final state. Figures 32, 33, and 34 show the baryon-meson, baryon-two-meson and baryon-three-meson mass plots respectively. Only the N*(1236) is produced in significant amounts. The $p\pi^+$ mass spectrum shows that again the $I_Z = 3/2$ N*(1236) is produced copiously. The $p\pi^o$ mass spectrum shows some $N^{*+}(1236)$. As before, the $N^{*o}(1236)$ in the $p\pi^-$ mass spectrum is obscured by a very large non-resonant background. Each of the mass plots in Figs. 32, 33 and 34 has two points per event due to the indistinguishability of the final state protons.

The production angular distribution of the final state protons is presented in Fig. 35. Compared to Fig. 10 we can see that the protons are again peaked forward-backward but not as sharply as in the $pp\pi^+\pi^-$ final state.

The most striking feature of these events is the ω meson production. The $\pi^+\pi^-\pi^o$ mass spectrum in Fig. 36 has a very pronounced ω peak. The partial cross section for ω production is estimated to be 104 ± 12 μb in this reaction channel. From the width of the observed ω peak we estimate that the mass resolution in this final state is approximately 25 MeV/c^2. At the lower end of the allowed kinematic region where phase space is small, we see an enhancement which we attribute to the production of the η meson corresponding to a cross section of about 28 ± 5 μb.

The two pion effective masses in the unselected data show no

significant enhancements at the ρ mass as we can see in Fig. 37. This indicates that as in the $np\pi^+\pi^+\pi^-$ channel we must select for those final states in which ρ production is most probable.

B. Resonant Search

1. The ρ Meson

In the $pp\pi^+\pi^-\pi^0$ reaction channel there are three two-pion effective mass distributions to be examined for evidence of ρ production. As we have done with events in the $np\pi^+\pi^+\pi^-$ reaction channel, we will select the events in an attempt to enhance the $NN^*\pi\pi$ final states. We note that, due to the differing resonance to background ratios in the observed $N^*(1236)$ peaks in Fig. 32, we may expect the success of our selection procedure to vary considerably among the three final states of interest.

An additional selection criterion will be that the $\pi^+\pi^-\pi^0$ mass for the events studied must be outside the range 720 to 840 MeV/c^2. This is done in an attempt to minimize the reflections of the ω meson decay into the two-pion effective mass distributions. A somewhat larger band than necessary of the $\pi^+\pi^-\pi^0$ effective mass distribution was eliminated, but calculations of the $\pi\pi$ mass spectrum appropriate to the $NN^*\pi\pi$ final state indicate that this procedure has a negligible effect on the shape of our estimated background. In addition, it can be shown that the existence of the observed ρ peaks is not dependent on this selection.

In Fig. 38 we present the $\pi^-\pi^0$ mass spectrum for events with one or both of the $p\pi^+$ effective mass combinations be in the 1236 resonance region (1160 to 1280 MeV/c^2). As we can see, the ρ^- is present in these selected events although it was hidden in the total sample by

non-resonant background and reflections. We find 132 events in the ρ^- peak, which when corrected for a detection efficiency of 0.50 ± 0.05 due to the mass cuts and including the uncertainty of the shape and normalization of the background, yields a cross section of 153 ± 31 μb for ρ^- production in the $pp\pi^+\pi^-\pi^o$ reaction channel. There are, of course, two protons in this final state and while we have selected events so that one is the decay product of an $N^{*++}(1236)$ it is still possible that the other is resonant with either the π^o, π^- or both $\pi^o\pi^-$. However, the $p\pi^o$ mass spectrum is the only one showing any significant resonance production as we have seen in Fig. 32. The shaded histogram of Fig. 38 shows the effect of the additional requirement that the $p_2\pi^o$ mass be outside the range 1120 to 1320 MeV/c^2 when p_1 is the proton such that the $p_1\pi^+$ effective mass is in the N*(1236) band (1160 to 1280 MeV/c^2). If both $p\pi^+$ effective masses are in the N*(1236) band, the event is discarded. As we can see, the ρ^- peak remains and its size is consistent with the reduced detection efficiency attributable to the additional mass cut.

Figure 39 shows the $\pi^+\pi^-$ mass spectrum for those events for which either of the $p\pi^o$ effective masses is in the range 1160 to 1280 MeV/c^2. The shaded area includes only those events in this sample which in addition have the two $p\pi^+$ masses outside the N*(1236) mass region (1120 to 1320 MeV/c^2). We find 39 events in the ρ^o peak of the unshaded mass plot which yields a corrected cross section for ρ^o production of 45 ± 12 μb.

The evidence for production of ρ^+ is shown in Fig. 40 where now we require one or both of the $p\pi^-$ effective mass combinations to be in the 1160 to 1280 MeV/c^2 range. Again the shaded area is that subset

of these events with both $p\pi^+$ effective masses outside the N*(1236) mass region. The partial cross section for ρ^+ production in this reaction channel is found to be 65 ± 18μb.

In Table IV we compare the observed cross sections for ρ production with ratios predicted by isotopic spin considerations for four possible cases. Case I assumes the ρ is produced at a vertex with an N*(1236) through an I = 1/2 amplitude. Case II assumes production as in Case I except that it is through an I = 3/2 amplitude. Cases III and IV assume production of ρ in association with a nucleon through I = 1/2 and I = 3/2 amplitudes respectively. The observed ratios are not consistent with any one of these models. However, if we only consider these four cases, it is obvious that Case II must be included to account for the observed ρ^+ production and the decay of the N*(1950) into N*(1236)ρ^0 discussed previously.

2. <u>The Pseudo-Two-Body Final States</u>

In Fig. 41 we present the $p_2\pi^+\pi^-\pi^0$ effective mass for those events with p_1 chosen by the double del squared method to have the minimum momentum transfer, $M(p_1\pi^+)$ outside the effective mass region 1120 to 1320 MeV/c^2, $M(\pi^+\pi^-\pi^0)$ effective mass outside the ω region defined as 720 to 840 MeV/c^2, and $|\cos\theta(p_1)| \geq 0.9$. Three possible resonant peaks are seen at approximately 1700, 2050, and 2200 MeV/c^2 respectively. Only the peak at 1700 can be separated from the background distribution easily. We estimate that there are 31 events in this peak. Using a detection efficiency of 0.65 ± 0.15, this corresponds to a partial cross section of 28 ± 9μb for the production of the pN*(1680) final state in this reaction channel. The other two peaks are much more

difficult to disentangle from the background. First, we are uncertain as to the shape of our background distribution or even which of the many possible final states contribute to it. Second, the N*(2190) is a broad resonance with a total width of 250 MeV/c^2. In addition, if we identify the peak at 2050 MeV/c^2 with the N*(1950) as we did in the previous section, then its width is approximately 200 MeV/c^2. These two broad resonance peaks will overlap so that there is no point between them to use in estimating a background curve. We can calculate a number of "peripheral phase space" curves which include the observed peripheralism of these events and which take into account the observed N*(1236) production. These curves are similar to the one shown in Fig. 24. Using these curves as a guide, we estimate a reasonable background and find approximately 84 events in the N*(1950) peak and 78 events in the N*(2190) peak. We note that a more pessimistic background distribution is possible which could yield counts as low as 30 and 46 events respectively in these two peaks, but it is necessary to ignore the large widths of these resonances if it is used. Using the more optimistic background and a detection efficiency of 0.65 ± 0.15, we obtain production cross sections of 74 ± 20μb and 69 ± 19μb respectively for the $pN^{*+}(1950)$ and $pN^{*+}(2190)$ final states in the $pp\pi^+\pi^-\pi^0$ reaction channel.

It is interesting to compare the production cross section for the $pN^{*+}(1950)$ final state with the value predicted on the basis of isospin considerations and the $nN^{*++}(1950)$ production cross section. The cross section for the $nN^{*++}(1950)$ final state, shown in Fig. 24, was found to be 151 ± 47μb. The cross section for $pN^{*+}(1950)$ production, shown in Fig. 41, is thus expected to be 52 ± 16μb. This agrees reasonably well with the value 74 ± 20μb when we consider the difficulties

and uncertainties encountered in measuring these cross sections.

Attempts to isolate N*N* final states in the $pp\pi^+\pi^-\pi^0$ reaction channel have not been very fruitful due to the fact that except for the N*(1236) in the nucleon pion systems the resonance production is too small to be resolved by this experiment. In order to conclude the search for pseudo-two-body resonance production we present proton-pion and the corresponding proton-two-pion effective mass spectra in Figs. 42, 43, and 44. Figures 42(a) and (b) show the $p_1\pi^+$ and $p_2\pi^-\pi^0$ mass spectra for those events with the $\Delta^2(p_1\pi^+) < \Delta^2(p_2\pi^+)$, $|\cos\theta(p_1\pi^+)| \geq 0.9$, and $M(p_2\pi^+)$ not in the N*(1236) band (1120 to 1320 MeV/c^2). Figures 43(a) and (b) show the $p_1\pi^0$ and $p_2\pi^+\pi^-$ mass spectra for those events with $\Delta^2(p_1\pi^0) < \Delta^2(p_2\pi^0)$, $|\cos\theta(p_1\pi^0)| \geq 0.9$, and $M(p_1\pi^+)$ not in the N*(1236) band. Finally, Figs. 44(a) and (b) show the $p_1\pi^-$ and $p_2\pi^+\pi^0$ mass spectra for those events with $\Delta^2(p_1\pi^-) < \Delta^2(p_2\pi^-)$, $|\cos\theta(p_1\pi^-)| \geq 0.9$, and $M(p_1\pi^+)$ not in the N*(1236) band. Figures 42(a) and 43(a) definitely show the presence of the N*(1236). Neither 43(a) or 44(a) show any evidence for production of the I=1/2 resonance N*(1520) or N*(1680). None of the proton-two-pion effective mass distributions show any firm evidence of baryon resonance production.

VII. CONCLUSIONS

To summarize the results of this experiment which involved the three reactions studied in detail in Sections IV, V, and VI, the following points must be made.

(a) In the $pp\pi^+\pi^-$ reaction channel, nuclear isobar formation is strong and the production of psuedo-two-body final states is a striking feature. To a lesser extent, the pseudo-two-body processes are also found in the five-body final states $np\pi^+\pi^+\pi^-$ and $pp\pi^+\pi^-\pi^o$.

(b) The peripheral nature of the pseudo-two-body processes is a characteristic and dominant feature of the production mechanism.

(c) Resonances, especially the N*(1236), are produced as the decay products of higher mass resonances in cascade decay processes and any attempt to measure and compare the decay angular distributions of a resonance with a model which assumes that it is produced at a vertex by a one particle exchange process will be incorrect if this source of resonance production is not taken into account.

(d) An enhancement has been observed in the $p\pi^+\pi^+\pi^-$ and $p\pi^+\pi^-\pi^o$ mass spectra of reactions (1.7) and (1.8) at about 2080 ± 30 MeV/c^2 with an apparent width of approximately 200 MeV/c^2. While the possibility of a new resonance cannot be ruled out, we have found[23] that suitable assumptions concerning resonance shape and energy dependence of the partial width can cause the N*(1950) resonance peak to be shifted to this mass region if it has an N*ρ decay mode.

(e) In addition to the ω and η meson resonances previously found

in other pp experiments at several different energies, production of the ρ meson has been detected in the five body final states $np\pi^+\pi^+\pi^-$ and $pp\pi^+\pi^-\pi^0$. The production mechanism of the meson resonances is not clear at this time.

A clearer understanding of certain points raised in this experiment clearly require more data. For example, the relative importance of the pseudo-two-body production processes in the five body final states studied here cannot be established until we are sure of being able to detect quite small production cross sections. Since the total number of possible pseudo-two-body processes in the five particle final states is much larger than in the four particle final state, individual final states have a much smaller share of the total cross section and are correspondingly harder to detect. Other questions, such as the branching ratio of the N*(1525) and N*(1680) into $N^*(1236)\pi^-$ as compared to $N\pi\pi$ and the determination of the spin and parity of the $N\pi\pi\pi$ enhancement at 2080 MeV/c^2 might best be answered in other types of experiments.

ACKNOWLEDGMENTS

I would like to express my sincere thanks and appreciation to Professor William Chinowsky who has given me both guidance and freedom in excellent proportion.

I am indebted to Dr. Jonas Schultz, Dr. Paul Condon, and Dr. Peter Schmidt for many helpful discussions during the analysis of the data presented here.

I wish to thank Professor Luis Alvarez for making the bubble chamber available. In addition, I wish to thank Mr. R. Watt and the bubble chamber crew for their careful attention to the operation of the bubble chamber during a long, arduous, and sometimes excessively dull running period. Also, a similar expression of gratitude is due the Bevatron operating crew.

I am also pleased to acknowledge the work and cooperation of the scanning and roadmaking personnel without whom this experiment would not be possible.

For the precision measurement and fitting of the events, I am indebted to Dr. Howard White and his group for the development, maintenance, and running of the FSD system.

I thank Professor Emilio Segrè for his valuable support and encouragement of this work.

I appreciate also the contribution of Mrs. Rosemary Fowell in typing this thesis.

Finally, to my wife, for her understanding and encouragement, I give my deepest thanks.

APPENDICES

A. Shape and Position of $N^*(1236)$ Peak

In order to fit the observed $N^*(1236)$ peak it is necessary to know what is the most reasonable shape to use and to understand why it is that the $N^*(1236)$ appears at approximately 1215 MeV/c^2 in production experiments, at 1222 MeV/c^2 in elastic scattering, and at 1236 in the tables of the properties of the elementary particles. Jackson[24] has shown that for production experiments we can write the cross section for production of a resonant state after integrating over all angles of the decay in the rest frame of the resonance as

$$d\sigma = d\sigma_s(\omega) \quad \frac{\omega_o \Gamma(\omega)}{(\omega_o^2 - \omega^2)^2 + \omega_o^2 \Gamma^2(\omega)} \frac{1}{\pi} \, d\omega^2 \tag{A.1}$$

where $d\sigma_s(\omega)$ is the cross section for production of a stable particle summed over the spin states of that particle in an $n + 1$ particle final state as opposed to an $n + m$ particle final state in which m is the number of particles into which the resonance decays. The other parameters in this equation are ω, the mass of the stable particle; ω_o, the mass of the resonance; and $\Gamma(\omega)$, the width of the resonance which can be defined as

$$\Gamma(\omega) = \frac{1}{32\pi^3} \frac{1}{2J+1} \Sigma \int |V|^2 \frac{q}{\omega} \, d\Omega_{12}. \tag{A.2}$$

In equation (A.2), J is the angular momentum of the resonant state,

the summation is over the spins of the resonance and the outgoing particles, the integration is over the decay distribution of the outgoing particles when $m = 2$, and V is the decay vertex amplitude.

For elastic scattering of a pair of particles through a resonant state, the scattering cross section is given by

$$\sigma_{scatt}(\omega) = \frac{4\pi}{q^2} \frac{2J+1}{(2_{j_1}+1)(2_{j_2}+1)} \frac{\omega_o^2\Gamma^2(\omega)}{(\omega_o^2-\omega^2)^2+\omega_o^2\Gamma^2(\omega)} \qquad (A.3)$$

where j_1 is the angular momentum of particle 1 and j_2 is that of particle 2. The Γ^2 factor of the numerator in (A.3) as opposed to only a Γ in (A.1) is a result of the fact that in a scattering experiment the resonance is formed and then decays while in a production experiment only the decay of the resonance is involved.

The shape and position of an observed resonance is determined mainly be the line shape factor in equations (A.1) or (A.3) but if the resonance is broad the energy dependence of the width $\Gamma(\omega)$ can cause distortion of the shape. In the case of the $N^*(1236)$ the peak position is shifted to a value below 1236 MeV c^2 and the shape is skewed to higher energies. The $N^*(1236)$ decay is a two body decay through a partial wave of orbital angular momentum $\ell = 1$. Assuming that the width of such a two body decay can be written as

$$\Gamma(\omega) \simeq \Gamma_o \left(\frac{q}{q_o}\right)^{2\ell + 1} \qquad (A.4)$$

then the shift in the peak position from (A.1) is given by

$$\frac{\omega_o - \omega_{peak}}{\Gamma_o} \simeq \frac{2\ell + 1}{8} \frac{\Gamma_o}{\omega_o} \frac{\omega_o^4 - (m_1^2 - m_2^2)^2}{\omega_o^4 - 2(m_1^2 + m_2^2)\omega_o^2 + (m_1^2 - m_2^2)^2} \tag{A.5}$$

where m_1 and m_2 are the masses of the proton and pion decay products. Using (A.5), the value of ω_{peak} for $\omega_o = 1236$ MeV/c^2 and $\Gamma_o = 120$ MeV/c^2 is found to be 1215 MeV/c^2. Starting from equation (A.3), an equation similar to (A.5) is found with $2\ell + 1$ replaced by 2 and the peak position is found to be 1222 MeV/c^2. Thus, the differences in mass values for production experiments, scattering experiments, and particle tables is explained.

The mass energy variation of (A.4) is perhaps somewhat too simplified so in the actual fitting of the data the following was used,

$$\Gamma(\omega) = \Gamma_o \left(\frac{q}{q_o}\right)^{2\ell + 1} \frac{\rho(\omega)}{\rho(\omega_o)} \tag{A.6}$$

where $\ell = 1$ and

$$\rho(\omega) = \frac{E + m}{\omega} \tag{A.7}$$

The factor given in (A.7) is found from lowest order perturbation theory with E and m being the energy and mass of the decay proton in the $N^*(1236)$ center of mass.

B. Form of Baryon Resonances Used in Fitting and Calculations

In general we will use the form for resonance production given by equation (A.1), however, several remarks are in order concerning the applicability of this equation to the more complicated baryon resonances.

1) This equation is valid only insofar as interference effects in the final state can be ignored.
2) By a suitable definition of $\Gamma(\omega)$ the equation can be generalized to more complicated final states with $m > 2$.
3) If only one mode is being considered out of several alternative decay modes, the width in the numerator of (A.1) is the partial width for that mode while the width in the denominator is the total width.

With regard to item 1), little can be done and the fits are made with the assumption of no interference effects among the final states. The width $\Gamma(\omega)$ used for those cases which can be represented by a two-body decay is

$$\Gamma_i(\omega) = \gamma_i \left(\frac{q}{q_o}\right)^{2\ell + 1} \frac{\omega_o(X^2 + q_o^2)^\ell}{\omega(X^2 + q^2)^\ell} \tag{B.1}$$

such that $\Gamma_i(\omega)$ is the partial width of the resonance into the ith channel where γ_i is the partial width at $\omega = \omega_o$; q is the three momentum of the two decay particles in the resonance center of the mass, ω; ℓ is the decay angular momentum;and X is an empirical para-

meter which is a measure of the interaction radius. This form has been employed in the fitting of baryonic resonances in the context of unitary symmetry.[25] We may still use Eq. (B.1) even if one or both of the decay products are resonances if we include an integration over the mass or masses of these resonances. If the decay is into three or more particles (resonances), we use a constant $\Gamma_i(\omega)$ since no model exists which can describe the energy dependence of the partial width of such a decay mode. The production cross section for the ith final state of a resonance is written as

$$d\sigma_i = d\sigma_s(\omega) \frac{\omega_o \Gamma_i(\omega)}{(\omega_o^2 - \omega^2)^2 + \omega_o^2 \Gamma^2(\omega)} \frac{1}{\pi} d\omega^2 \qquad \text{(B.2)}$$

where $\Gamma(\omega) = \sum_i \Gamma_i(\omega)$. Except for the N*(1236), which has essentially a 100% branching ratio into $N\pi$, the partial cross sections and branching ratios of the resonances we observe are not well known. We have assumed in our fitting procedure that the N*(1525) and N*(1688) resonances decay only into $N\pi$ and N*(1236)π in the ratio of 65%/35%. For all other resonance production the total width, $\Gamma(\omega)$, was taken to be a constant.

REFERENCES

1. D. R. O. Morrison, Review of Inelastic Two-Body Reactions, CERN/TC/PHYSICS 66-20.

2. G. Wolf, Phys. Letters 19, 925 (1967).

3. Aachen-Berlin-CERN Collaboration, Phys. Letters 12, 356 (1964).

4. R. D. Newman, K^+p Inelastic Interactions at 2.7 BeV/c (Ph. D. Thesis), UCRL-17003, July 1966.

5. G. Alexander, O. Benary, G. Czapek, B. Haber, N. Kidron, B. Reuter, A. Shapira, E. Simopoulou, and G. Yekutieli, Phys. Rev. 154, 1284 (1967).

6. H. S. White, T. Aronstein, C. Osborne, N. Webre, and W. G. Moorhead, Nuclear Instruments and Methods 20, 393 (1963).

7. S. Buckman, J. Frany, J. Gotthelfsman, D. Hall, V. Morgan, and F. Windorski, The Multi-View Fog Program and Its Application to Quality Control of FSD Data, UCRL-16508, Oct. 1965.

8. B. N. Fabian, R. L. Place, W. A. Riley, W. H. Sims, and V. P. Kenney, Rev. of Sci. Instr. 34, 484 (1963).

9. R. C. Strand, Bubble Density Measurement with the Hough-Powell Digitizer, 6-34 (B.C.) Brookhaven, 1963.

10. D. Hall, et al., Data Handling Notes 9 and 10, UCID 1930-1931, June 1963.

11. R. F. George, K. F. Riley, R. J. Tapper, D. V. Bugg, D. C. Salter, and G. H. Stafford, Phys. Rev. Letters 15, 214 (1965).

12. A. M. Eisner, E. L. Hart, R. J. Louttit, and T. W. Morris, Phys. Rev. 138, B670 (1965).

13. E. Pickup, D. K. Robinson, and E. O. Salant, Phys. Rev. 125, 2091 (1962).

14. E. L. Hart, R. J. Louttit, J. W. Morris, W. J. Willis, and S. S. Yamamoto, Phys. Rev. 126, 747 (1962).

15. J. Kidd, L. Mandelli, V. Pelosi, S. Ratti, A. Sichirollo, and L. Tallone, Phys. Letters 16, 75 (1965).

16. A. P. Colleraine, Isobar Production Mechanisms in Proton-Proton Collisions at 5 GeV/c, Princeton-Penn. Report PPAD 600F, Aug. 1966.

17. See reference 5.

18. S. P. Almeida, J. G. Rushbrooke, J. H. Scharenginvil, M. Behrens, V. Blobel, J. Borecka, H. C. Dehne, J. Diaz, G. Kines, R. Schafer, and W. P. Swanson, Higher Isobar Production in p-p Collisions at 10 GeV/c, collaboration Cavandish Laboratory, Institut fur Experimental Physik, Hamburg, and DESY, preprint.

19. K. Gottfried and J. D. Jackson, Nuovo Cimento 33, 309 (1964).

20. J. Friedman, Murtlebert, Alvarez Programming Group, Note No. P-156, University of California Lawrence Radiation Laboratory, Berkeley, Nov. 1966.

21. G. J. Chew and F. E. Low, Phys. Rev. 113, 1640 (1959).
E. Ferrari and F. Selleri, Suppl. Nuovo Cimento 24, 453 (1962).
E. Ferrari, Nuovo Cimento 30, 240 (1963).
J. D. Jackson and H. Pilkuhn, Nuovo Cimento 33, 906 (1964), Errata, Nuovo Cimento 34, 1841 (1964).

22. Differential elastic cross sections for $\pi^- p \rightarrow \pi^- p$, compiled by Mark Mandelkern, private communication.

23. W. Chinowsky, P. Condon, R. R. Kinsey, S. Klein, M. Mandelkern, P. Schmidt, J. Schultz, F. Martin, M. L. Perl, and T. H. Tan, UCRL-17651 Rev. (1968).

24. J. D. Jackson, Nuovo Cimento 35, 1644 (1964).

25. S. L. Glashow and A. H. Rosenfeld, Phys. Rev. Letters 10, 192 (1963).

FIGURE CAPTIONS

Fig. 1. Schematic of the experimental arrangement.

Fig. 2. Scatter plot of the reference ka required to normalize the measured ka and bring I_{meas} into agreement with I_{calc} for tracks with known mass assignments versus the average depth of the track in the bubble chamber (50 cm is the arbitrary center of the chamber).

Fig. 3. Distribution of $(I_{meas} - I_{calc})/I_{calc}$ for the outgoing tracks of events with good four constraint kinematic fits. (a) tracks measured in the normal mode. (b) tracks measured in the orthogonal mode.

Fig. 4. Distribution of $(I_{meas} - I_{calc})/\sigma$ for the outgoing tracks of events with good four constraint kinematic fits. (a) tracks measured in the normal mode. (b) tracks measured in the orthogonal mode.

Fig. 5. Distribution of (a) $\chi^2_{ION,\ unfitted}$ and (b) $\chi^2_{ION,\ fitted}$ for events with good four constraint kinematic fits and for which all four outgoing tracks were used in calculating the χ^2's.

Fig. 6. Mass distribution of $p\pi^+$ for the reaction $pp \rightarrow pp\pi^+\pi^-$ (5681 events).

Fig. 7. Mass distribution of $p\pi^-$ for the reaction $pp \rightarrow pp\pi^+\pi^-$ (5681 events).

Fig. 8. Mass distribution of $p\pi^+\pi^-$ for the reaction $pp \rightarrow pp\pi^+\pi^-$ (5681 events).

Fig. 9. Mass distribution of $\pi^+\pi^-$ for the reaction $pp \rightarrow pp\pi^+\pi^-$ (5681 events).

Fig. 10. Distribution of the cosine of the production angle of the final state protons in the total center of mass system for the reaction $pp \rightarrow pp\pi^+\pi^-$ (11362 protons).

Fig. 11. Feynman diagrams.

Fig. 12. Mass distribution of $p_2\pi^+\pi^-$ from the reaction $pp \rightarrow p_1p_2\pi^+\pi^-$ for events with $\Delta^2(p_1) \leq \Delta^2(p_2)$ and $M(p_1\pi^+)$ not in the N*(1236) band (3527 events).

Fig. 13. Mass distribution of $p_2\pi^-$ from the reaction $pp \rightarrow p_1p_2\pi^+\pi^-$ for events with $M(p_1\pi^+)$ in the N*(1236) band (3632 events). The shaded area includes only those events with both $M(p_1\pi^+)$ in the N*(1236) band (923 events).

Fig. 14. Mass distribution of $p_2\pi^-$ from the reaction $pp \rightarrow p_1p_2\pi^+\pi^-$ for those events with $M(p_1\pi^+)$ in the N*(1236) band and $M(p_1\pi^+\pi^-) >$ 1800 MeV/c^2 (1518 events, 1777 data points).

Fig. 15. Decay angular distribution of p_1 in the $p_1\pi^+$ rest frame from the reaction $pp \rightarrow p_1p_2\pi^+\pi^-$ for events with $M(p_1\pi^+)$ in the N*(1236) band and $M(p_1\pi^+\pi^-) >$ 1800 MeV/c^2 (1518 events, 1777 data points). The shaded area includes only those events which in addition have $M(p_2\pi^+)$ outside the N*(1236) band (1274 events).

Fig. 16. Momentum transfer distribution to $p_1\pi^+$ for those events in the $p_1p_2\pi^+\pi^-$ channel which have $M(p_1\pi^+)$ in the N*(1236) band, $M(p_2\pi^+)$ not in the N*(1236) band and $M(p_1\pi^+\pi^-) >$ 1800 MeV/c^2.

Fig. 17. Mass distribution of $p_2\pi^-$ for those events in the $p_1p_2\pi^+\pi^-$ channel which have $M(p_1\pi^+)$ in the N*(1236) band, $M(p_2\pi^+)$ not in the N*(1236) band and $M(p_1\pi^+\pi^-) >$ 1800 MeV/c^2 (1274 events).

Fig. 18. Nucleon-pion mass distributions for the reaction $pp \rightarrow np\pi^+\pi^+\pi^-$. (a) $M(p\pi^+)$, (b) $M(p\pi^-)$, (c) $M(n\pi^+)$, and (d) $M(n\pi^-)$ (5244 events).

Fig. 19. Nucleon-two pion mass distributions for the reaction $pp \rightarrow np\pi^+\pi^+\pi^-$. (a) $M(p\pi^+\pi^-)$, (b) $M(p\pi^+\pi^+)$, (c) $M(n\pi^+\pi^-)$, and

(d) $M(n\pi^+\pi^+)$ (5244 events).

Fig. 20. Nucleon-three pion mass distributions for the reaction $pp \rightarrow np\pi^+\pi^+\pi^-$. (a) $M(p\pi^+\pi^+\pi^-)$ and (b) $M(n\pi^+\pi^+\pi^-)$ (5244 events).

Fig. 21. Distribution of the cosine of the production angle of the (a) protons and (b) neutrons in the total center of mass system for the final state $np\pi^+\pi^+\pi^-$ (5244 events).

Fig. 22. Mass distribution of $\pi^+\pi^-$ for the reaction $pp \rightarrow np\pi^+\pi^+\pi^-$ (5244 events).

Fig. 23. Mass distribution of $\pi_2^+\pi^-$ for those events in the final state $np\pi_1^+\pi_2^+\pi^-$ which have $M(p\pi_1^+)$ in the N*(1236) band, $M(p\pi_2^+)$ not in the N*(1236) band, and $M(n\pi^-)$ not in the N*(1236) band (1026 events).

Fig. 24. Mass distribution of $p\pi^+\pi^+\pi^-$ for those events in the final state $np\pi^+\pi^+\pi^-$ which have $M(n\pi^-)$ outside the N*(1236) band (2521 events). The first shaded area includes those events which in addition have one or both of the $M(p\pi^+)$ in the N*(1236) band (1492 events). The second shaded area has the additional requirement that $|\cos\theta(n)| \geq 0.9$ (582 events).

Fig. 25. Mass distribution of $p\pi_1^+\pi_2^+\pi^-$ for those events in the final state $np\pi_1^+\pi_2^+\pi^-$ which have $M(p\pi^-)$ outside the N*(1236) band, $|\cos\theta(n)| \geq 0.9$, $M(p\pi_1^+)$ in the N*(1236) band, and $M(\pi_2^+\pi^-)$ in the ρ band (193 events).

Fig. 26. Decay angular distribution of the N*(1236) in the N*(1236)ρ rest frame for events in the $np\pi_1^+\pi_2^+\pi^-$ channel which have $M(n\pi^-)$ outside the N*(1236) band, $|\cos\theta(n)| \geq 0.9$, $M(p\pi_1^+)$

in the N*(1236) band and $M(\pi_2^+\pi^-)$ in the ρ band. (a) inside the resonance region and (b) outside the resonance region.

Fig. 27. Mass distribution of $n\pi^+\pi^+\pi^-$ for events in the $np\pi^+\pi^+\pi^-$ final state which have $|\cos\theta(p)| \geq 0.9$ and both $p\pi^+$ effective masses outside the N*(1236) band (216 events).

Fig. 28. Scatter plot of $M(p\pi_1^+)$ versus $M(n\pi_2^+\pi^-)$ for those events in the $np\pi_1^+\pi_2^+\pi^-$ channel selected such that $\Delta^2(p\pi_1^+) \geq \Delta^2(p\pi_2^+)$ and $M(n\pi^-)$ is in the N*(1236) band (1936 events).

Fig. 29. Mass distribution of $n\pi^-\pi_2^+$ for events in the $np\pi_1^+\pi_2^+\pi^-$ reaction channel selected for $\Delta^2(p\pi_1^+) \leq \Delta^2(p\pi_2^+)$, $M(n\pi^-)$ in the N*(1236) band, and $M(p\pi_1^+)$ in the N*(1236) band (674 events). The shaded area has the additional requirement that $|\cos\theta(p\pi_1^+)| \geq 0.9$ (444 events).

Fig. 30. Mass distributions of (a) $n\pi_1^+$ and (b) $p\pi_2^+\pi^-$ for those events in the $np\pi_1^+\pi_2^+\pi^-$ final state selected to have $\Delta^2(n\pi_1^+) \leq \Delta^2(n\pi_2^+)$ and both $M(p\pi_1^+)$ and $M(n\pi^-)$ outside the N*(1236) band (1355 events). The shaded area has the additional requirement that $|\cos\theta(n\pi_1^+)| \geq 0.9$ (573 events).

Fig. 31. Mass distributions of (a) $p\pi^-$ and (b) $n\pi_1^+\pi_2^+$ for those events in the $np\pi_1^+\pi_2^+\pi^-$ final state which have both possible $p\pi^+$ effective masses outside the N*(1236) band (1481 events). The shaded region corresponds to the added requirement that $|\cos\theta(p\pi^-)| \geq 0.9$ (427 events).

Fig. 32. Proton-pion mass distribution for the reaction $pp \rightarrow pp\,\pi^+\pi^-\pi^0$. (a) $M(p\pi^+)$, (b) $M(p\pi^0)$ and (c) $M(p\pi^-)$ (4176 events).

Fig. 33. Proton-two pion mass distributions for the reaction $pp \rightarrow pp\pi^+\pi^-\pi^o$. (a) $M(p\pi^+\pi^-)$, (b) $M(p\pi^+\pi^o)$ and (c) $M(p\pi^-\pi^o)$ (4176 events).

Fig. 34. Mass distribution of $p\pi^+\pi^-\pi^o$ for the reaction $pp \rightarrow pp\pi^+\pi^-\pi^o$ (4176 events).

Fig. 35. Distribution of the cosine of the production angle of the final state protons in the total center-of-mass system for the reaction $pp \rightarrow pp\pi^+\pi^-\pi^o$ (8352 protons).

Fig. 36. Mass distribution of $\pi^+\pi^-\pi^o$ for the reaction $pp \rightarrow pp\pi^+\pi^-\pi^o$ (4176 events).

Fig. 37. Two pion mass distributions for the reaction $pp \rightarrow pp\pi^+\pi^-\pi^o$. (a) $M(\pi^+\pi^-)$, (b) $M(\pi^+\pi^o)$ and (c) $M(\pi^-\pi^o)$ (4176 events).

Fig. 38. Mass distribution of $\pi^-\pi^o$ for those events in the $pp\pi^+\pi^-\pi^o$ channel which have either $p\pi^+$ mass combination in the N*(1236) band and $M(\pi^+\pi^-\pi^o)$ outside the ω band (1865 events). The shaded area has the additional requirement that $M(p\pi^o)$ is outside the N*(1236) band (1258 events).

Fig. 39. Mass distribution of $\pi^+\pi^-$ for those events in the $pp\pi^+\pi^-\pi^o$ channel which have either $p\pi^o$ mass combination in the N*(1236) band and $M(\pi^+\pi^-\pi^o)$ outside the ω band (1403 events). The shaded area has the additional requirement that both $p\pi^+$ mass combinations are outside the N*(1236) band (536 events).

Fig. 40. Mass distribution of $\pi^+\pi^o$ for those events in the $pp\pi^+\pi^-\pi^o$ channel which have either $p\pi^-$ mass combination in the N*(1236) band and $M(\pi^+\pi^-\pi^o)$ outside the ω band (1453 events). The shaded area has the additional requirement that both $p\pi^+$ mass combinations are outside the N*(1236) band (516 events).

Fig. 41. Mass distribution of $p_2\pi^+\pi^-\pi^o$ for those events in the $p_1p_2\pi^+\pi^-\pi^o$ channel which have $\Delta^2(p_1) \leq \Delta^2(p_2)$, $|\cos\theta(p_1)| \geq 0.9$, $M(\pi^+\pi^-\pi^o)$ outside the ω band, and $M(p_1\pi^+)$ outside the N*(1236) band (1130 events).

Fig. 42. Mass distributions of (a) $p_1\pi^+$ and (b) $p_2\pi^-\pi^o$ for those events in the $p_1p_2\pi^+\pi^-\pi^o$ channel selected such that $\Delta^2(p_1\pi^+) \leq \Delta^2(p_2\pi^+)$, $M(p_2\pi^+)$ outside the N*(1236) band, and $|\cos\theta(p_1\pi^+)| \geq 0.9$ (908 events).

Fig. 43. Mass distributions of (a) $p_1\pi^o$ and (b) $p_2\pi^+\pi^-$ for those events in the $p_1p_2\pi^+\pi^-\pi^o$ channel selected such that $\Delta^2(p_1\pi^o) \leq \Delta^2(p_2\pi^o)$, $M(p_1\pi^+)$ outside the N*(1236) band, and $|\cos\theta(p_1\pi^o)| \geq 0.9$ (890 events).

Fig. 44. Mass distributions of (a) $p_1\pi^-$ and (b) $p_2\pi^+\pi^o$ for those events in the $p_1p_2\pi^+\pi^-\pi^o$ channel selected such that $\Delta^2(p_1\pi^-) \leq \Delta^2(p_2\pi^-)$, $M(p_1\pi^+)$ outside the N*(1236) band, and $|\cos\theta(p_1\pi^-)| \geq 0.9$ (831 events).

TABLE I. Summary of Events Found

Reaction	Number of Events Found	Corrected** Percentage of Total Number of Events in the Film (25168)
I. Well measured events with good fits		
$pp \rightarrow pp\pi^+\pi^-$	3445	29.3
$np\pi^+\pi^+\pi^-$	3182*	27.0
$pp\pi^+\pi^-\pi^o$	2634	22.4
$d\pi^+\pi^+\pi^-$	50	.4
$d\pi^+\pi^+\pi^-\pi^o$	178	1.5
II. Well measured events with no acceptable fit	2281*	19.4
III. Events which were not successfully measured	5344	
Totals	17114	100.0

* Corrected for Fake Fits.

** Corrected for measurement failure (31.3%) and scan efficiency (68%).

TABLE II. Cross Sections

Reaction	Cross Sections (millibarns)							
	Ref. (12) 2.23 GeV/c	Ref. (13) 2.81 GeV/c	Ref. (14) 3.67 GeV/c	Ref. (15) 4.0 GeV/c	Ref. (16) 5.0 GeV/c	Ref. (17) 5.5 GeV/c	This Exp. 6.0 GeV/c	Ref. (18) 10 GeV/c
$pp \rightarrow pp\pi^+\pi^-$	1.22 ± 0.14	2.51 ± 0.14	2.67 ± 0.13	2.95 ± 0.15	2.96 ± 0.12	2.84 ± 0.08	3.2 ± 0.3	2.45 ± 0.10
$np\pi^+\pi^+\pi^-$	0.02 ± 0.02	0.405 ± 0.40	1.15 ± 0.09		2.19 ± 0.09	2.85 ± 0.08	2.9 ± 0.4	2.27 ± 0.25
$pp\pi^+\pi^-\pi^o$	0.02 ± 0.02	0.217 ± 0.029	0.74 ± 0.07		1.76 ± 0.07	1.84 ± 0.07	2.4 ± 0.2	2.50 ± 0.30
$d\pi^+\pi^+\pi^-$			0.06 ± 0.02		0.02 ± 0.01		0.04 ± 0.01	
$d\pi^+\pi^+\pi^-\pi^o$					$0.08^{+0.01}_{-0.03}$		0.16 ± 0.03	

Table III. Partial Cross Sections for the reaction $pp \rightarrow pp\pi^+\pi^-$

Final State	Percentage of Events[a]	Cross Section (mb)
A. $N^{*++}_{1236}(p\pi^+)N^{*o}_{1236}(p\pi^-)$	20.8 ± 1.1	.66 ± .07
B. $N^{*++}_{1236}(p\pi^+)N^{*o}_{1525}(p\pi^-)$	13.7 ± 1.0	.44 ± .05
C. $N^{*++}_{1236}(p\pi^+)N^{*o}_{1688}(p\pi^-)$	7.7 ± 0.8	.25 ± .04
D. (1) $pN^{*+}_{1400}(p\pi^+\pi^-)$	21.1 ± 2.0	.68 ± .09
(2) $pN^{*+}_{1400}(N^{*\overset{+}{o}+}_{1236}(p\pi^{\pm})\pi^{\mp})$	9.4 ± 1.9	.30 ± .07
E. $pN^{*+}_{1525}(N^{*\overset{+}{o}+}_{1236}(p\pi^{\pm})\pi^{\mp})$	6.1 ± 1.0	.20 ± .04
F. $pN^{*+}_{1688}(N^{*\overset{+}{o}+}_{1236}(p\pi^{\pm})\pi^{\mp})$	13.2 ± 0.9	.42 ± .05
G. $pN^{*+}_{1920}(p\pi^+\pi^-)$	5.9 ± 1.1	.19 ± .04
H. $pp\pi^+\pi^-$	2.1 ± 3.7	.07 ± .12

(a) The curves shown on Figs. 6, 7, 8 and 9 were calculated assuming this mixture of final states.

Table IV. Rho Meson Production

Final State	Cross Section (μb)	Case I $N(N^*\rho)_{I=1/2}$	Case II $N(N^*\rho)_{I=3/2}$	Case III $N^*(N\rho)_{I=1/2}$	Case IV $N^*(N\rho)_{I=3/2}$
$pN^{*++}(p\pi^+)\rho^-(\pi^-\pi^0)$	153 ± 31	9	18	18	3
$pN^{*+}(p\pi^0)\rho^0(\pi^+\pi^-)$	45 ± 12	4	2	2	8
$pN^{*0}(p\pi^-)\rho^+(\pi^+\pi^0)$	65 ± 18	1	8	-	3
$nN^{*++}(p\pi^+)\rho^0(\pi^+\pi^-)$	228 ± 46	-	81	9	6
$pN^{*+}(n\pi^+)\rho^0(\pi^+\pi^-)$	not seen	2	1	1	4

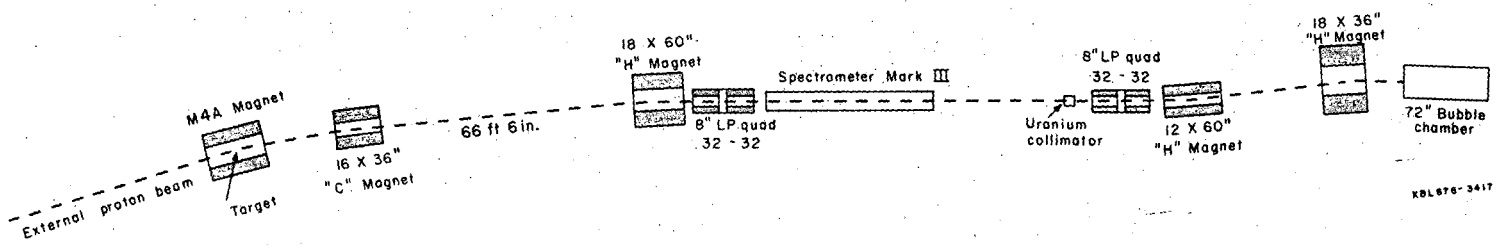
External proton beam
M4A Magnet
Target
16 X 36"
"C" Magnet
66 ft 6 in.
18 X 60"
"H" Magnet
8" LP quad
32 - 32
Spectrometer Mark III
Uranium
collimator
8" LP quad
32 - 32
12 X 60"
"H" Magnet
18 X 36"
"H" Magnet
72" Bubble
chamber
XBL676-3417

Fig. 1

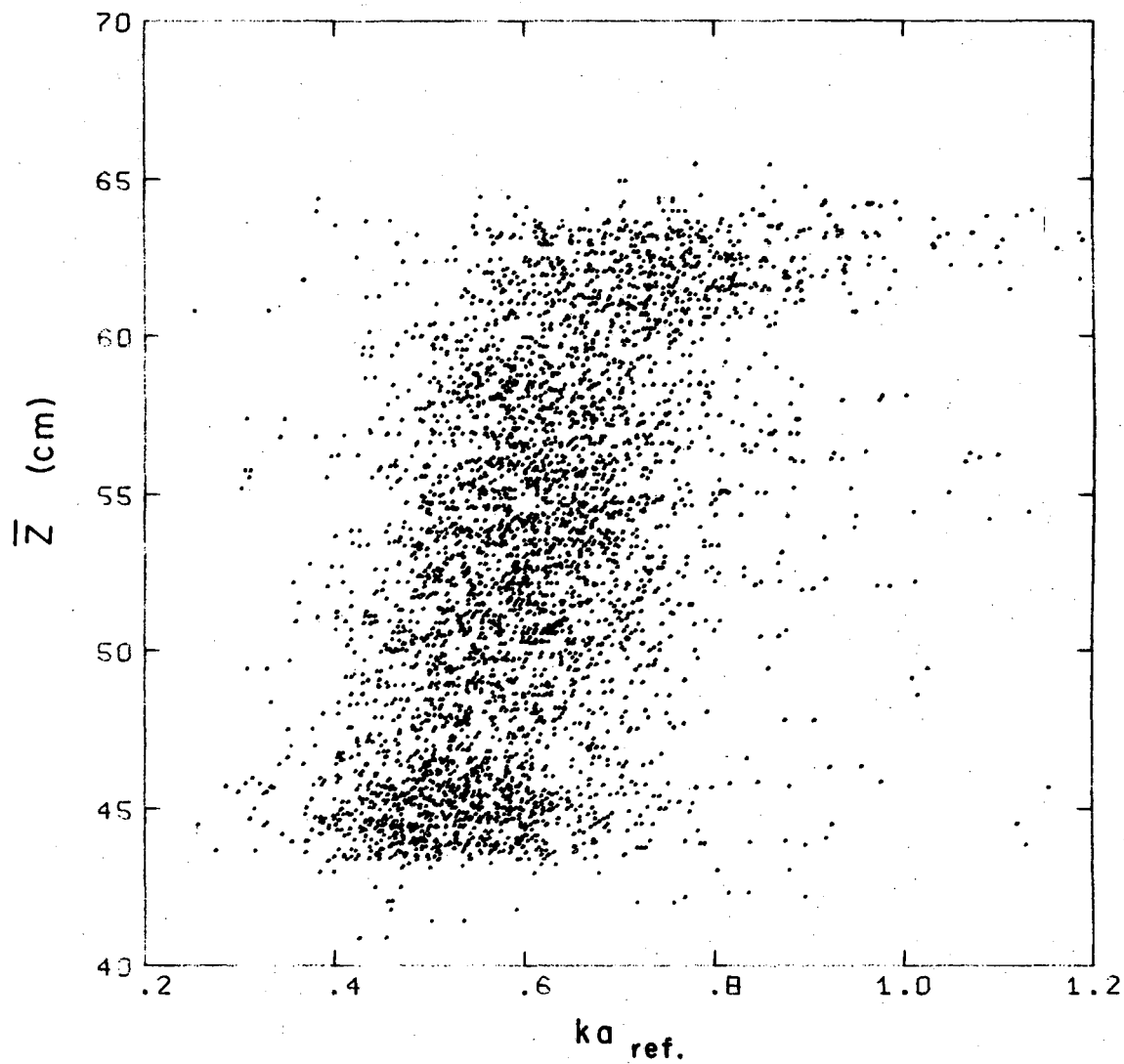

XBL 686-985

Fig. 2

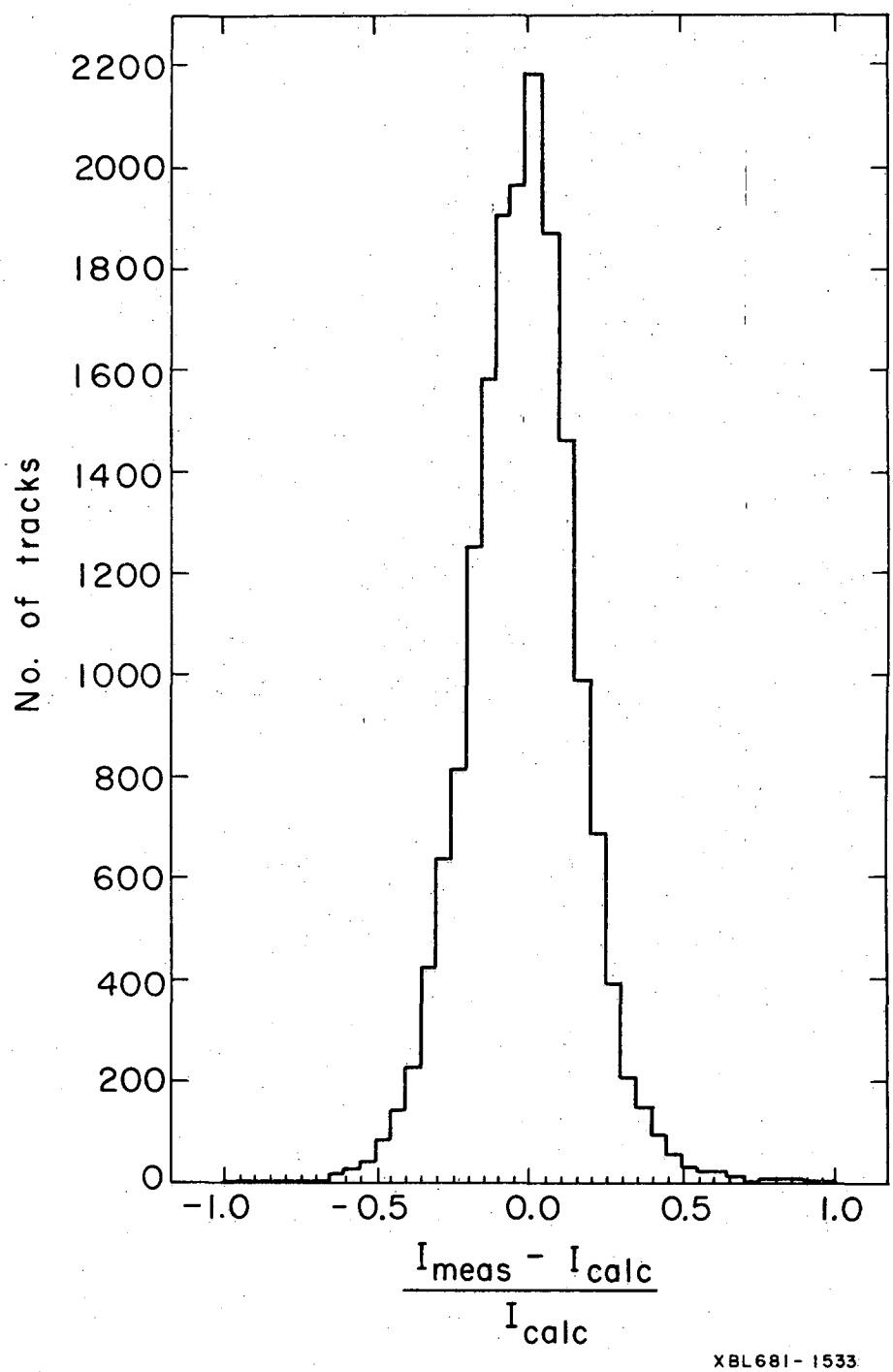
2200
2000
1800
1600
1400
1200
1000
800
600
400
200
0
No. of tracks
-1.0
-0.5
0.0
0.5
1.0
$\frac{I_{meas} - I_{calc}}{I_{calc}}$
XBL681-1533

Fig. 3a

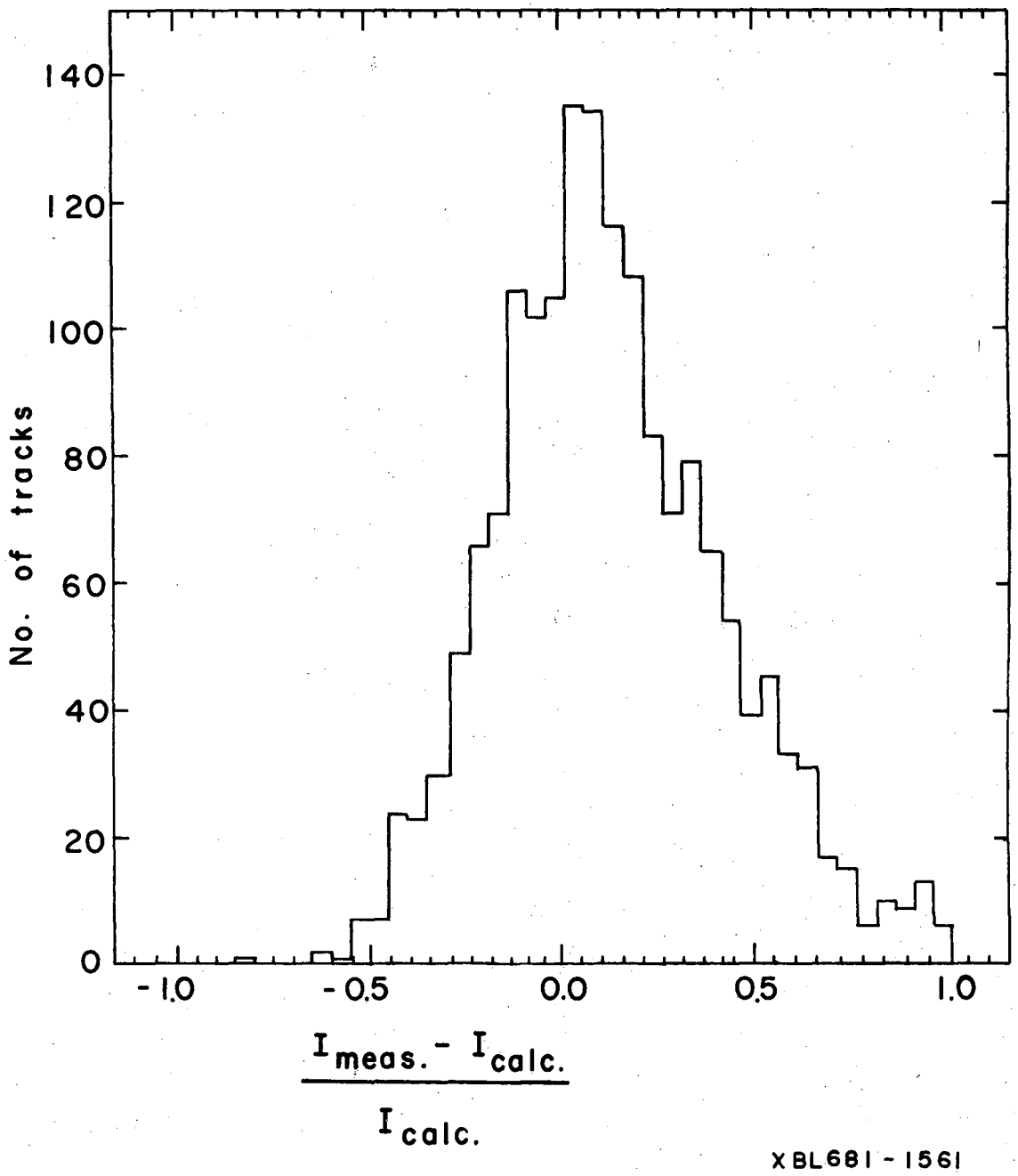
140
120
100
80
60
40
20
0
No. of tracks
-1.0
-0.5
0.0
0.5
1.0
$\frac{I_{meas.} - I_{calc.}}{I_{calc.}}$
XBL681-1561

Fig. 3b

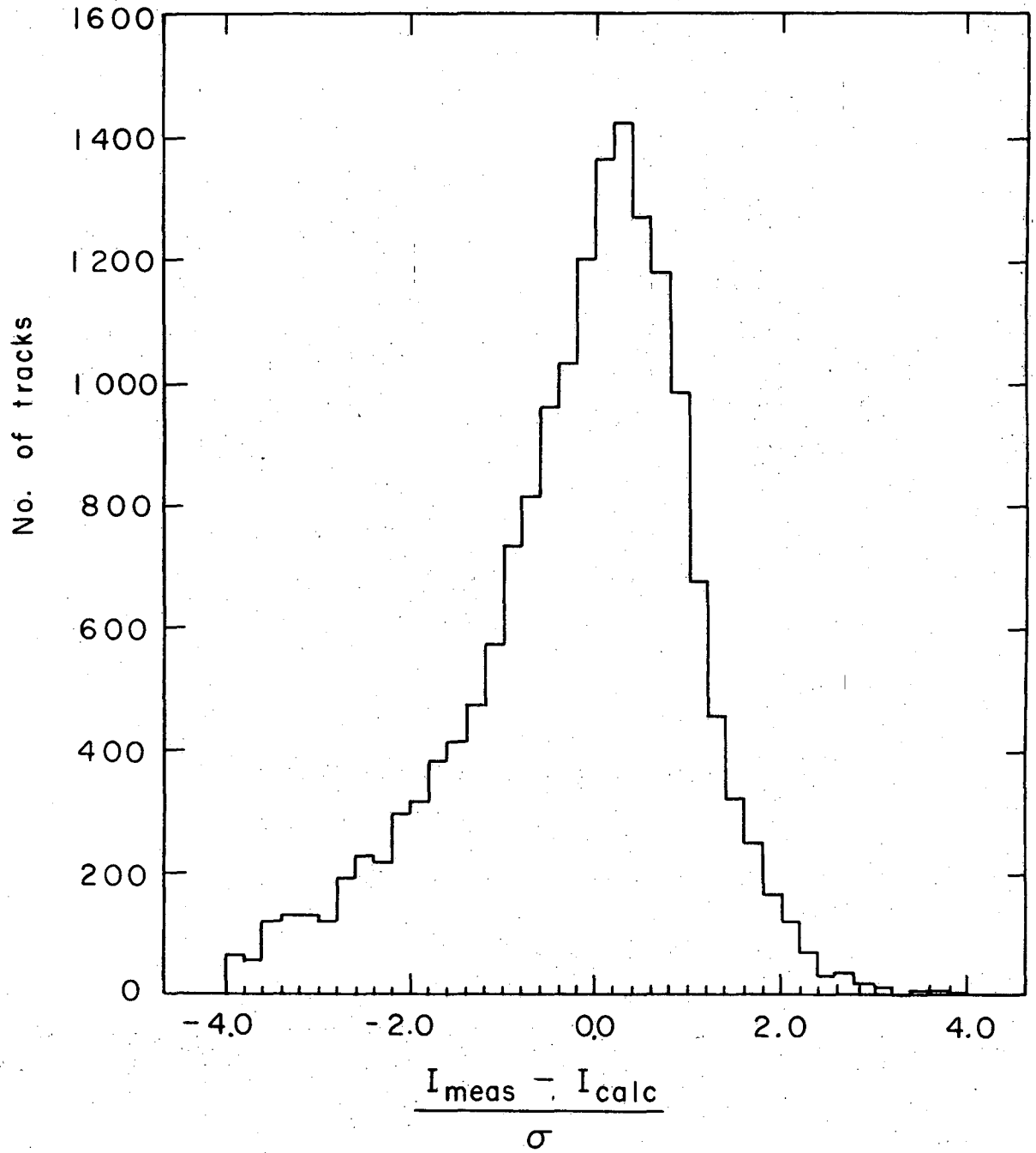

XBL681-1562

Fig. 4a

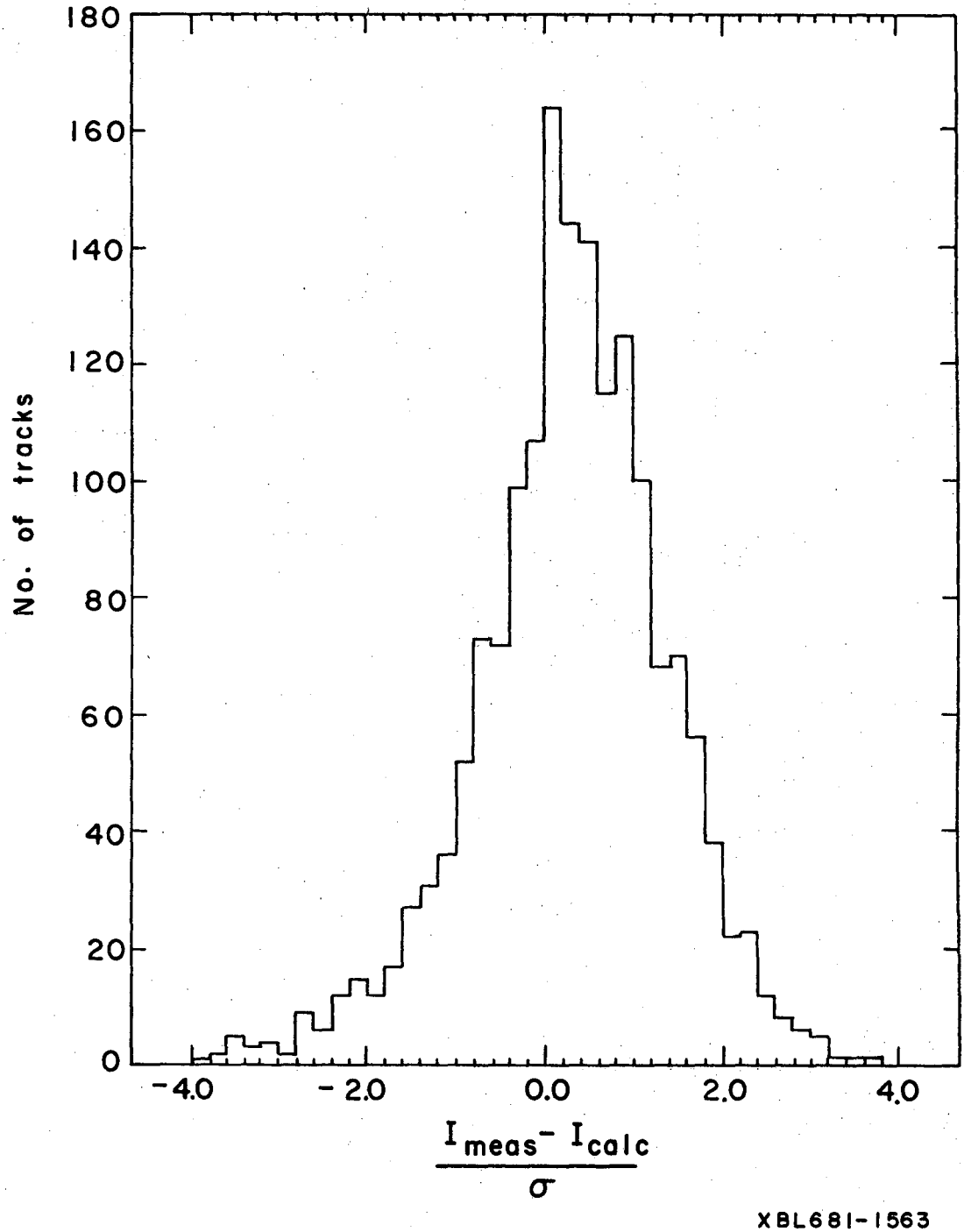
180
160
140
120
100
80
60
40
20
0
No. of tracks
-4.0
-2.0
0.0
2.0
4.0
$\frac{I_{meas} - I_{calc}}{\sigma}$
XBL681-1563

Fig. 4b

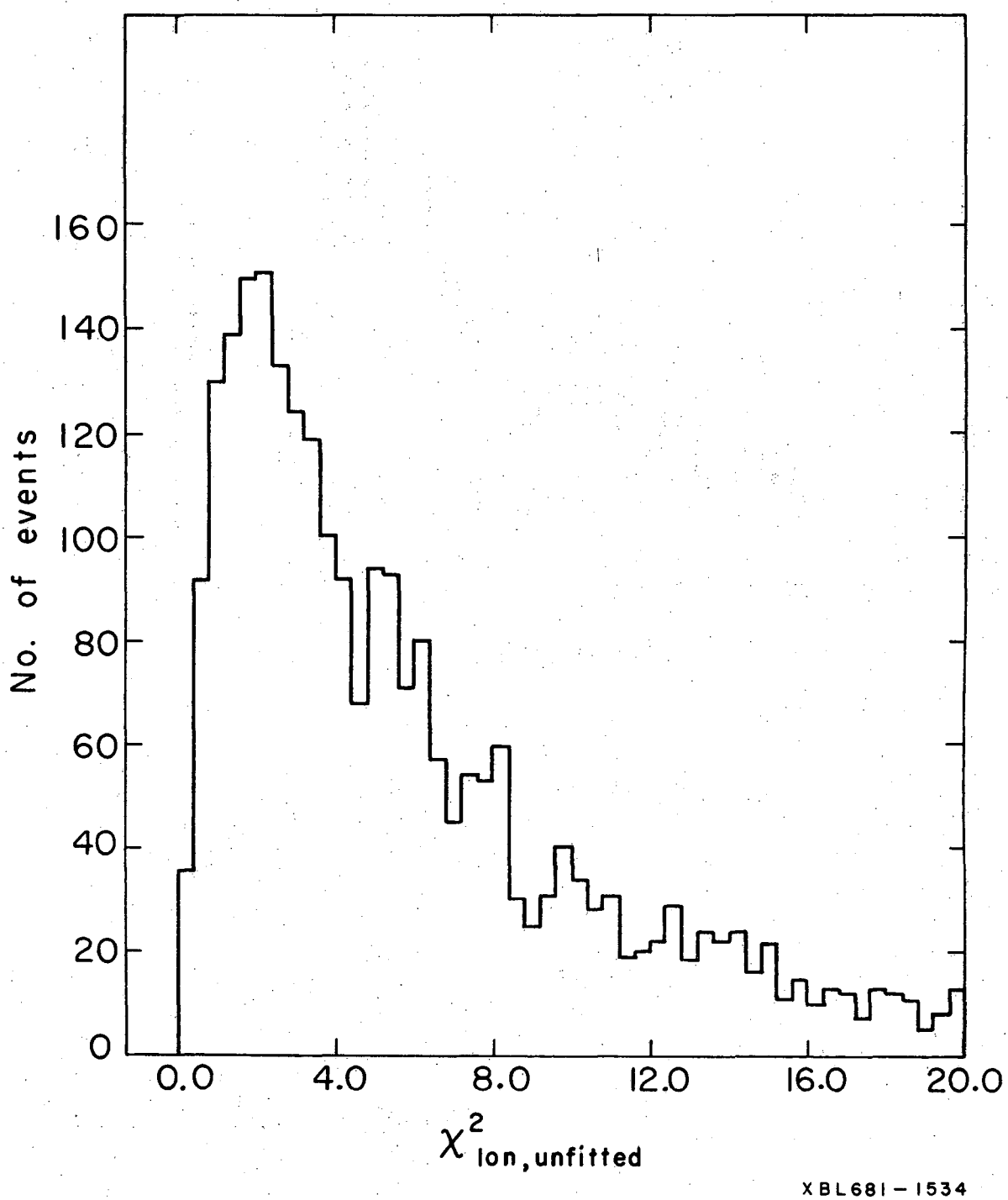
160
140
120
100
80
60
40
20
0
No. of events
0.0
4.0
8.0
12.0
16.0
20.0
$\chi^2_{\text{ion, unfitted}}$
XBL681-1534

Fig. 5a

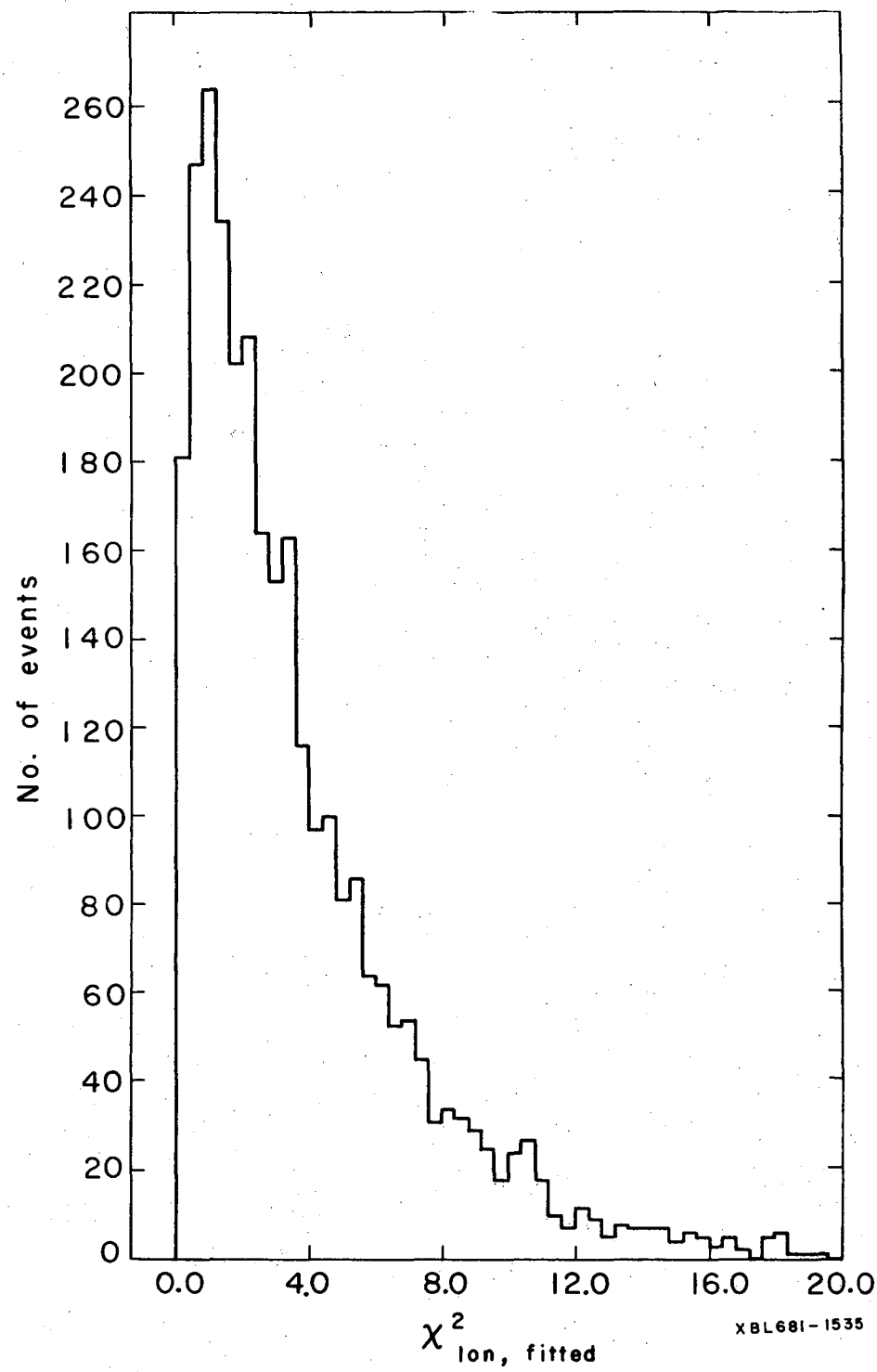
No. of events
0
20
40
60
80
100
120
140
160
180
200
220
240
260
0.0
4.0
8.0
12.0
16.0
20.0
$\chi^2_{\text{lon, fitted}}$
XBL681-1535

Fig. 5b

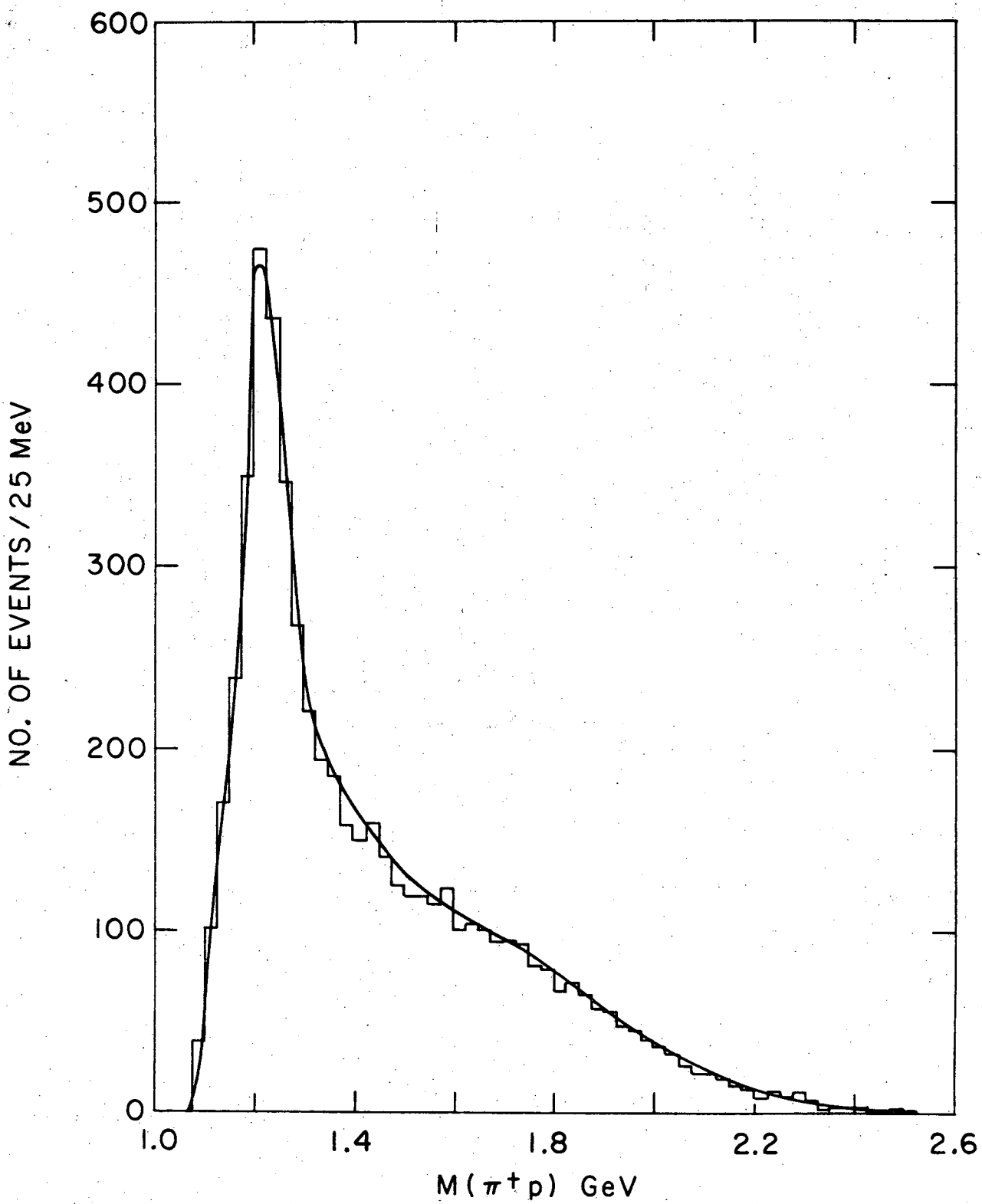
600
500
400
300
200
100
0
NO. OF EVENTS / 25 MeV
1.0
1.4
1.8
2.2
2.6
M(π⁺p) GeV

Fig. 6

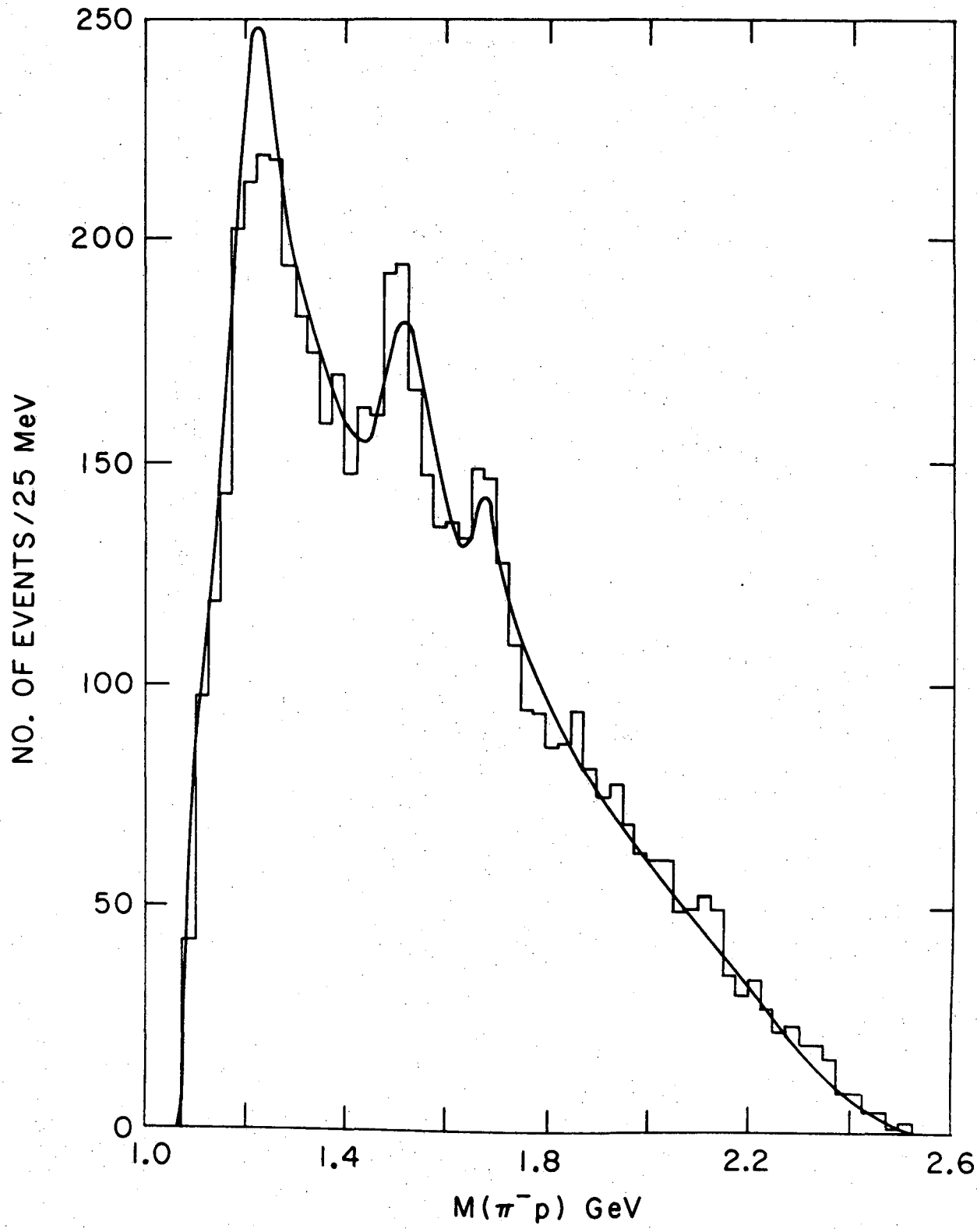

Fig. 7

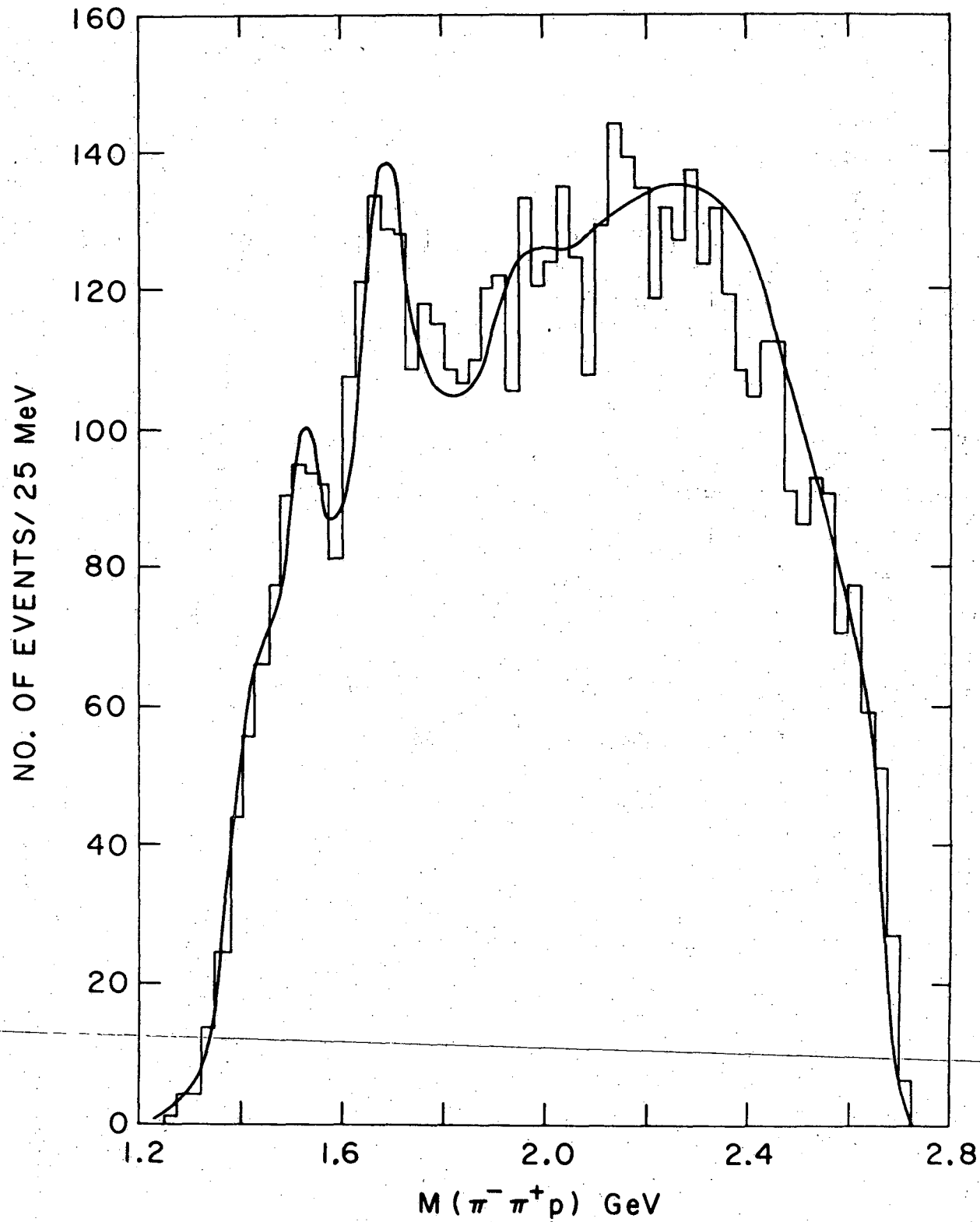
160
140
120
100
80
60
40
20
0
NO. OF EVENTS/ 25 MeV
1.2
1.6
2.0
2.4
2.8
M ($\pi^-\pi^+$p) GeV

Fig. 8

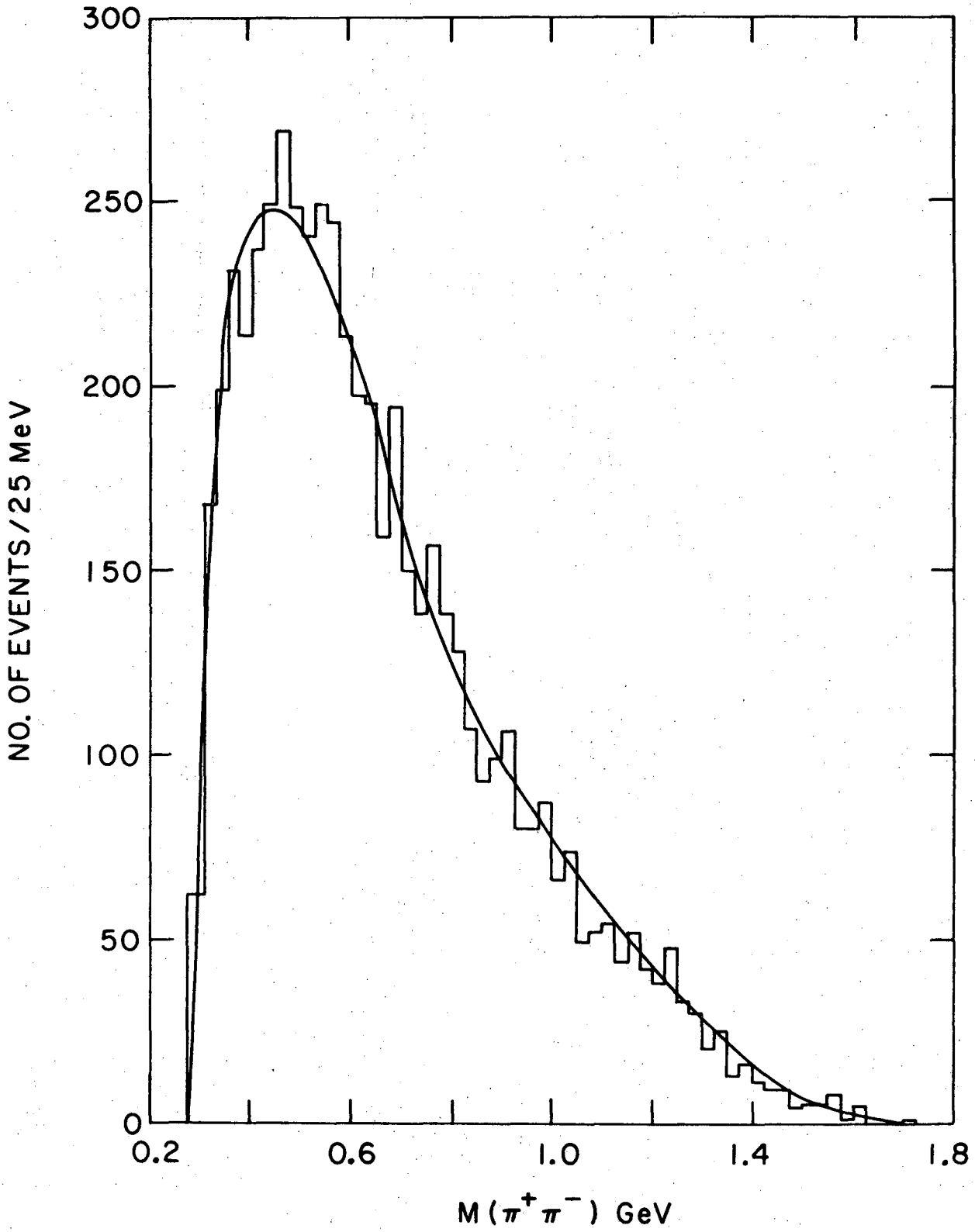
300
250
200
150
100
50
0
NO. OF EVENTS/25 MeV
0.2
0.6
1.0
1.4
1.8
M ($\pi^+\pi^-$) GeV

Fig. 9

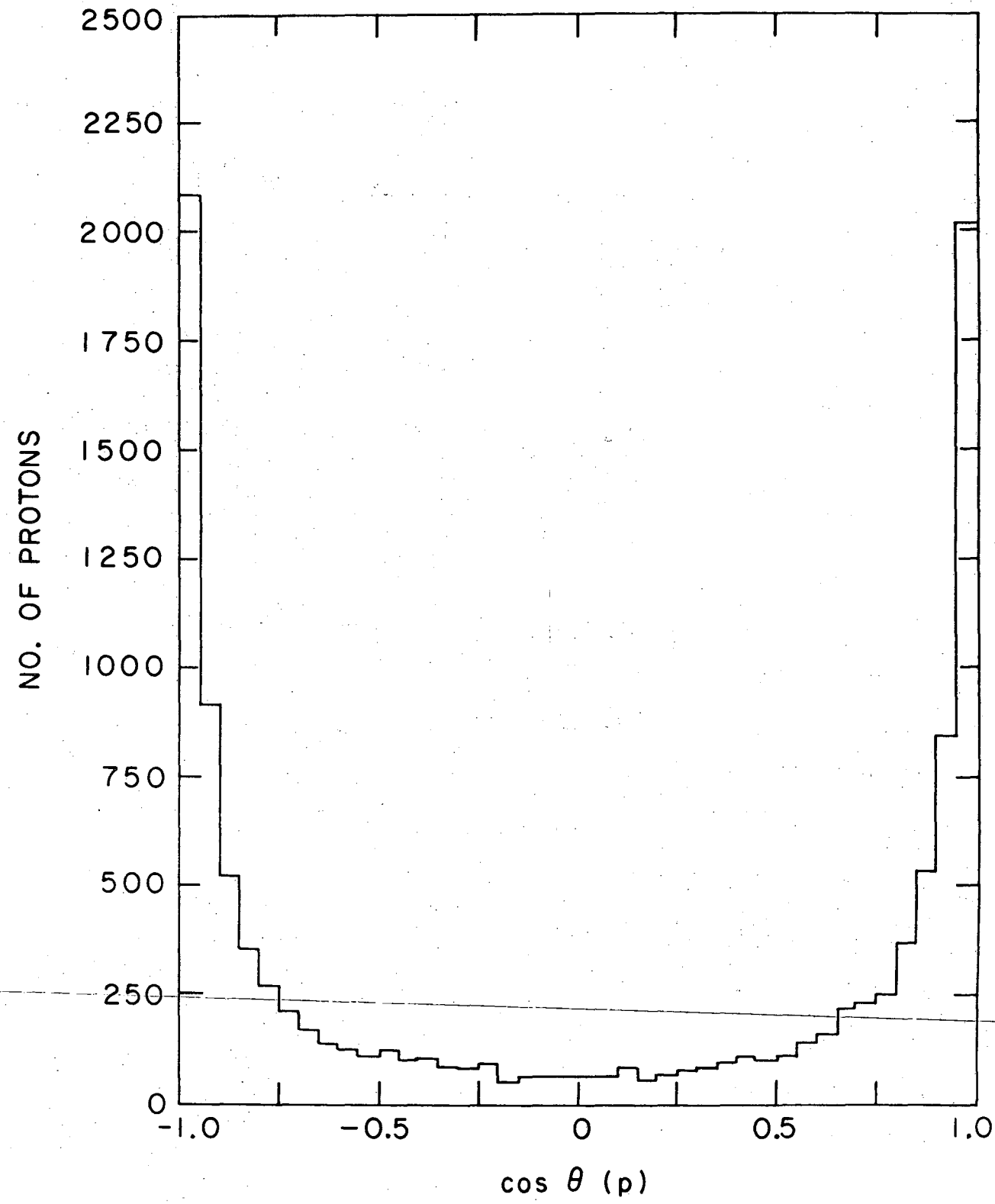
2500
2250
2000
1750
1500
1250
1000
750
500
250
0
NO. OF PROTONS
-1.0
-0.5
0
0.5
1.0
cos θ (p)

Fig. 10

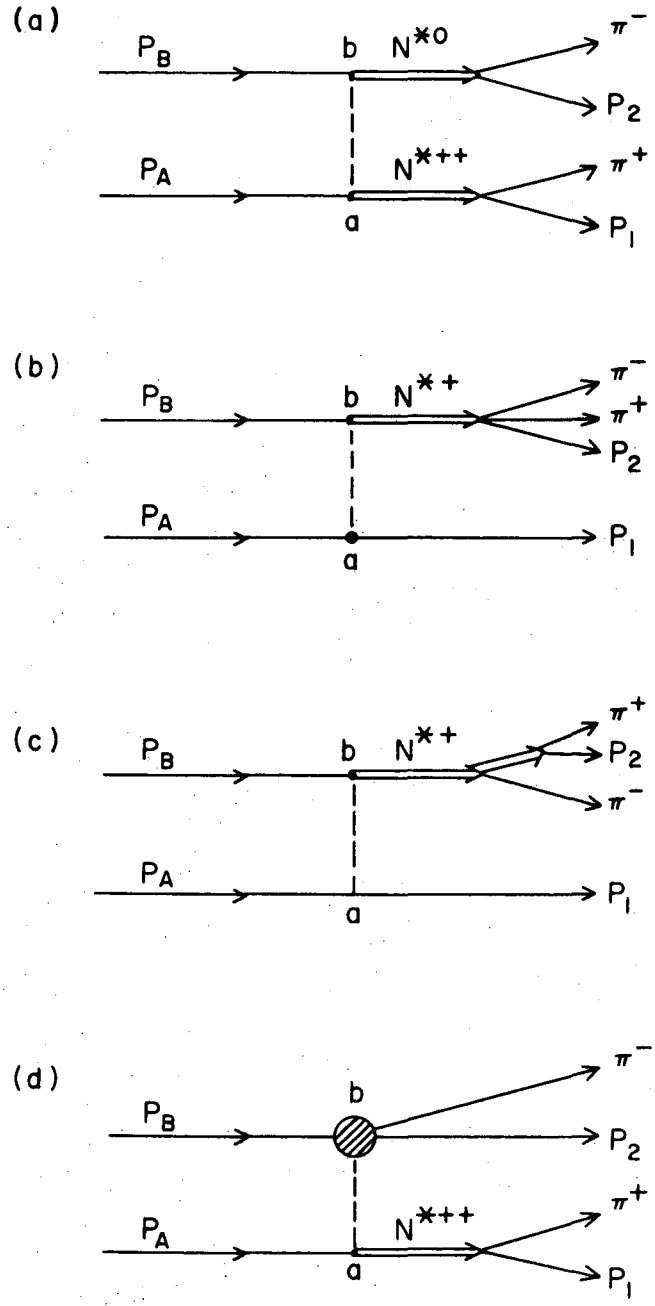

XBL 686-1011

Fig. 11

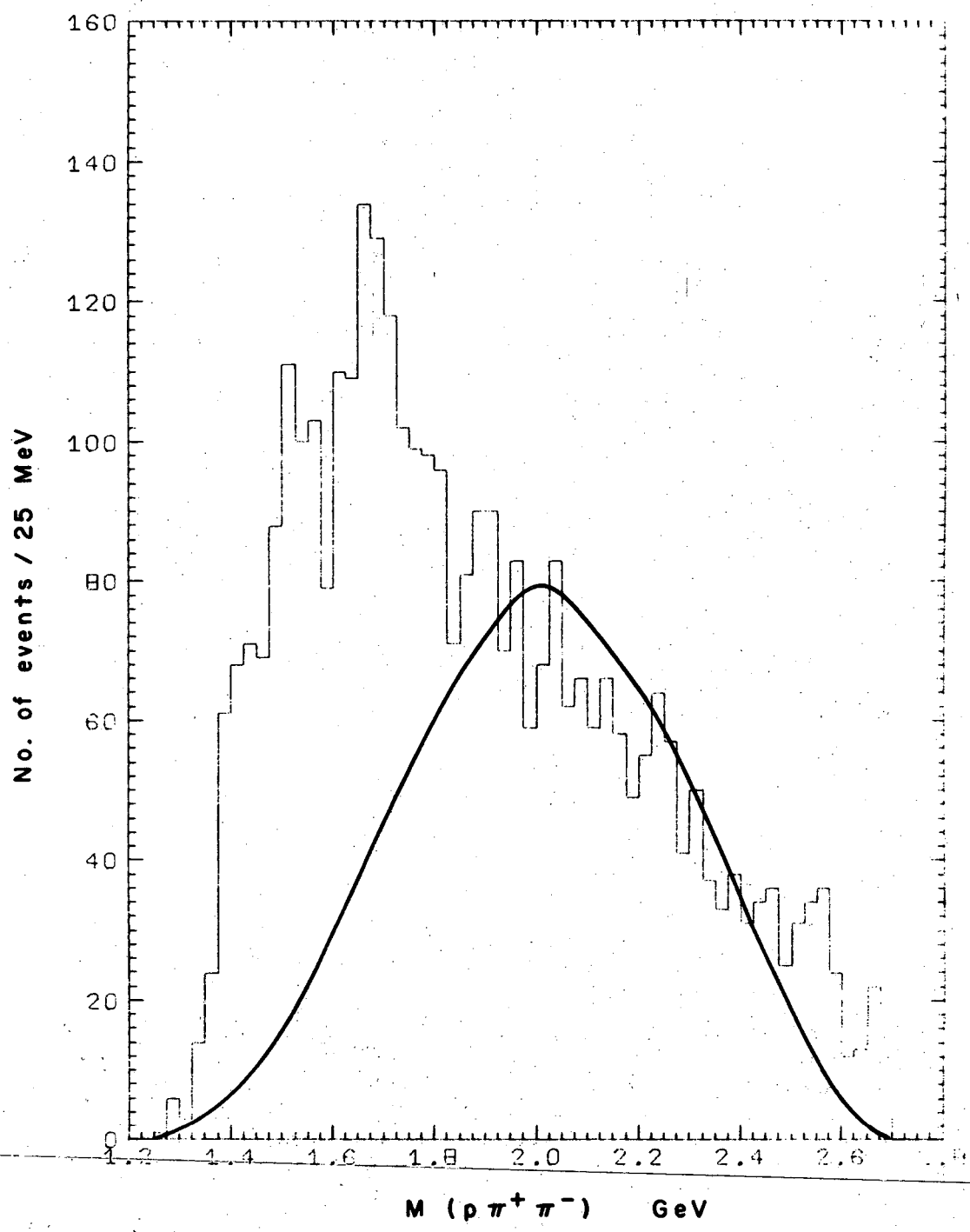

XBL6712-5935

Fig. 12

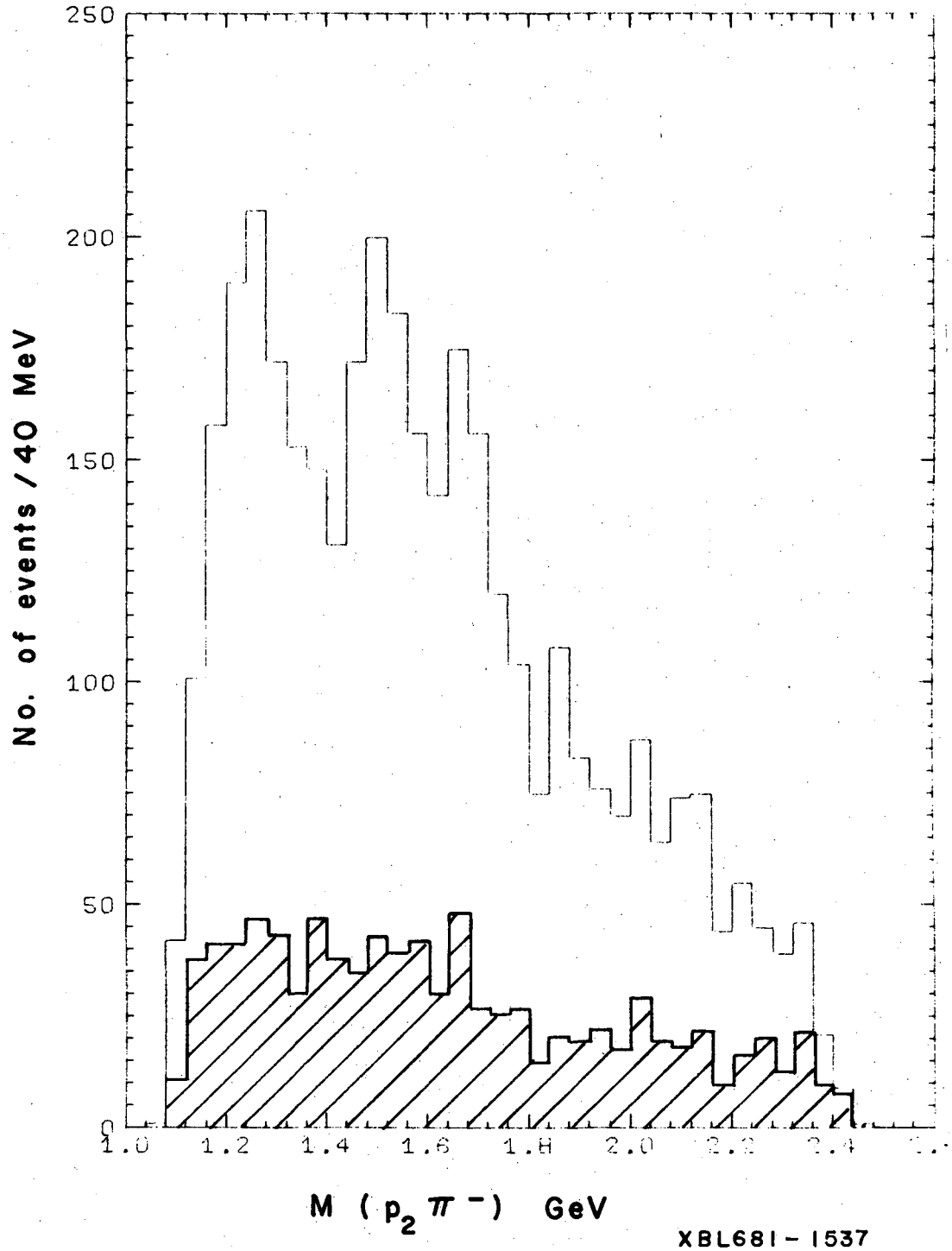
250
200
150
100
50
0
No. of events / 40 MeV
1.0
1.2
1.4
1.6
1.8
2.0
2.2
2.4
M (p2 π −) GeV
XBL681-1537

Fig. 13

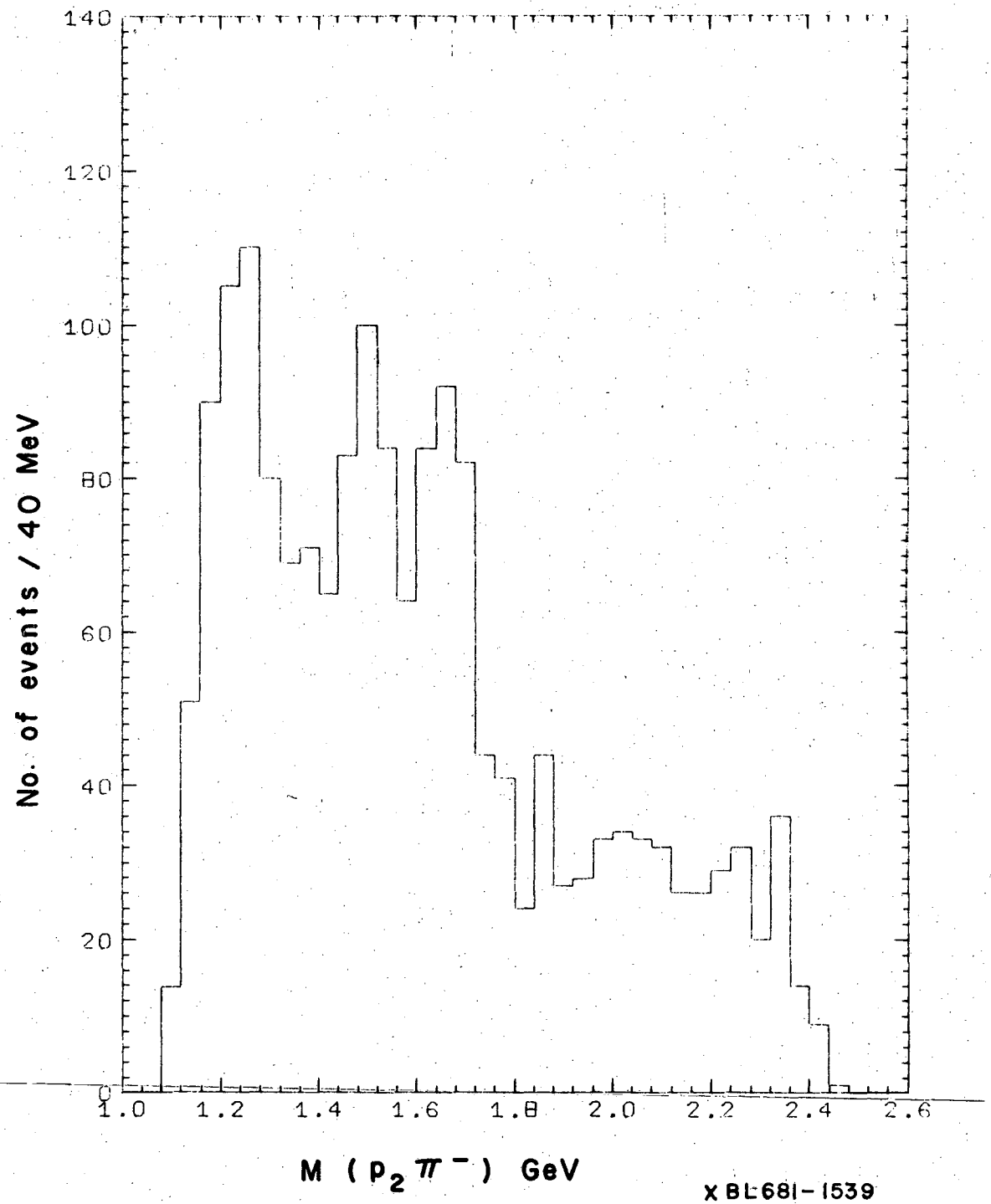
140
120
100
80
60
40
20
0
No. of events / 40 MeV
1.0
1.2
1.4
1.6
1.8
2.0
2.2
2.4
2.6
M (p2 π−) GeV
XBL681-1539

Fig. 14

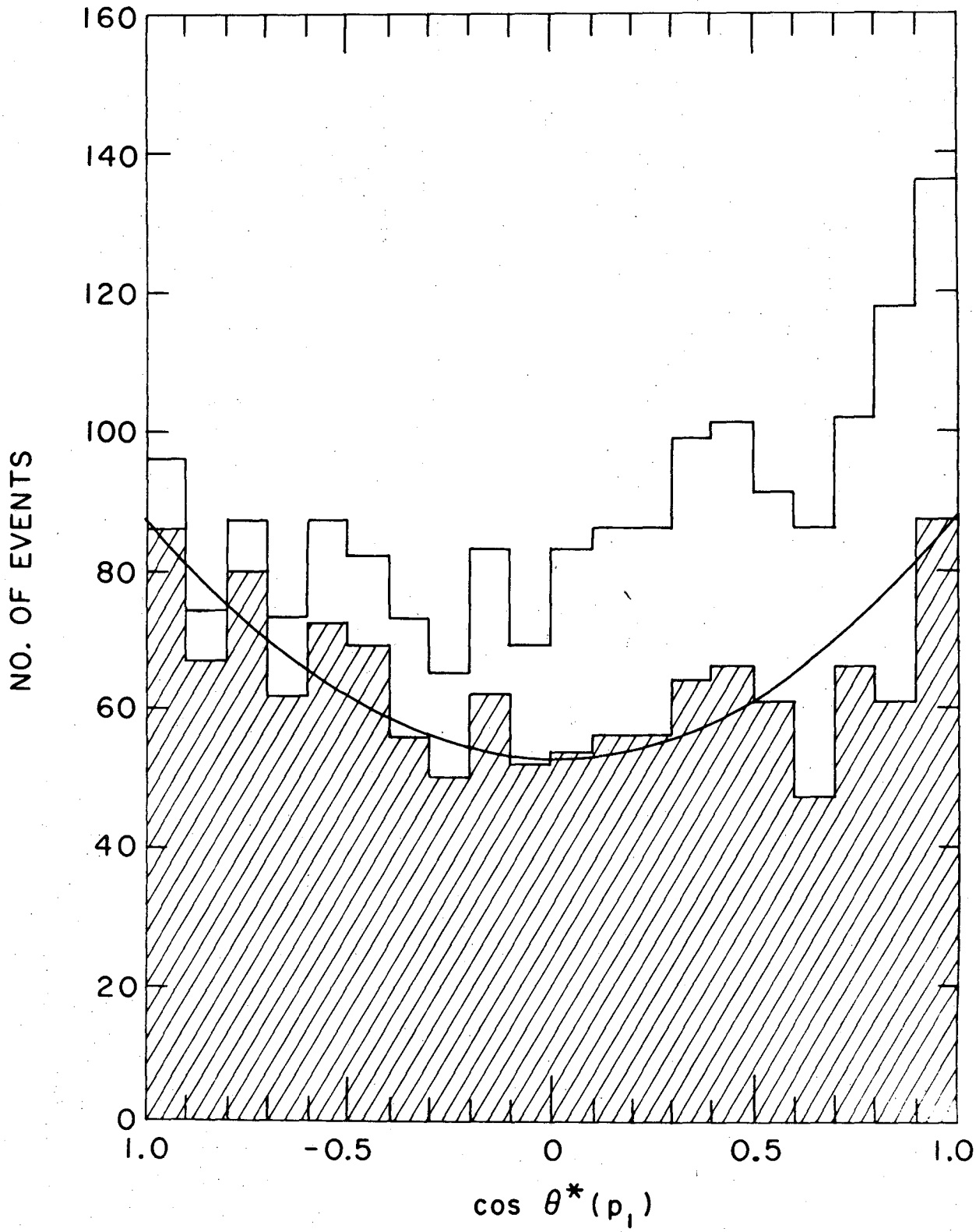

Fig. 15

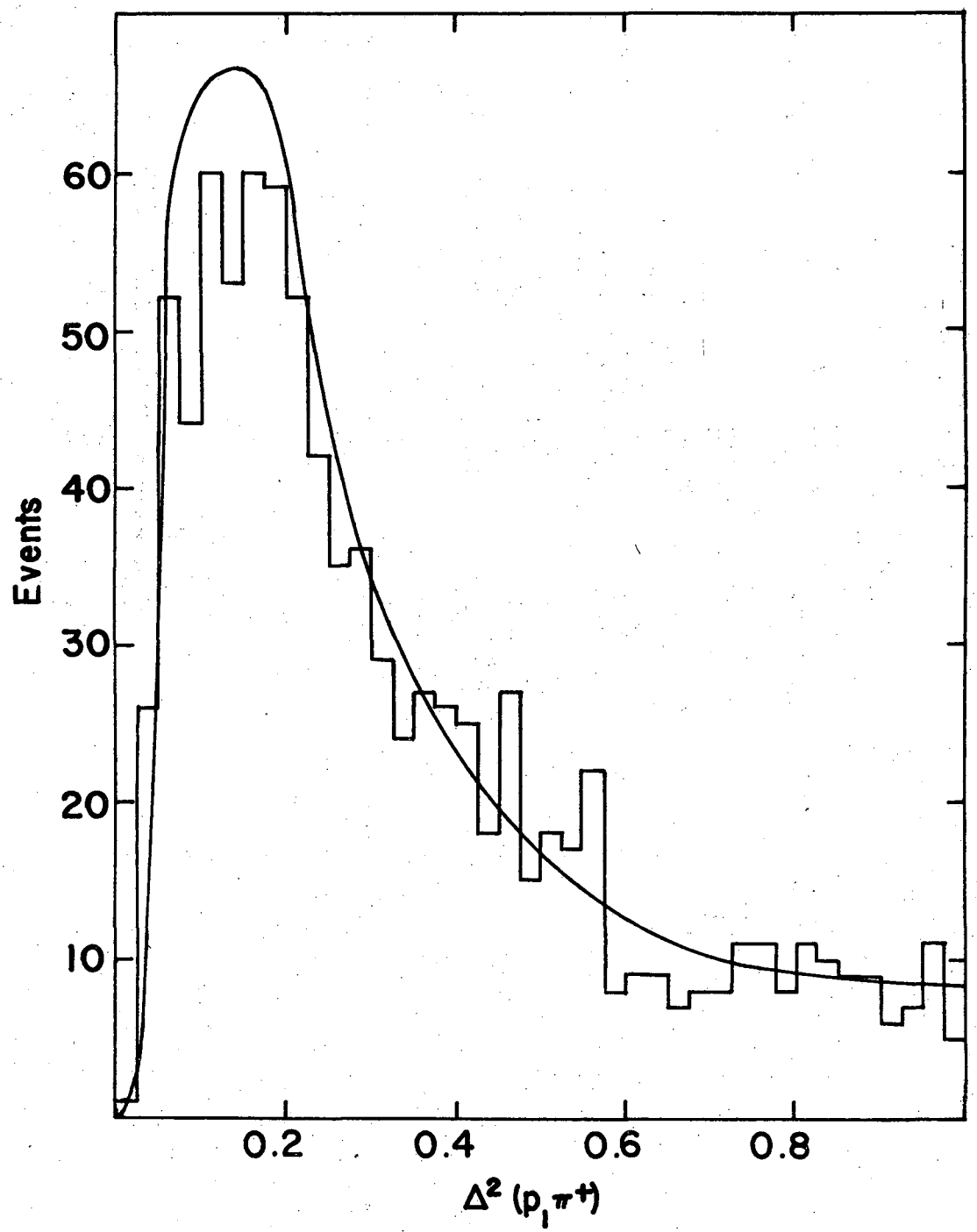

XBL 686-983

Fig. 16

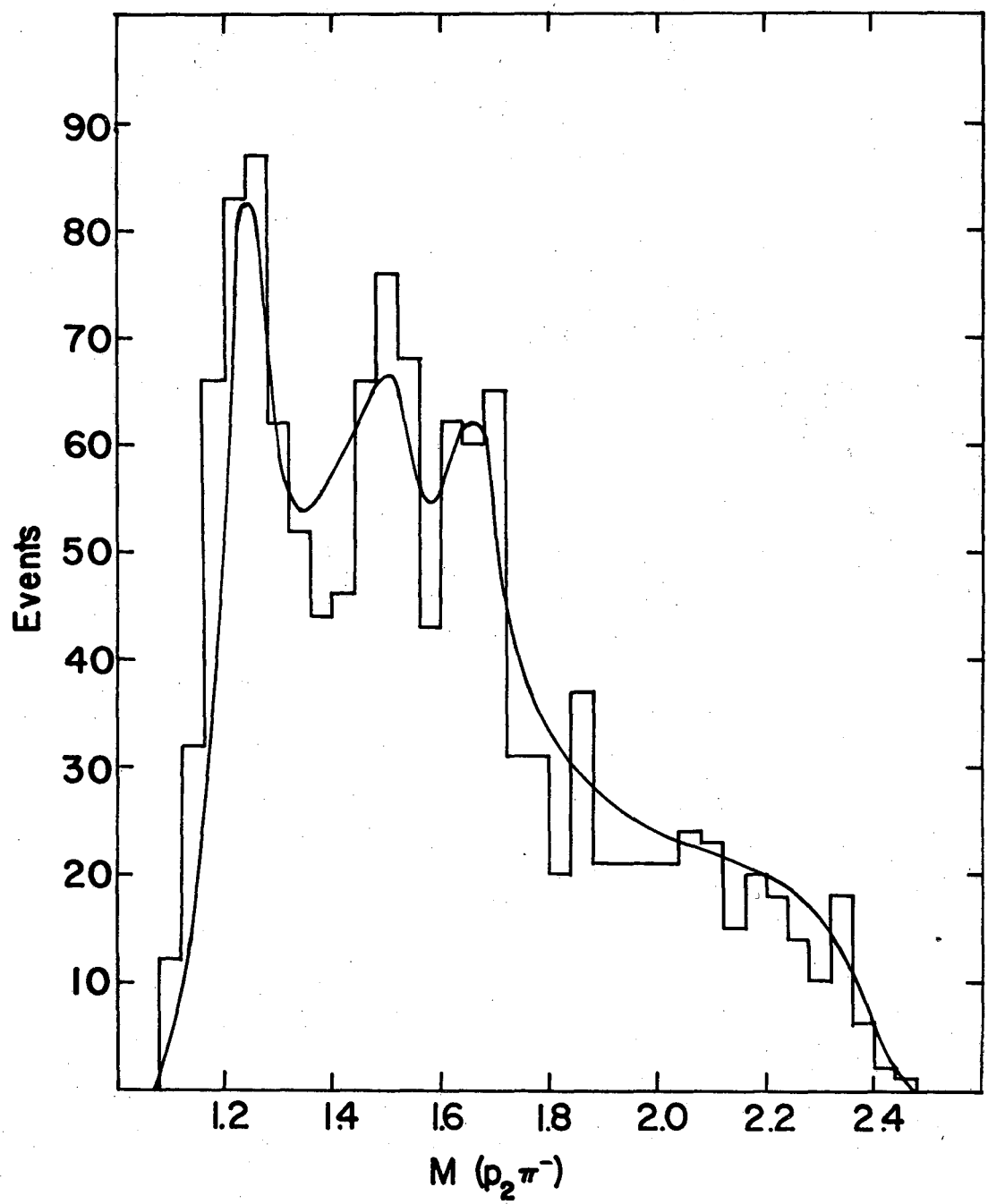

XBL 686-984

Fig. 17

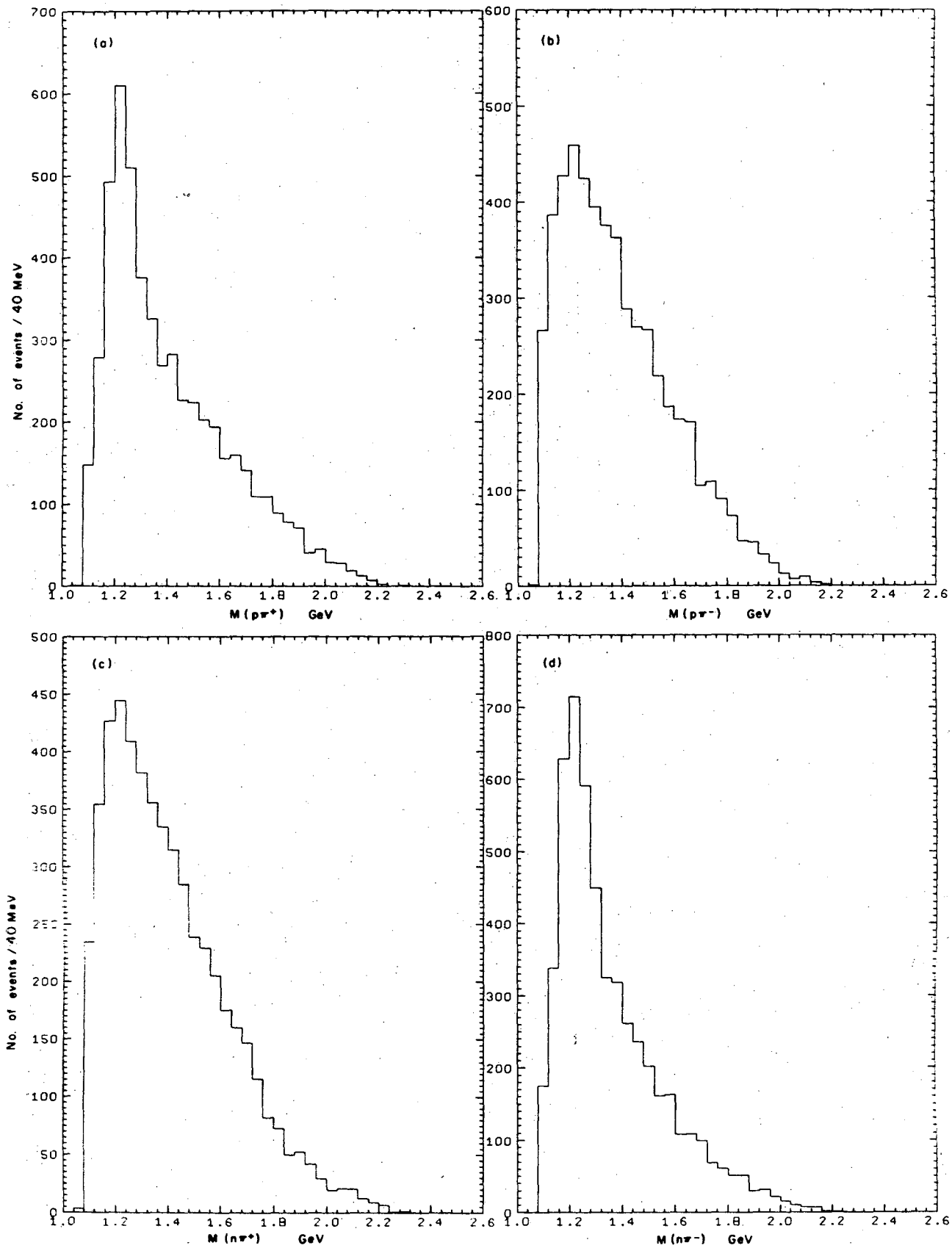

Fig. 18

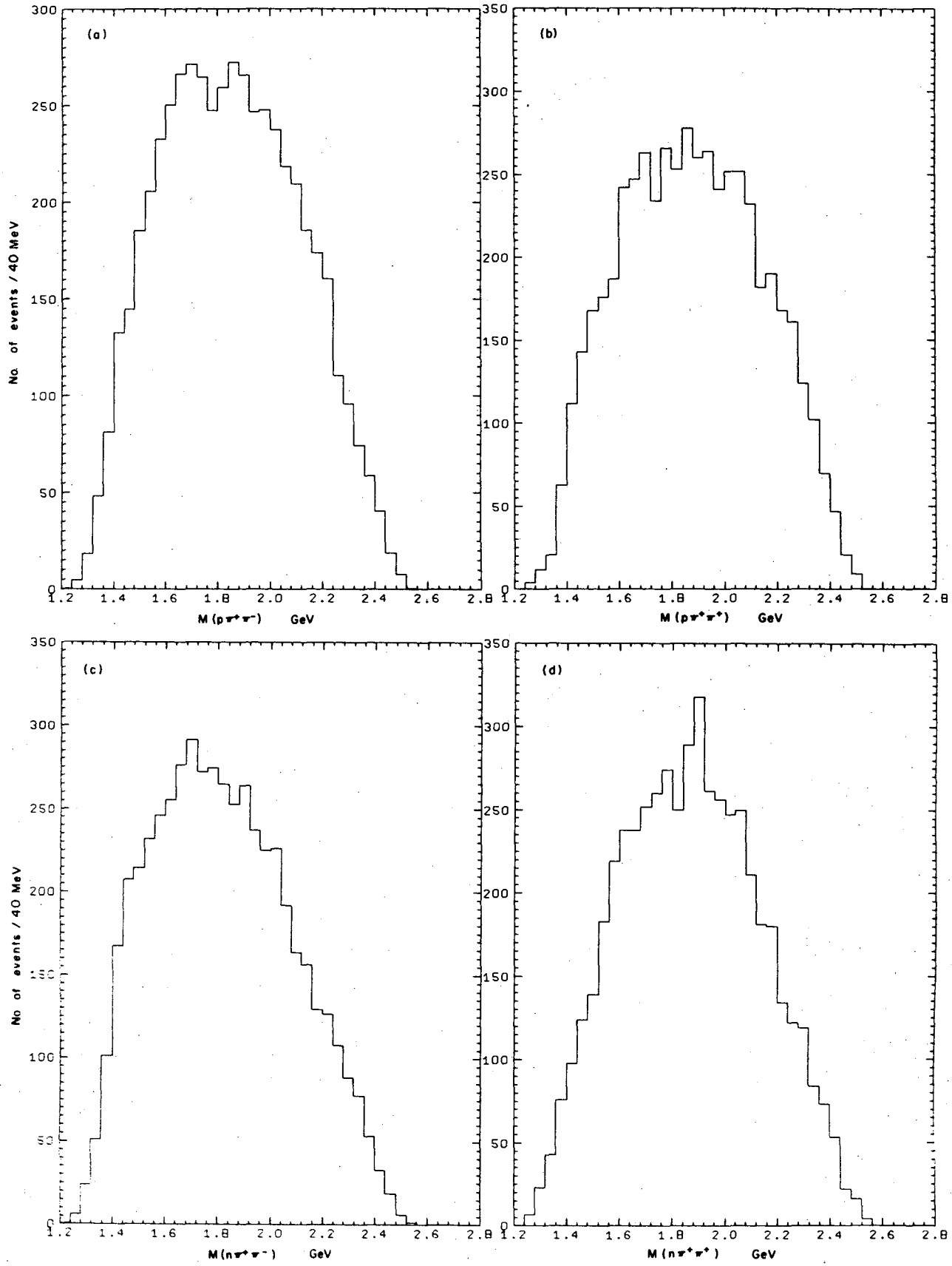

Fig. 19

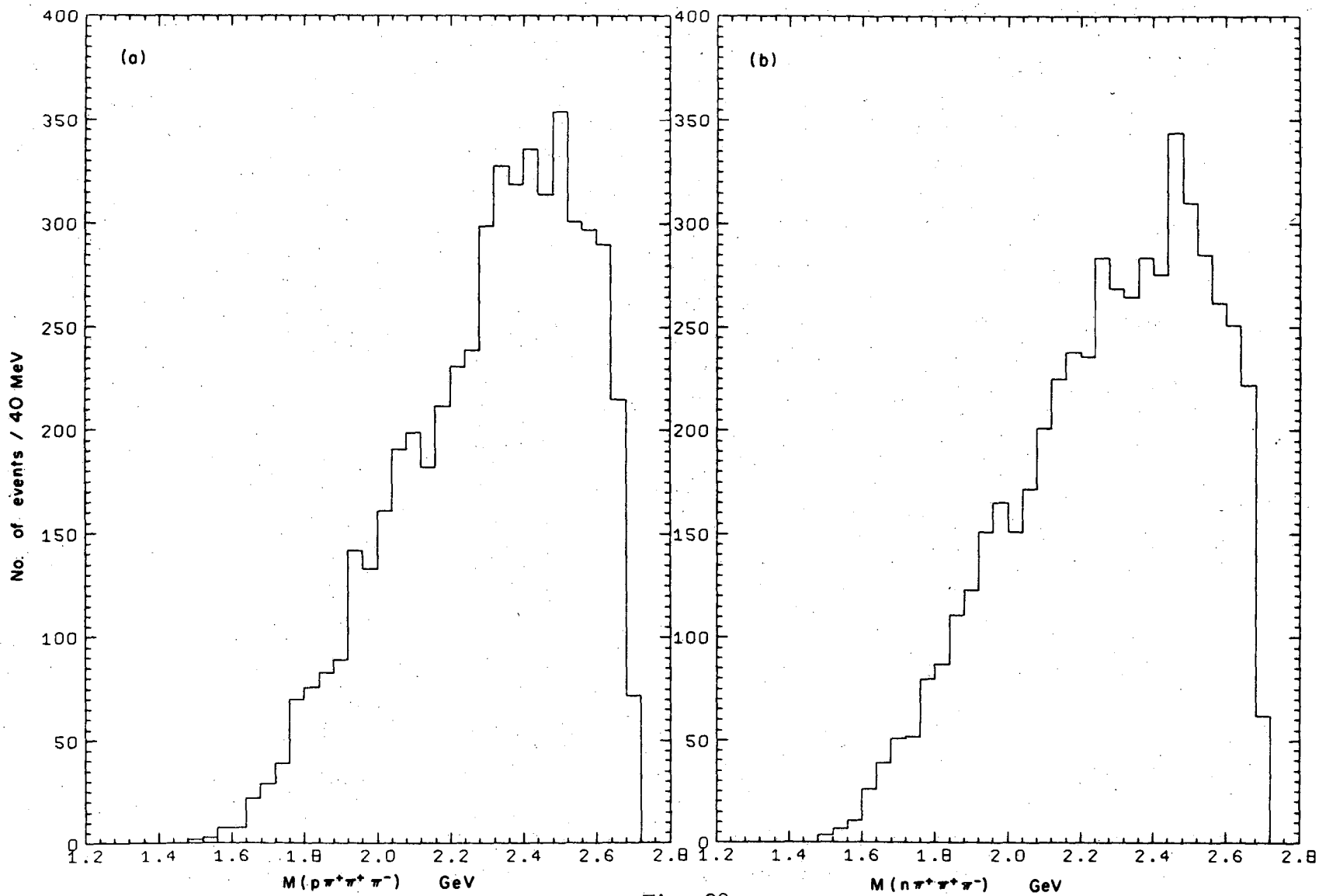
(a)
(b)
No. of events / 40 MeV
0
50
100
150
200
250
300
350
400
1.2
1.4
1.6
1.8
2.0
2.2
2.4
2.6
2.8
M(pπ⁺π⁺π⁻) GeV
M(nπ⁺π⁺π⁻) GeV

Fig. 20

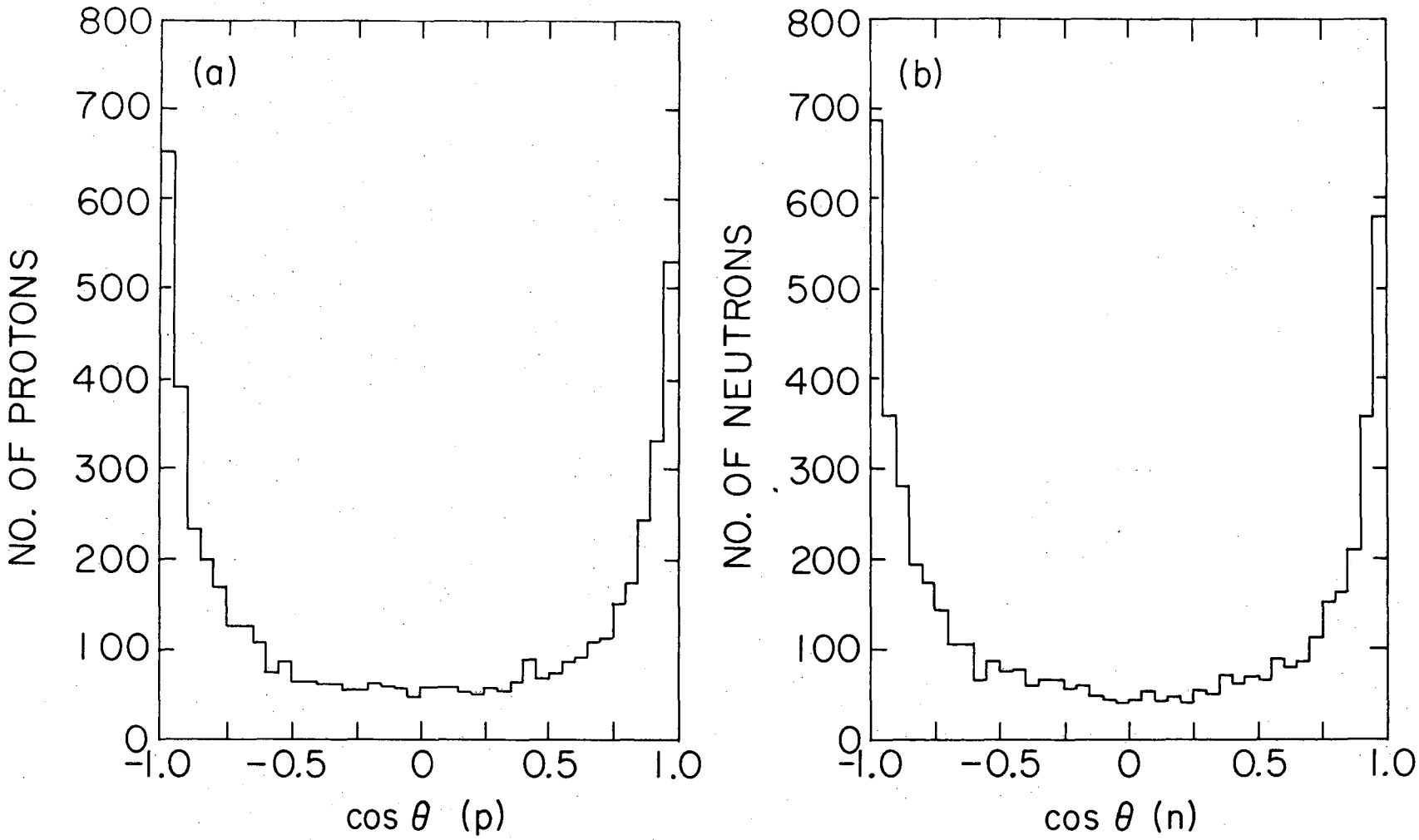
(a)
NO. OF PROTONS
800
700
600
500
400
300
200
100
0
-1.0
-0.5
0
0.5
1.0
cos θ (p)
(b)
NO. OF NEUTRONS
800
700
600
500
400
300
200
100
0
-1.0
-0.5
0
0.5
1.0
cos θ (n)

Fig. 21

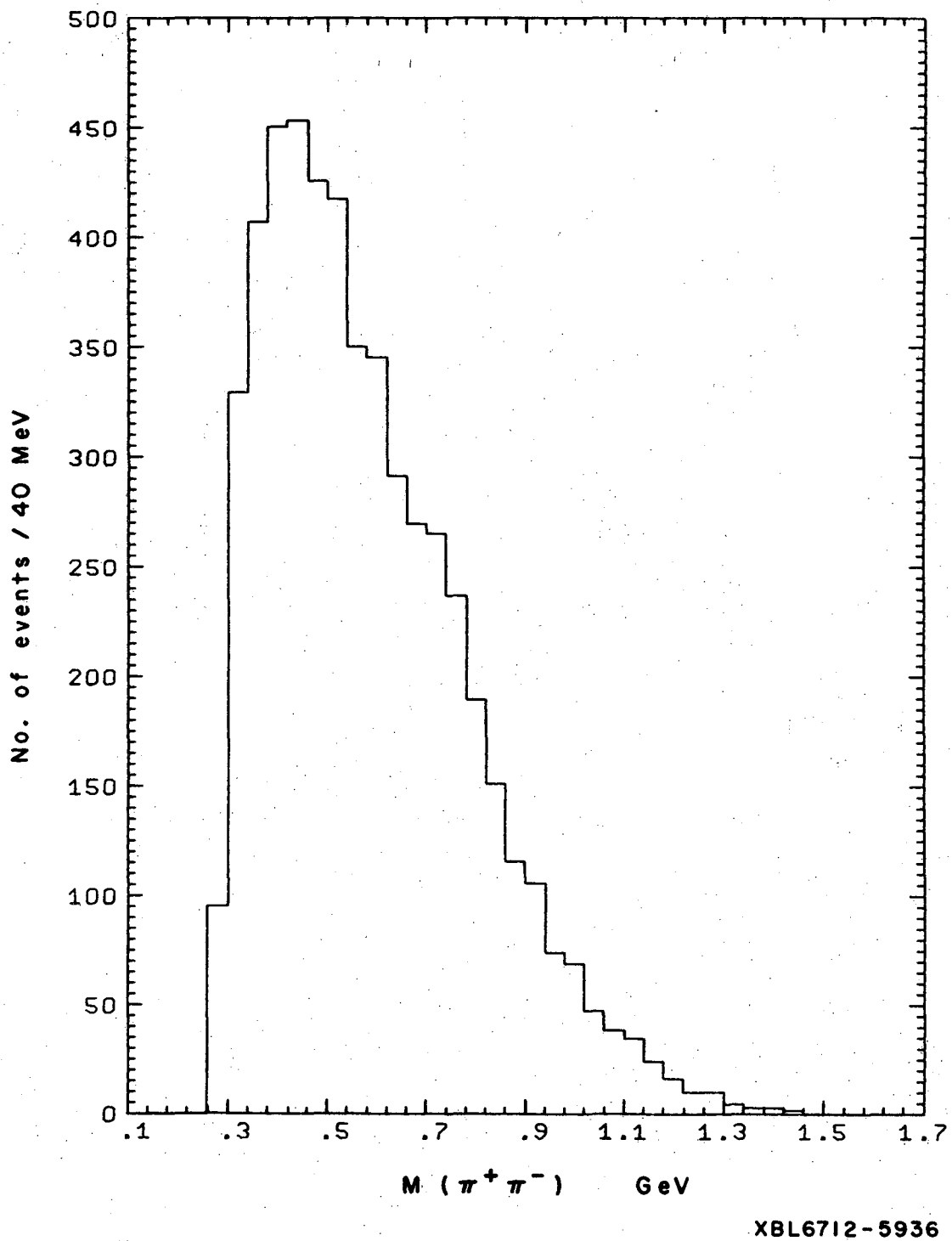
500
450
400
350
300
250
200
150
100
50
0
No. of events / 40 MeV
.1
.3
.5
.7
.9
1.1
1.3
1.5
1.7
M ($\pi^+\pi^-$) GeV
XBL6712-5936

Fig. 22

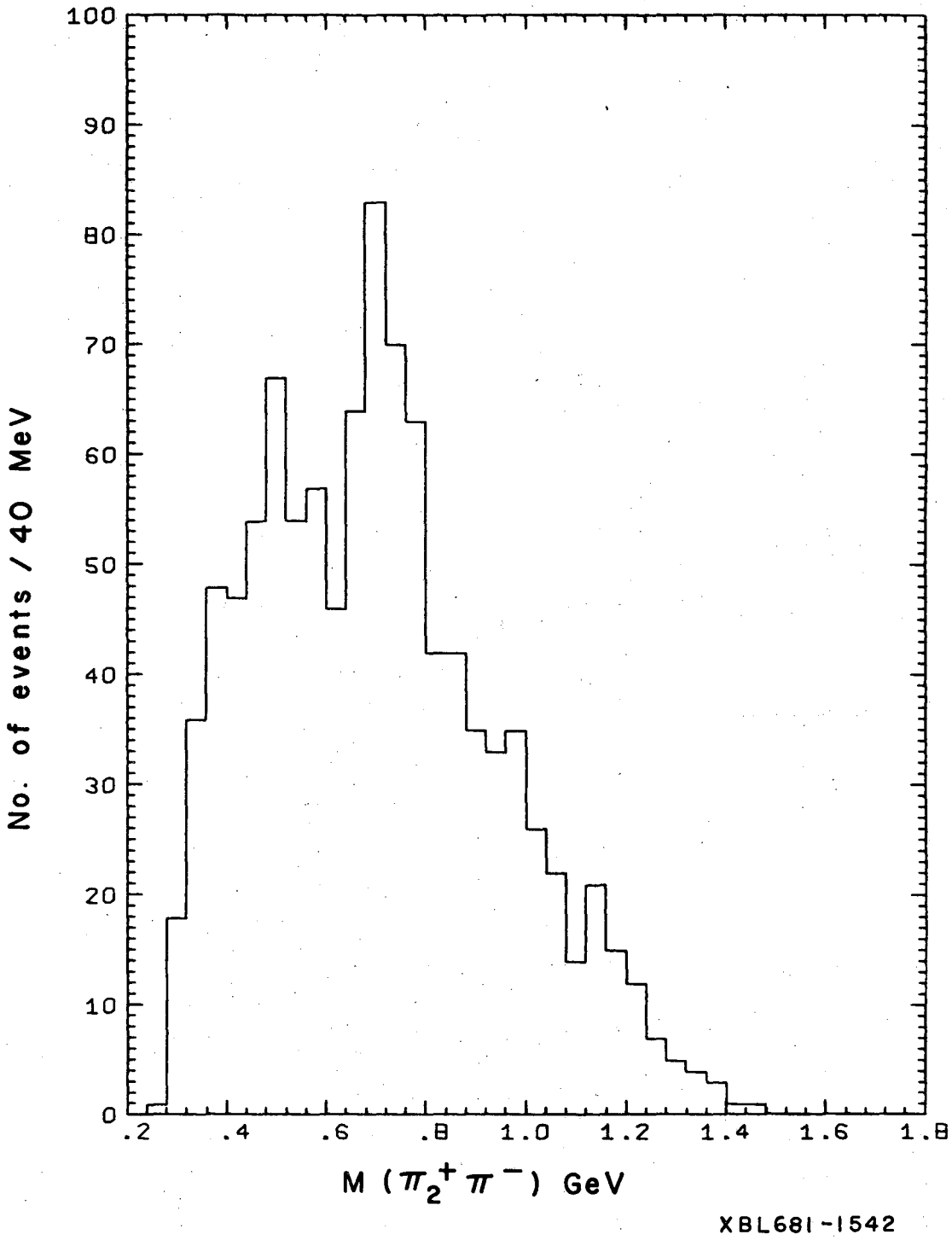
100
90
80
70
60
50
40
30
20
10
0
No. of events / 40 MeV
.2
.4
.6
.8
1.0
1.2
1.4
1.6
1.8
M ($\pi_2^+ \pi^-$) GeV
XBL681-1542

Fig. 23

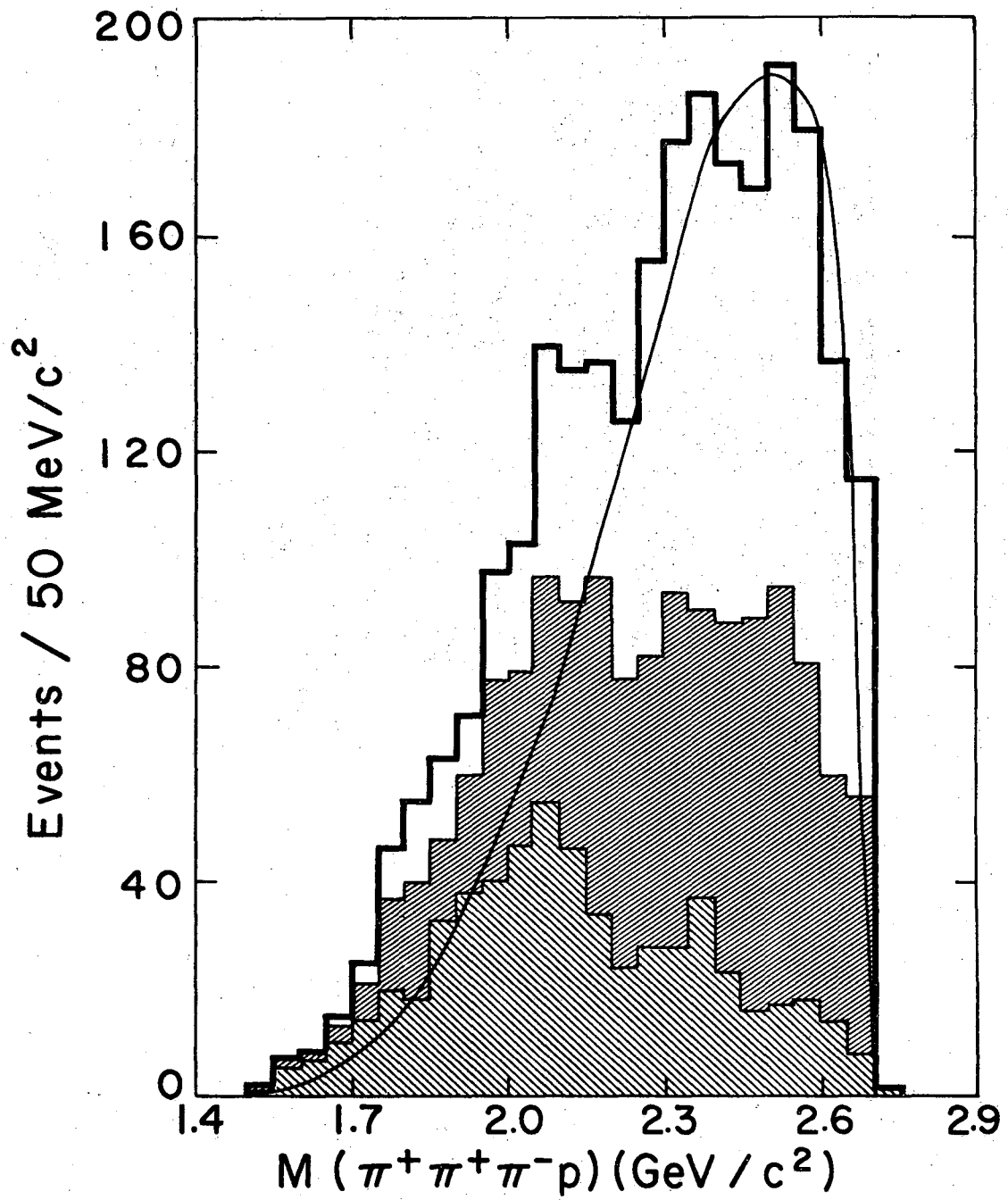

XBL6712-5986

Fig. 24

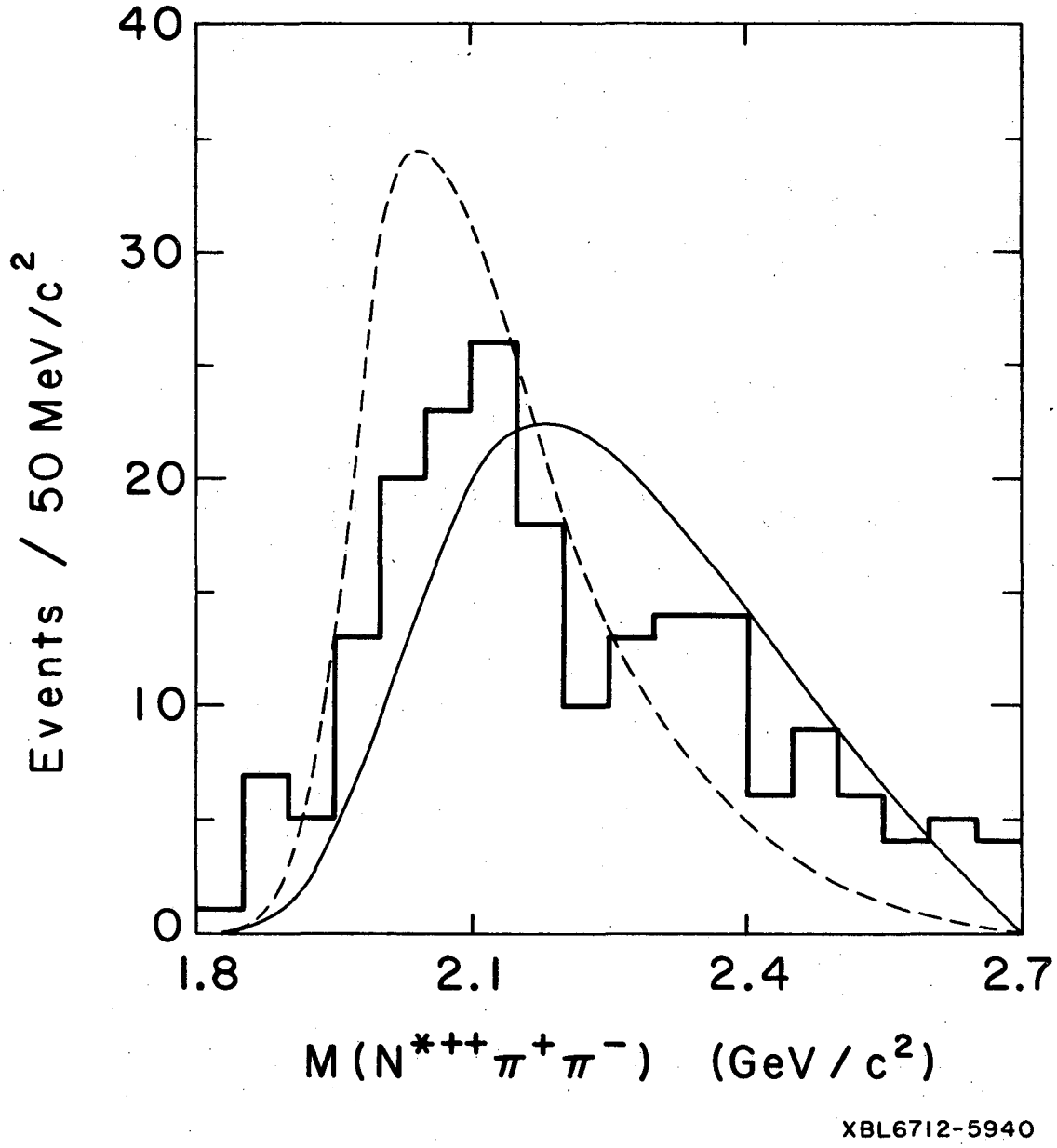
40
30
20
10
0
Events / 50 MeV/c²
1.8
2.1
2.4
2.7
M(N*++π+π−) (GeV/c²)
XBL6712-5940

Fig. 25

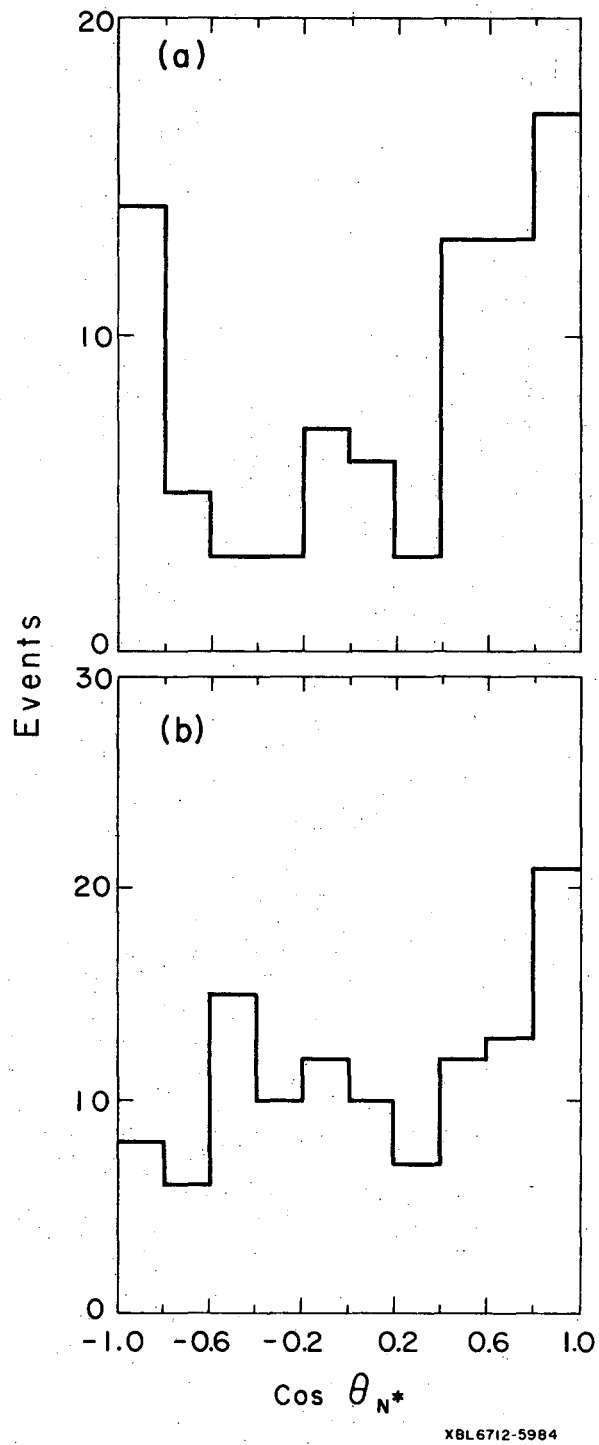
(a)
(b)
Events
20
10
0
30
20
10
0
-1.0
-0.6
-0.2
0.2
0.6
1.0
Cos θ_{N^*}
XBL6712-5984

Fig. 26

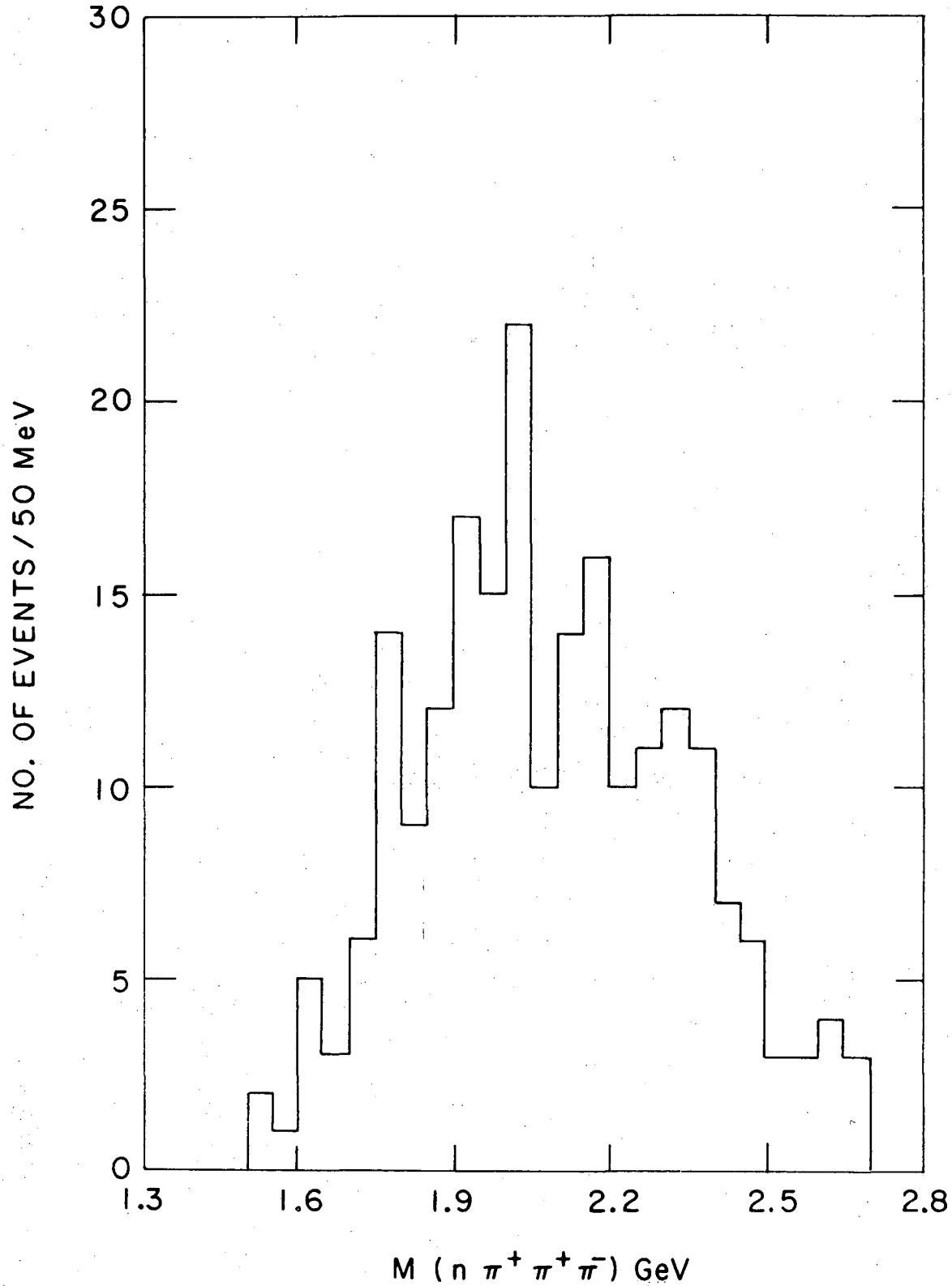
30
25
20
15
10
5
0
NO. OF EVENTS / 50 MeV
1.3
1.6
1.9
2.2
2.5
2.8
M (n $\pi^+ \pi^+ \pi^-$) GeV

Fig. 27

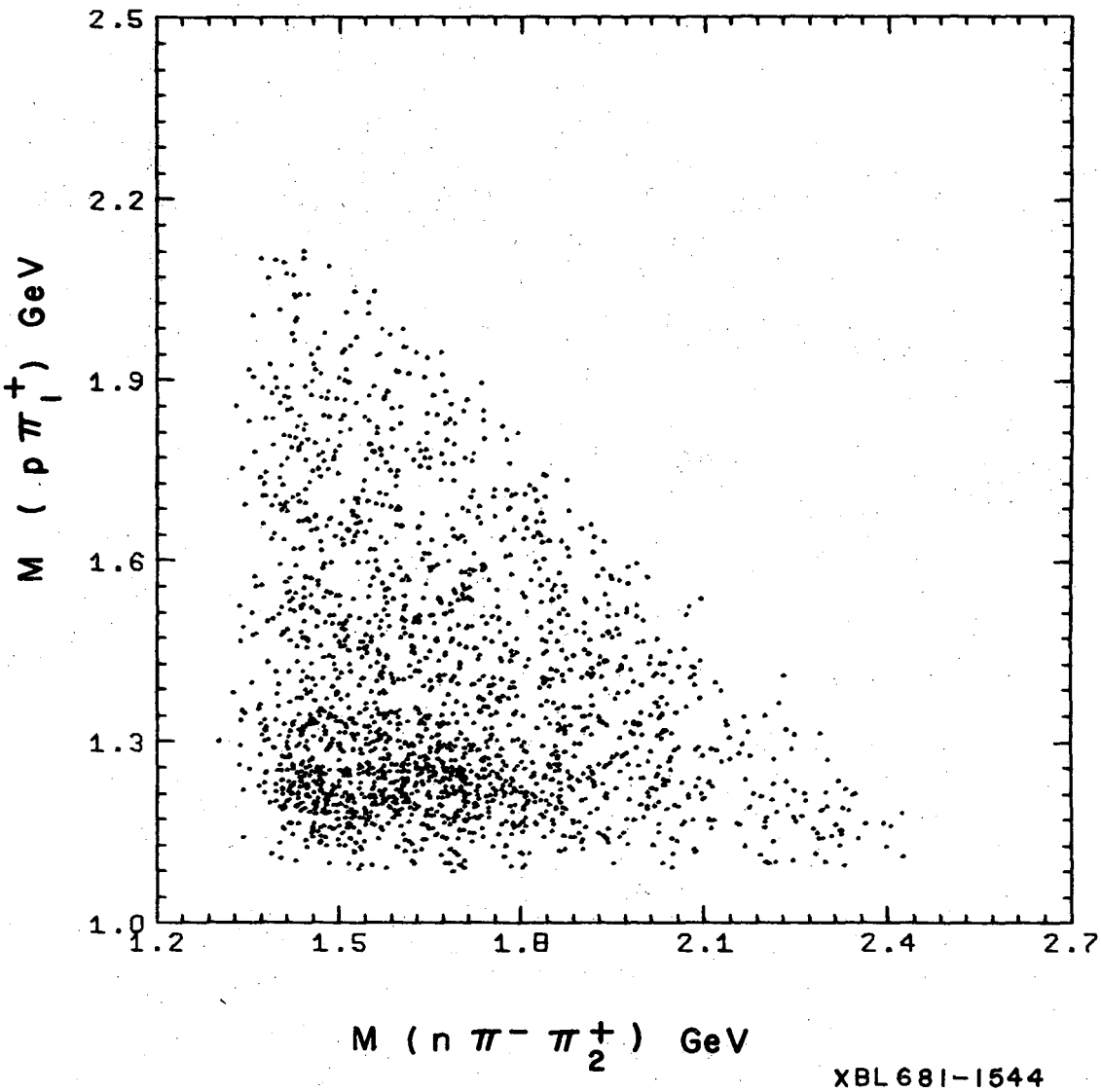
2.5
2.2
1.9
1.6
1.3
1.0
1.2
1.5
1.8
2.1
2.4
2.7
M (p π_1^+) GeV
M (n π^- π_2^+) GeV
XBL 681-1544

Fig. 28

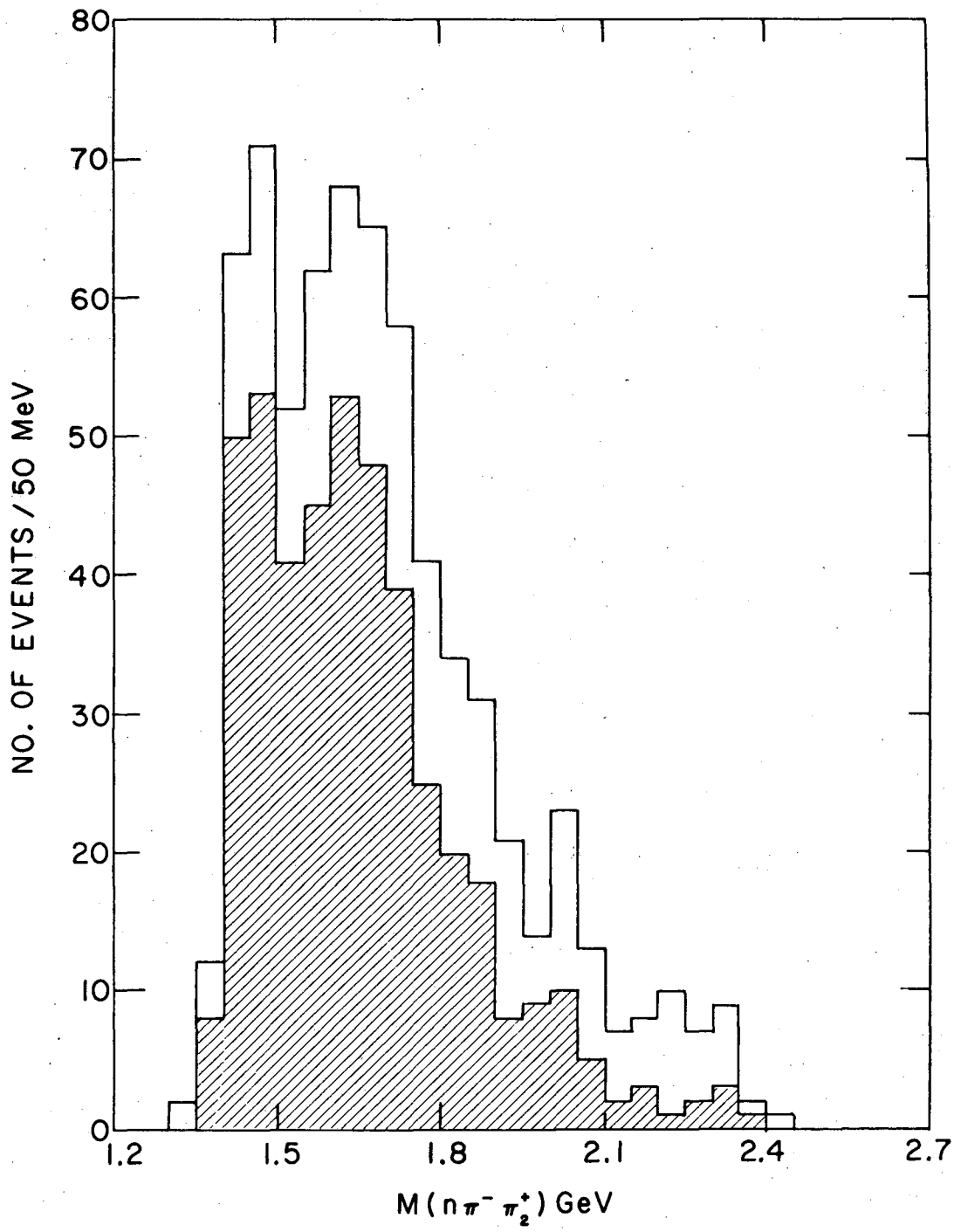

XBL 686-982

Fig. 29

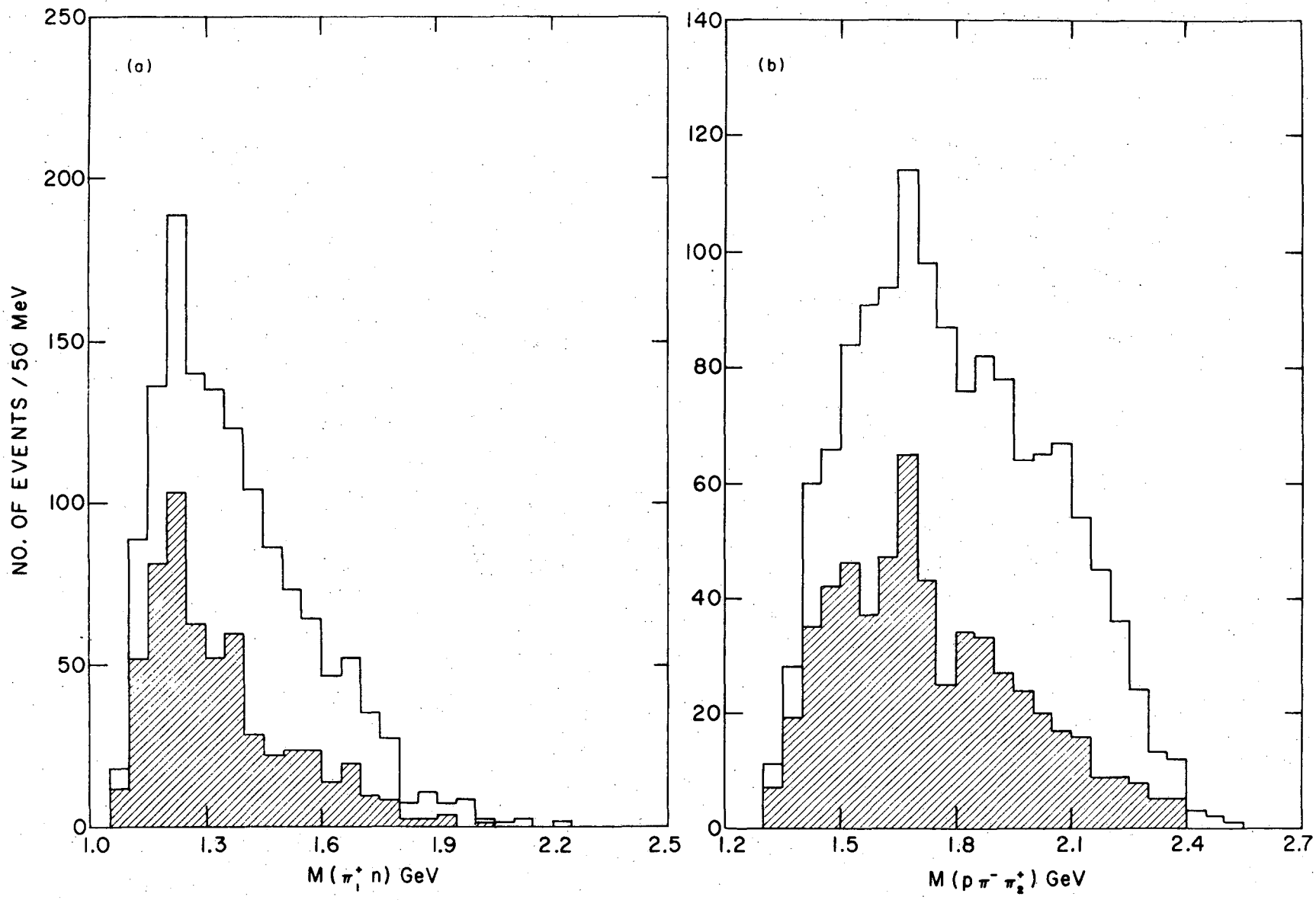
(a)
(b)
NO. OF EVENTS / 50 MeV
250
200
150
100
50
0
140
120
100
80
60
40
20
0
1.0
1.3
1.6
1.9
2.2
2.5
1.2
1.5
1.8
2.1
2.4
2.7
M (π_1^+ n) GeV
M (p π^- π_2^+) GeV

Fig. 30

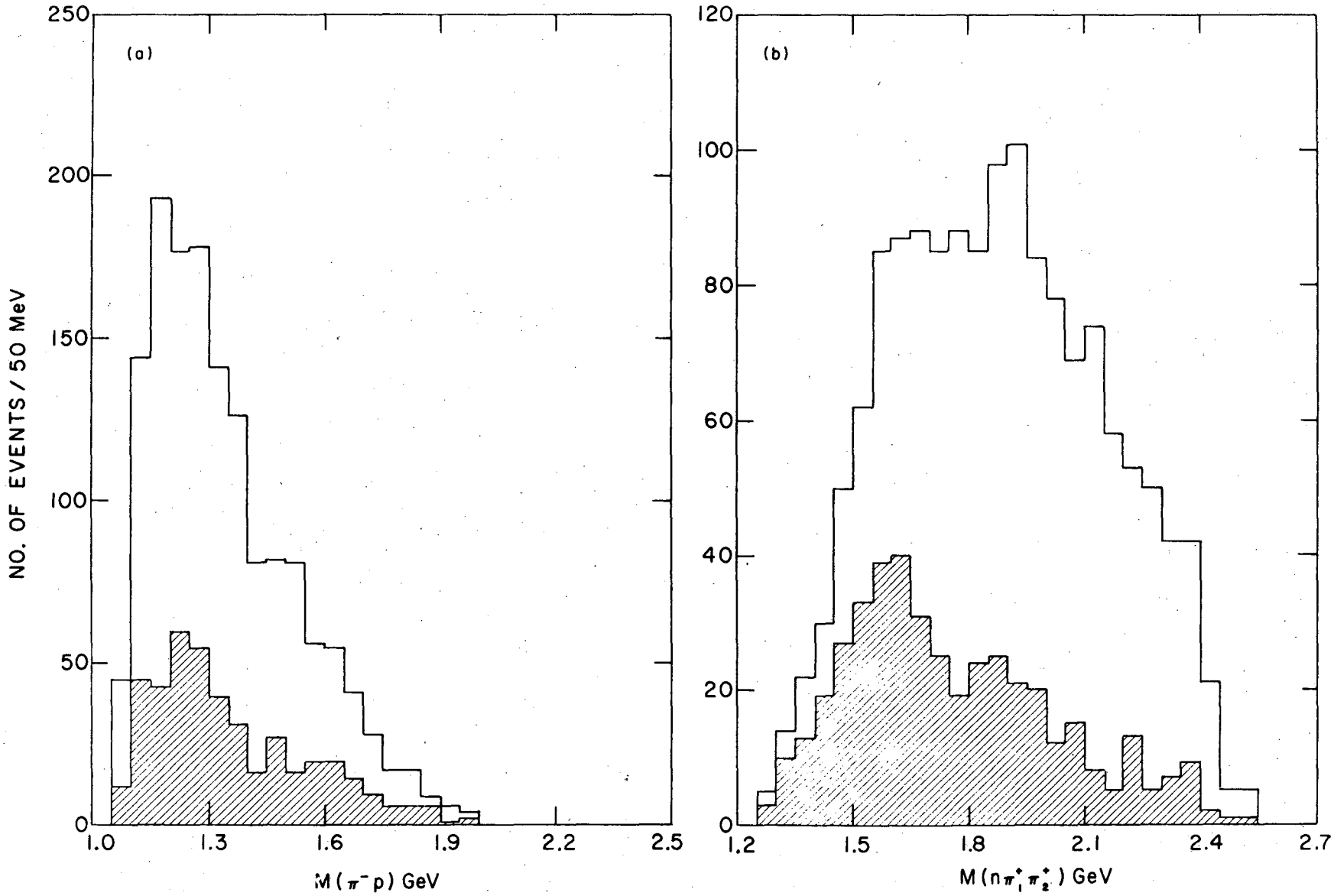
(a)
(b)
NO. OF EVENTS / 50 MeV
250
200
150
100
50
0
120
100
80
60
40
20
0
1.0
1.3
1.6
1.9
2.2
2.5
1.2
1.5
1.8
2.1
2.4
2.7
M (π^- p) GeV
M (n $\pi_1^+ \pi_2^+$) GeV

Fig. 31

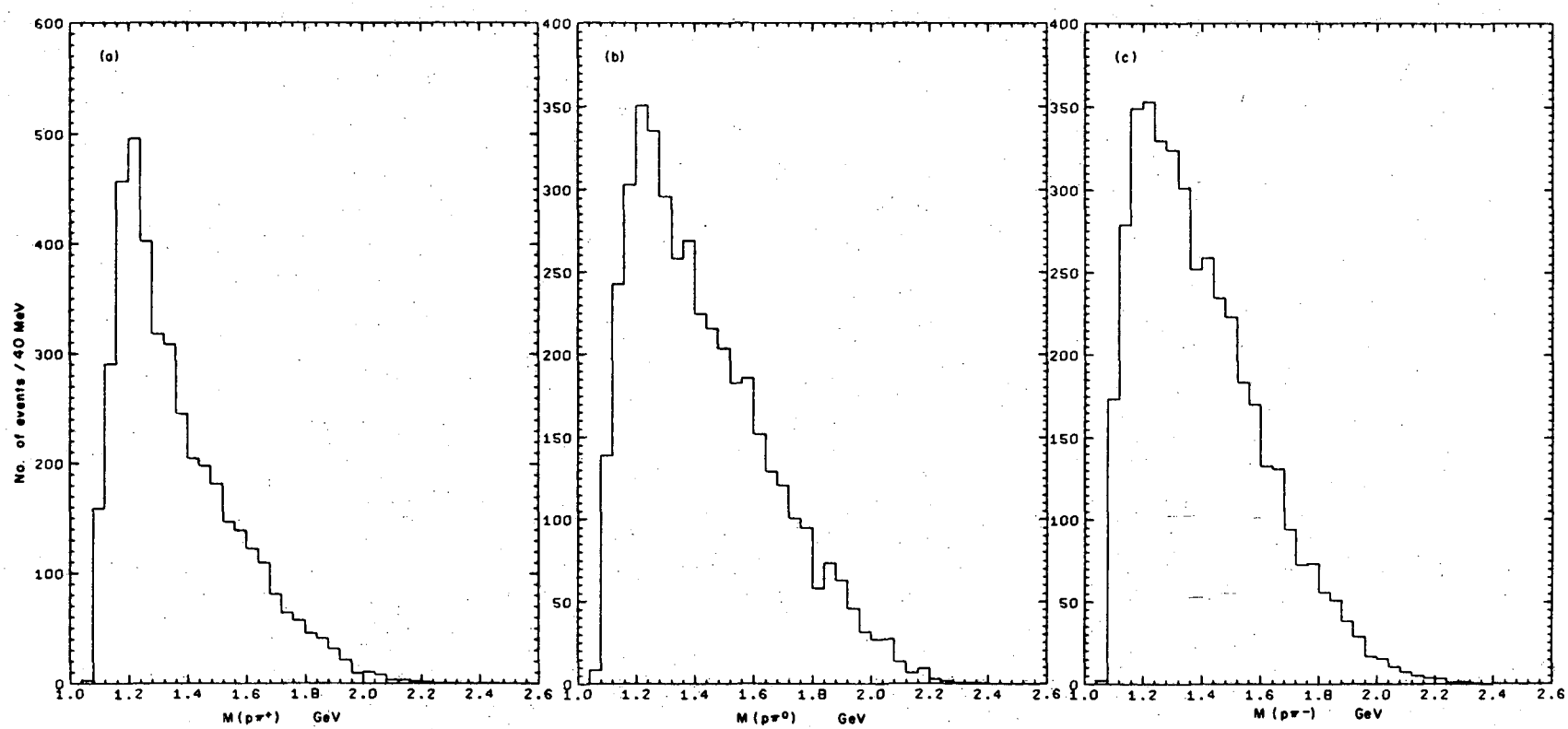

Fig. 32

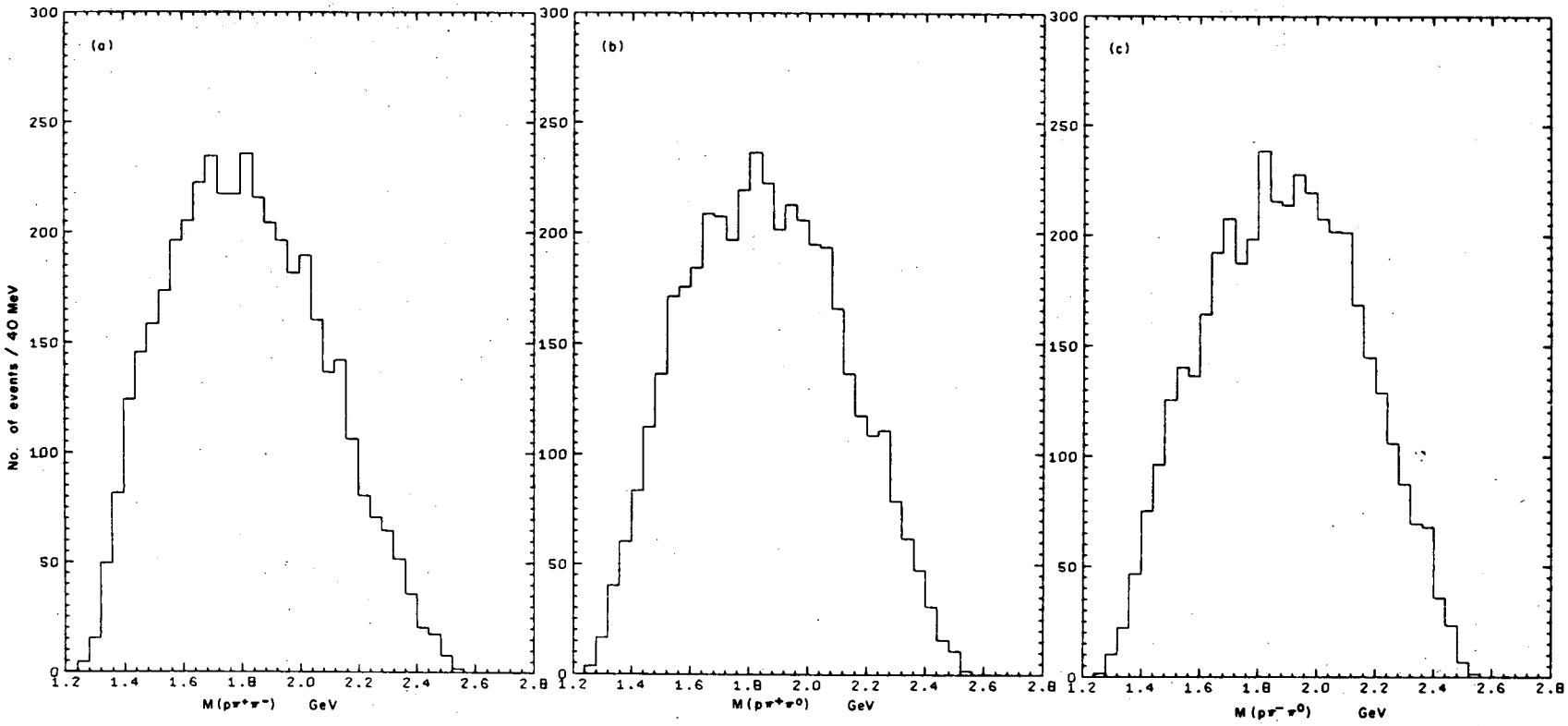
(a)
(b)
(c)
No. of events / 40 MeV
0
50
100
150
200
250
300
1.2
1.4
1.6
1.8
2.0
2.2
2.4
2.6
2.8
M(pπ+π−) GeV
M(pπ+π0) GeV
M(pπ−π0) GeV

Fig. 33

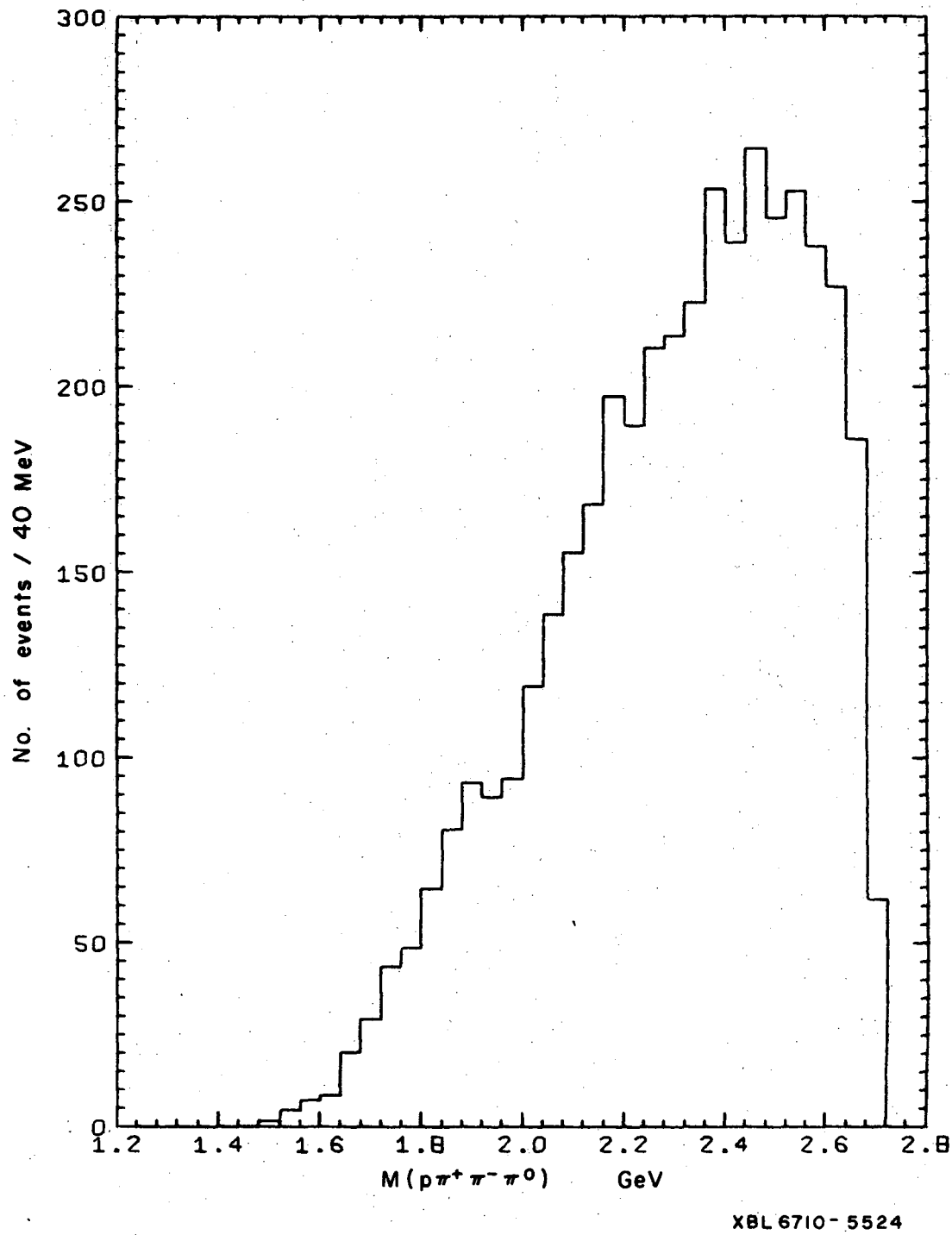
300
250
200
150
100
50
0
No. of events / 40 MeV
1.2
1.4
1.6
1.8
2.0
2.2
2.4
2.6
2.8
M(pπ⁺π⁻π⁰) GeV
XBL 6710-5524

Fig. 34

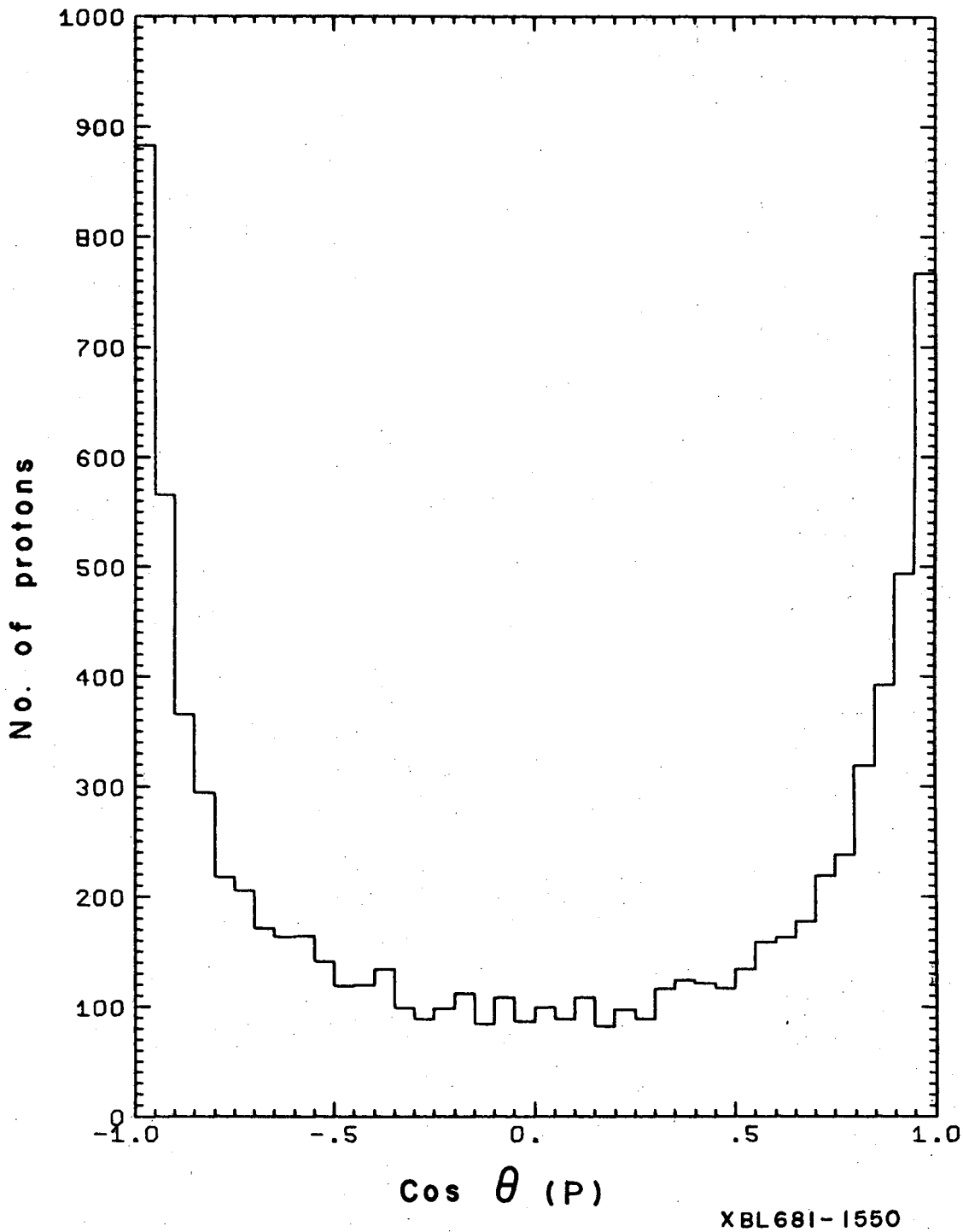
1000
900
800
700
600
500
400
300
200
100
0
No. of protons
-1.0
-.5
0.
.5
1.0
Cos θ (P)
XBL681-1550

Fig. 35

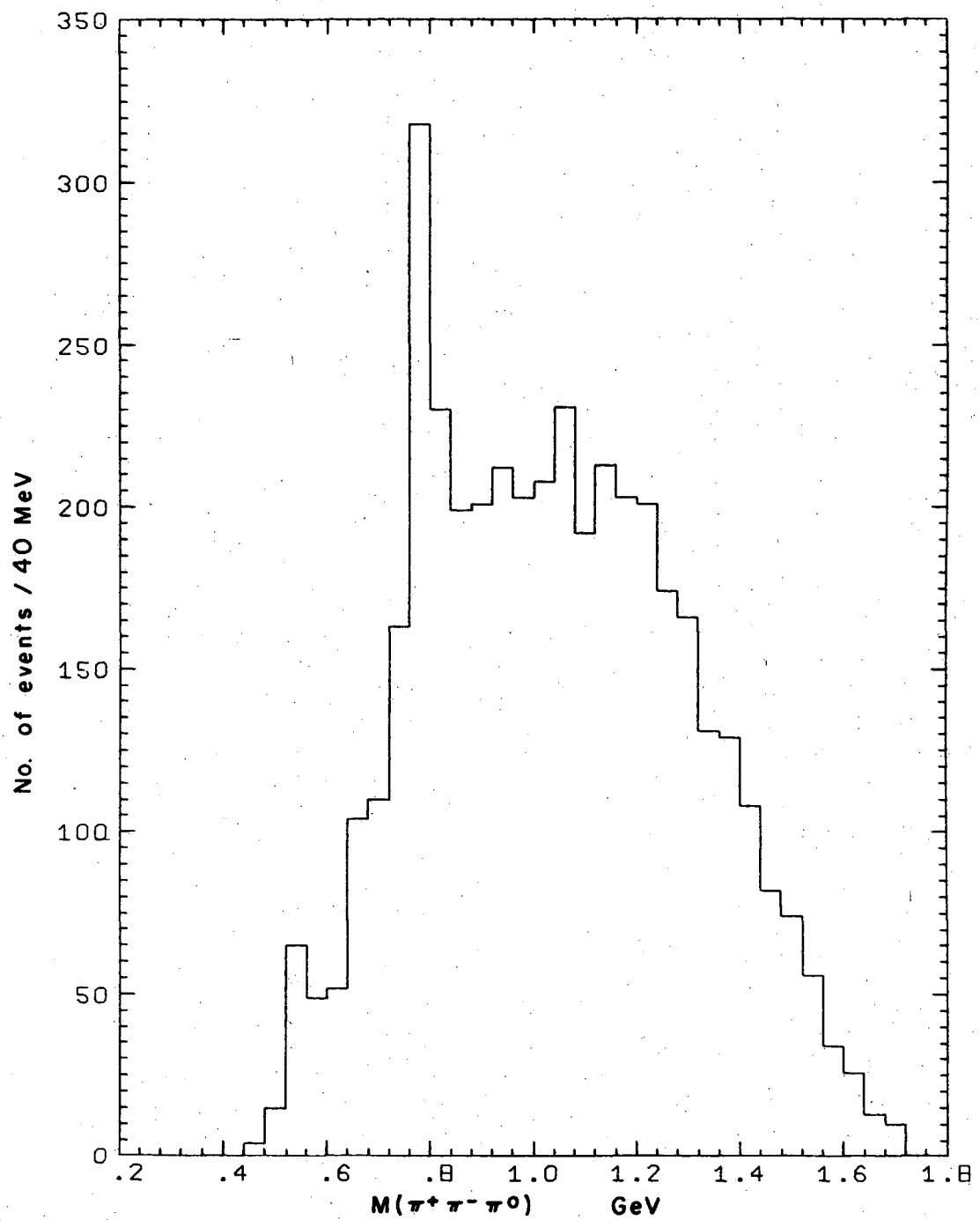

XBL6710-5529

Fig. 36

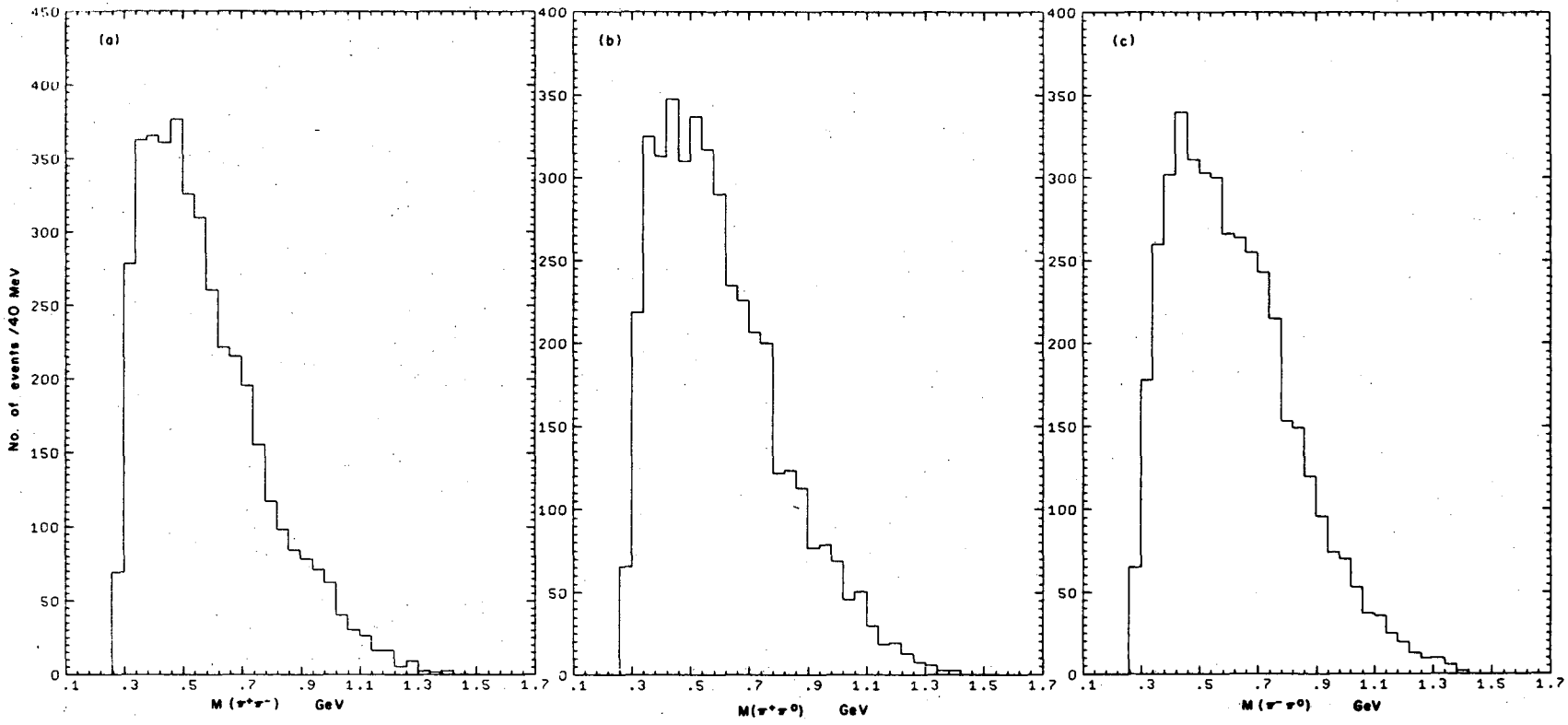

Fig. 37

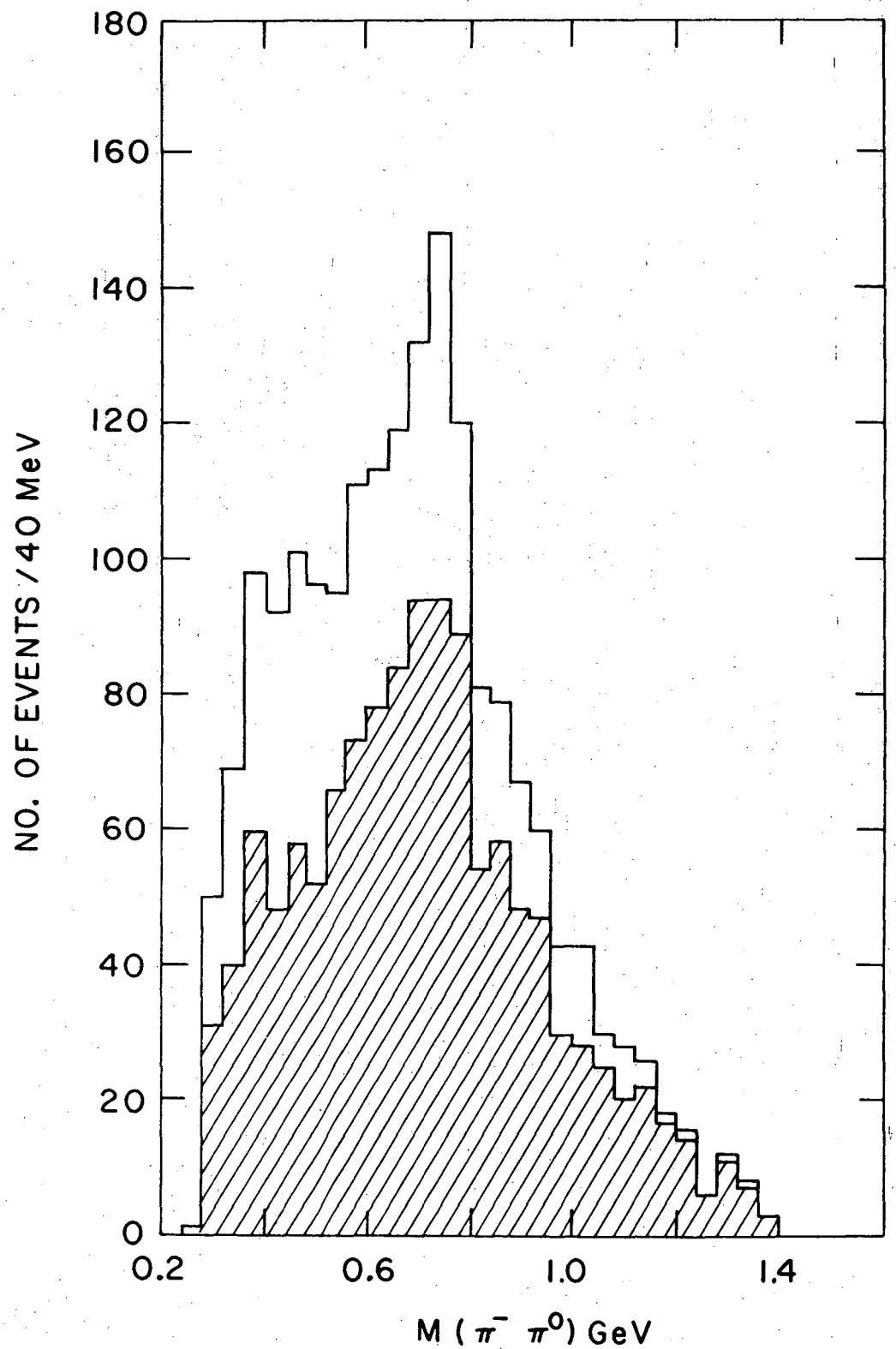
180
160
140
120
100
80
60
40
20
0
NO. OF EVENTS / 40 MeV
0.2
0.6
1.0
1.4
M (π^- π^0) GeV

Fig. 38

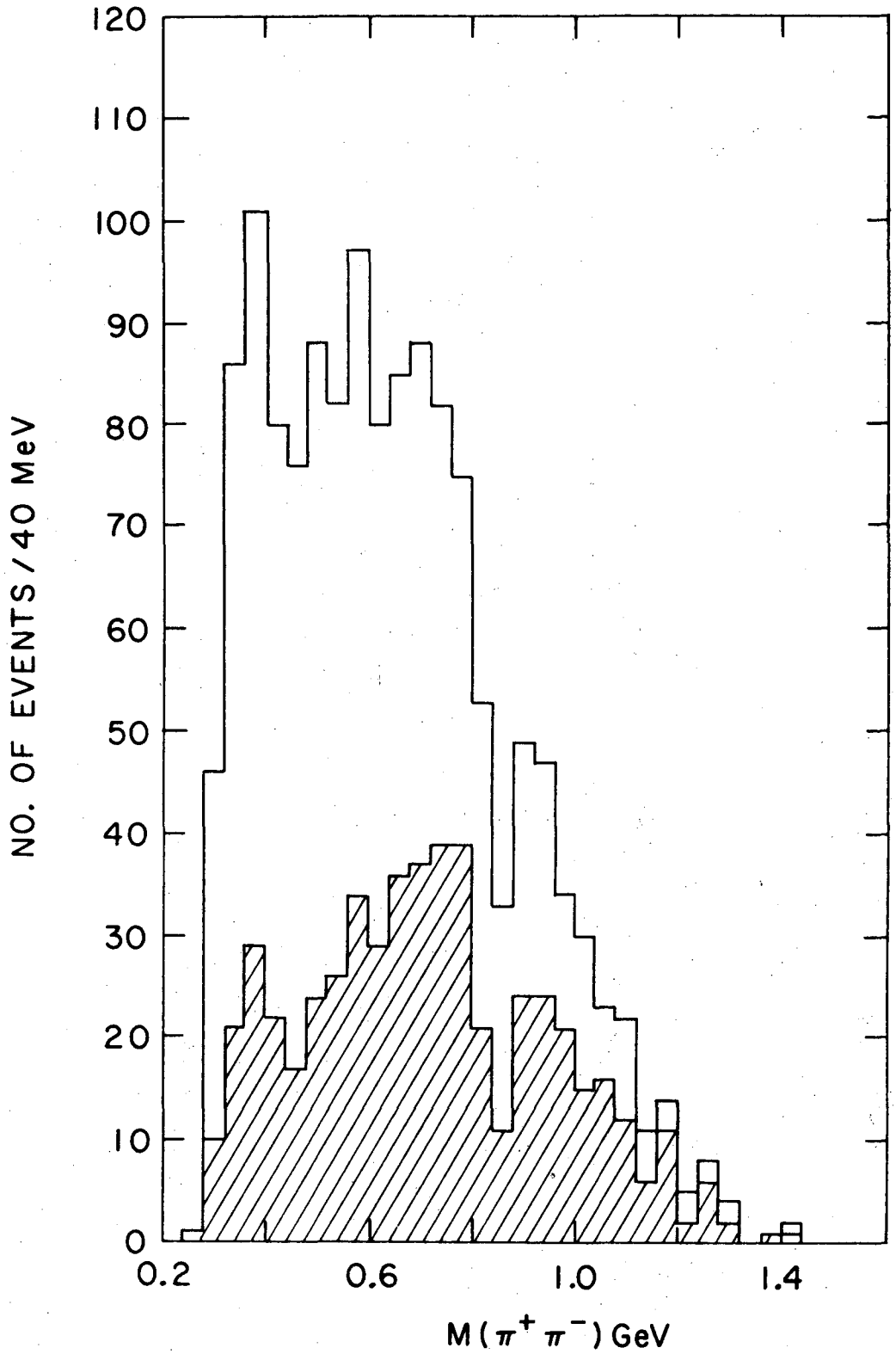
120
110
100
90
80
70
60
50
40
30
20
10
0
NO. OF EVENTS / 40 MeV
0.2
0.6
1.0
1.4
M (π+ π−) GeV

Fig. 39

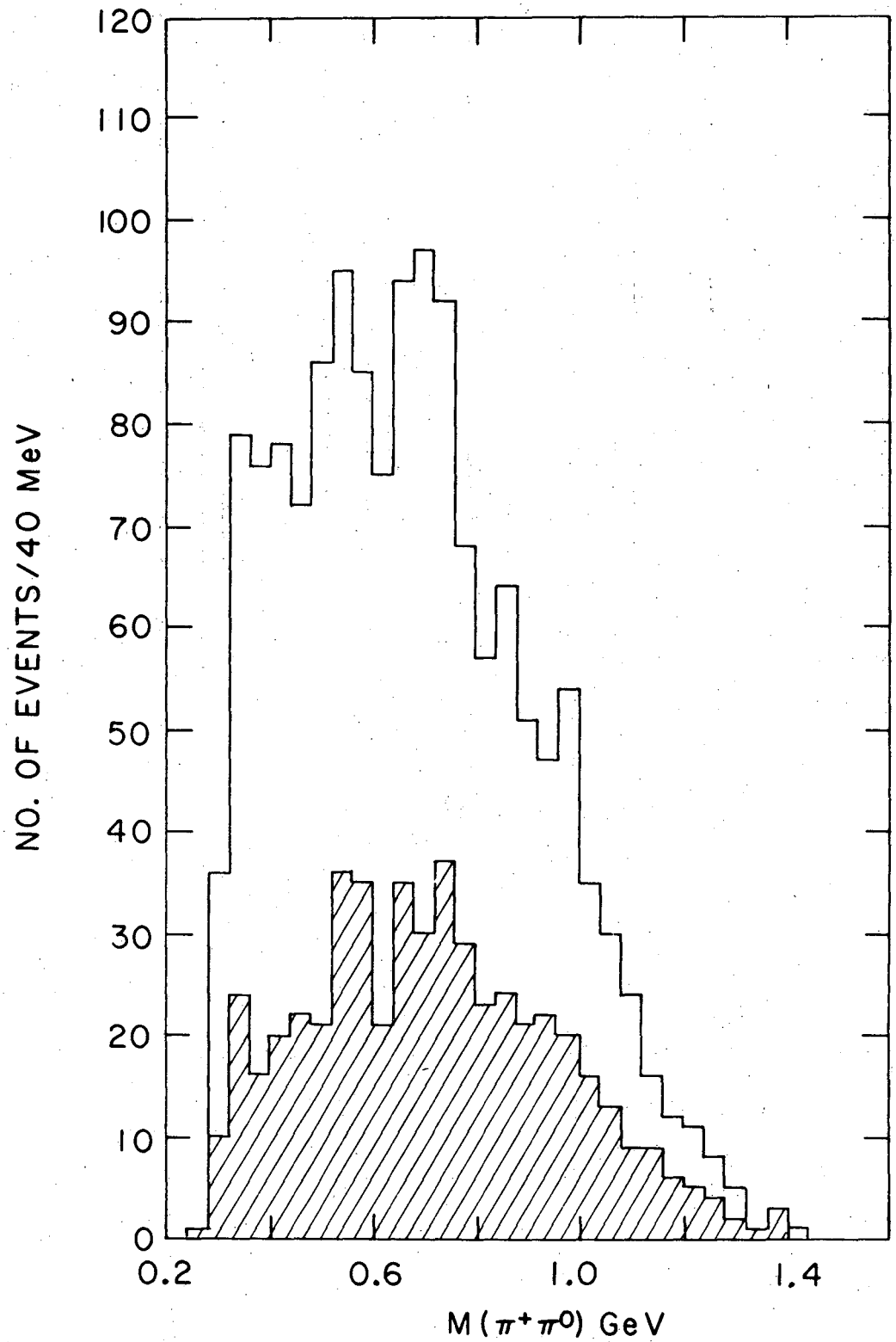
120
110
100
90
80
70
60
50
40
30
20
10
0
NO. OF EVENTS/40 MeV
0.2
0.6
1.0
1.4
M ($\pi^+\pi^0$) GeV

Fig. 40

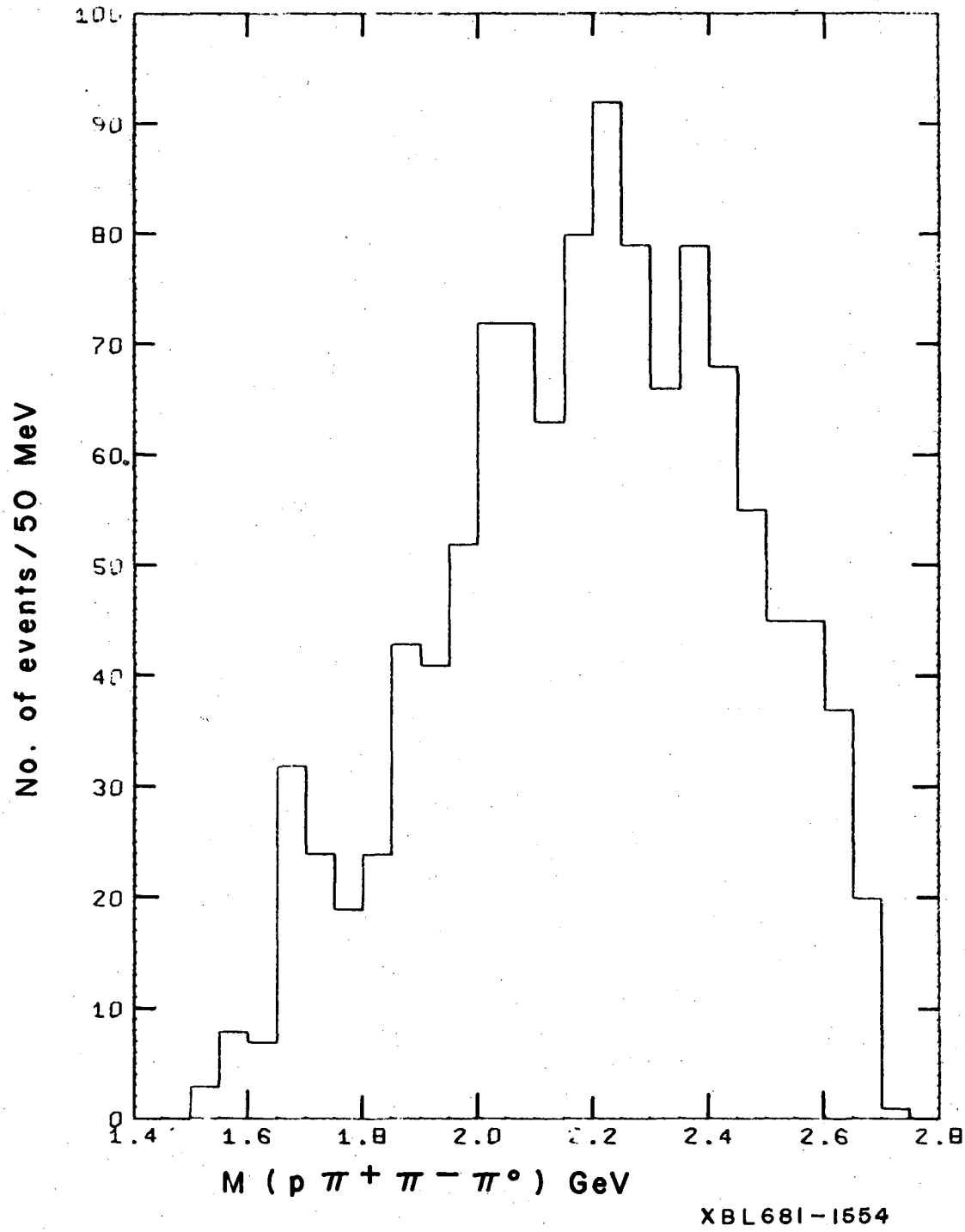
No. of events / 50 MeV
100
90
80
70
60
50
40
30
20
10
0
1.4
1.6
1.8
2.0
2.2
2.4
2.6
2.8
M (p π + π − π°) GeV
XBL681-1554

Fig. 41

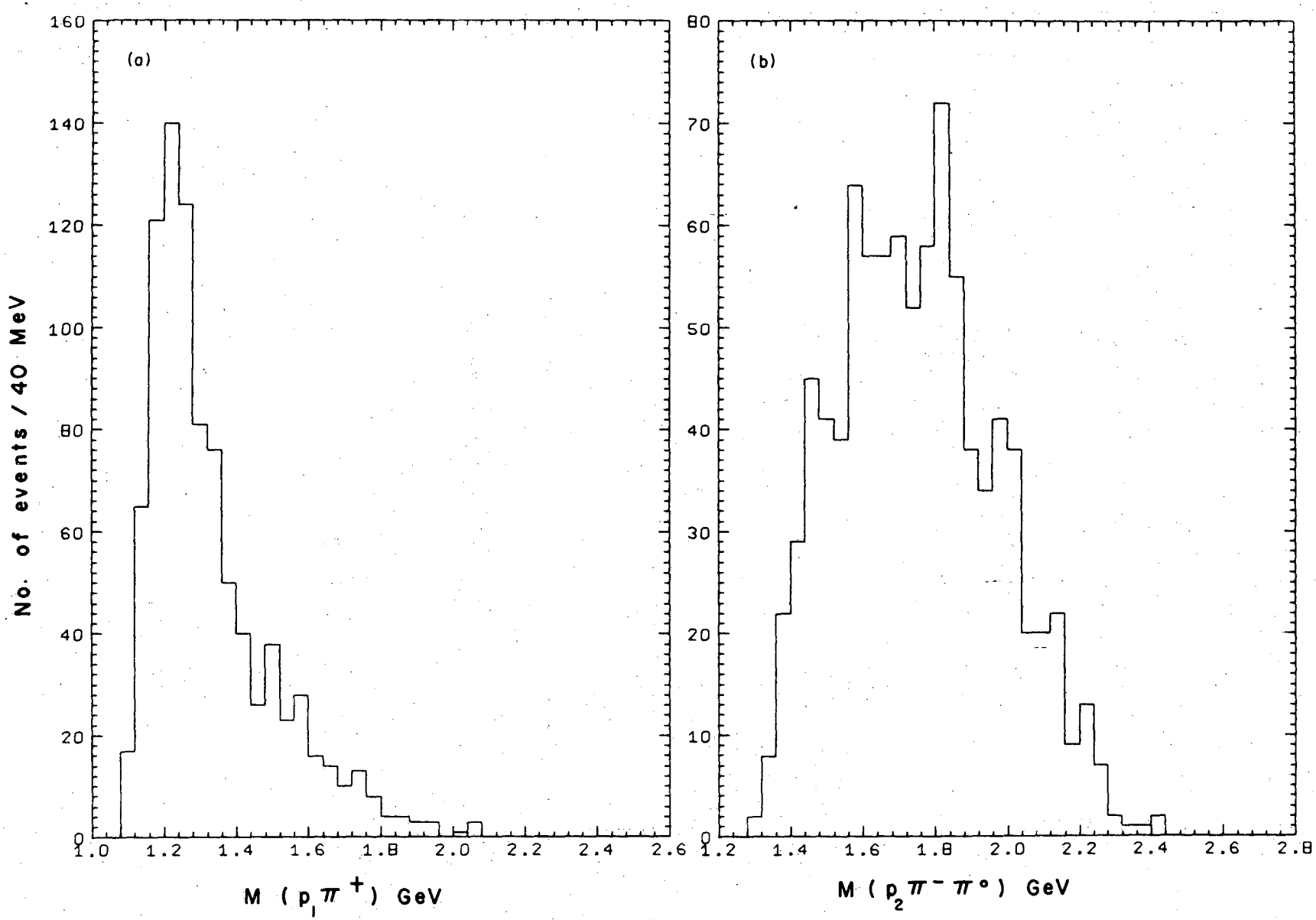
(a)
(b)
No. of events / 40 MeV
M ($p_1 \pi^+$) GeV
M ($p_2 \pi^- \pi^0$) GeV
0
20
40
60
80
100
120
140
160
10
30
50
70
1.0
1.2
1.4
1.6
1.8
2.0
2.2
2.4
2.6
2.8

Fig. 42

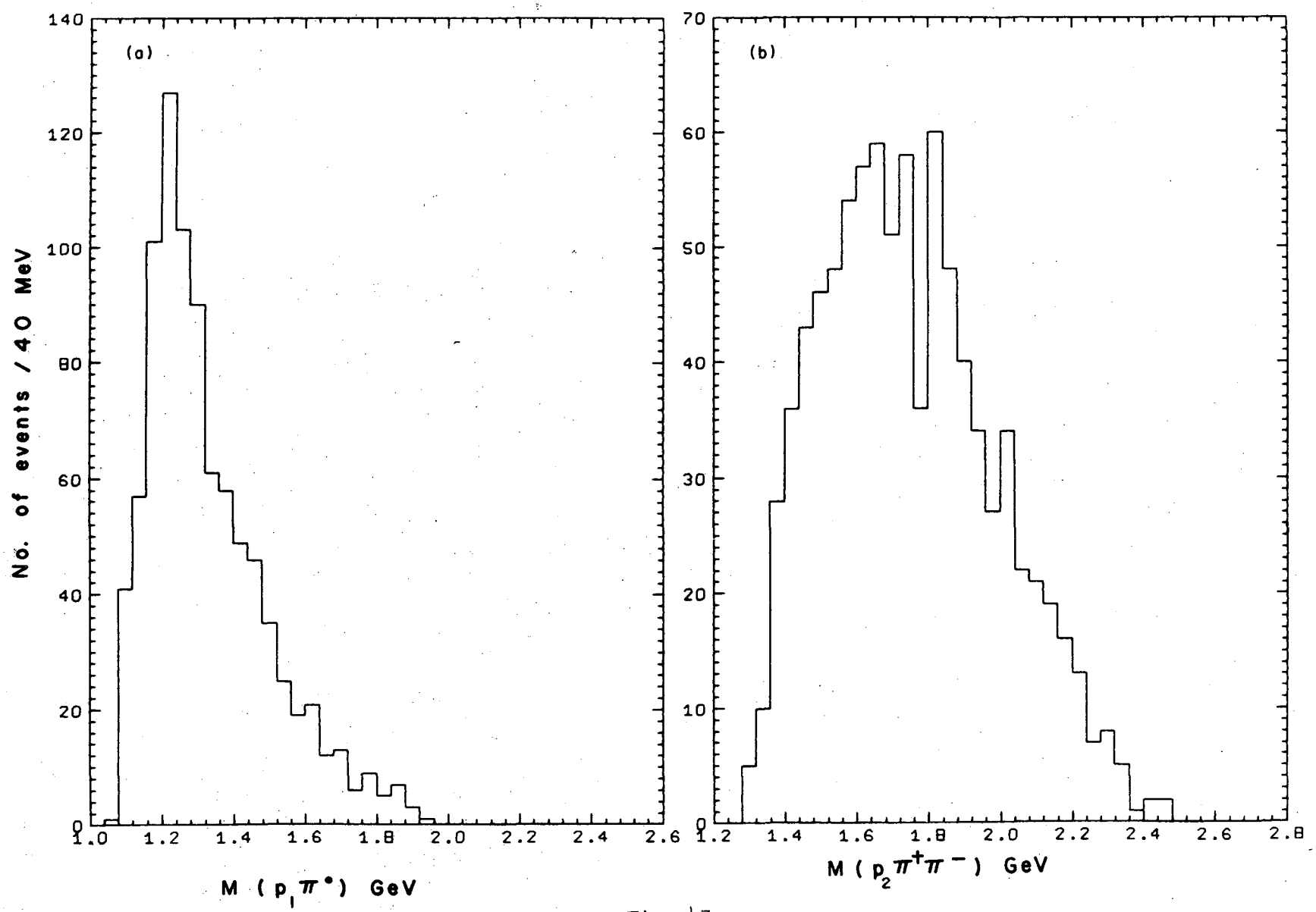
(a)
(b)
No. of events / 40 MeV
M (p1 π°) GeV
M (p2 π+ π−) GeV
0
20
40
60
80
100
120
140
10
30
50
70
1.0
1.2
1.4
1.6
1.8
2.0
2.2
2.4
2.6
2.8

Fig. 43

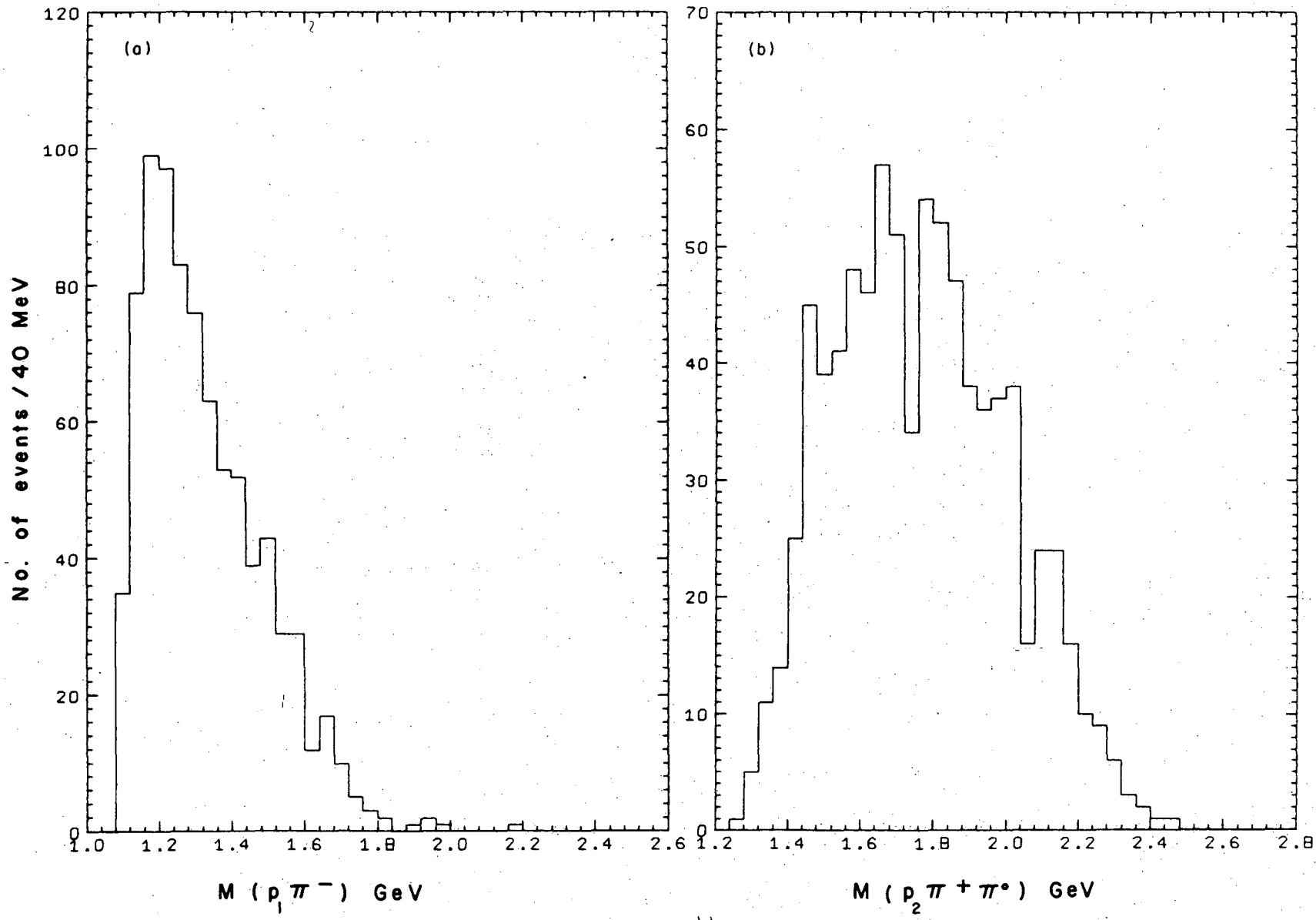
(a)
(b)
No. of events / 40 MeV
M (p1 π−) GeV
M (p2 π+ π°) GeV
0
20
40
60
80
100
120
10
30
50
70
1.0
1.2
1.4
1.6
1.8
2.0
2.2
2.4
2.6
2.8

Fig. 44

This report was prepared as an account of Government sponsored work. Neither the United States, nor the Commission, nor any person acting on behalf of the Commission:

A. Makes any warranty or representation, expressed or implied, with respect to the accuracy, completeness, or usefulness of the information contained in this report, or that the use of any information, apparatus, method, or process disclosed in this report may not infringe privately owned rights; or

B. Assumes any liabilities with respect to the use of, or for damages resulting from the use of any information, apparatus, method, or process disclosed in this report.

As used in the above, "person acting on behalf of the Commission" includes any employee or contractor of the Commission, or employee of such contractor, to the extent that such employee or contractor of the Commission, or employee of such contractor prepares, disseminates, or provides access to, any information pursuant to his employment or contract with the Commission, or his employment with such contractor.